

Submitted in accordance with the requirements for the degree of
Doctor of Philosophy



UNIVERSITY OF LEEDS

SCHOOL OF PHYSICS & ASTRONOMY

**Interacting Non-Abelian Anyons in an
Exactly Solvable Lattice Model**

Ville Tapani Lahtinen

March 2010

The candidate confirms that the work submitted is his own and that appropriate credit has been given where reference has been made to the work of others. This copy has been supplied on the understanding that it is copyright material and that no quotation from the thesis may be published without proper acknowledgement.

Acknowledgements

First and foremost I would like to thank my parents who have continuously supported me throughout the 20+ years I have spent educating myself.

Second, I would like to thank my Master's thesis supervisor Dr. Claus Montonen, who gave my studies direction by pointing me towards the fascinating field of topological quantum computing. I would have been much less happy a man had I stayed tuning the parameters of the Standard Model while waiting for the LHC to become operational.

What comes to the PhD work itself, my supervisor Dr. Jiannis Pachos deserves my deepest gratitude. His sharp physical intuition guided me to work on topical problems, and his wide knowledge on contemporary theory provided new ways to address them. Concerning my understanding of physics, working with him has contributed to it more than all the courses I have taken combined. I would also like to thank the Engineering and Physical Sciences Research Council and The Finnish Academy of Science for the financial support that made this thesis possible and enabled active participation in the physics community.

Further, I'd like to thank my close colleague and office mate James Wootton, with whom I had several scientific collaborations, as well as shared many moments of dry witty British humour. Fellow students Andreas Kurcz and Michal Hajdusek deserve also an honourable mention for their integral role in the "collaborations" at the numerous pubs of Leeds. Academic freedom was exercised to the full, and somehow it all contributed for the greater good. Also, this thesis would not have been possible without the procrastinatory relief provided by Google Maps (Hey, you

can walk through Australia on Google Street View!), Oxford English Dictionary (What is a scalliwag anyway? Oh, it is a rascalion.) and the BBC website (Probe sees 'Pac-man in the moon').

Finally, with self-ironic undertones, I would like to thank myself for being too lazy to study for the entry examinations for a course in economics. This led to a career in physics which now culminates on this thesis. Although I still entertain the odd idea that the grass is greener on the other side, the more I get into physics research, the more I regard that idea as just an optical illusion.

Abstract

Ville Tapani Lahtinen, “Interacting Non-Abelian Anyons in an Exactly Solvable Lattice Model”, Ph.D. thesis, University of Leeds, March 2010.

In this thesis, we study the non-Abelian anyons that emerge as vortices in Kitaev’s honeycomb spin lattice model. By generalizing the solution of the model, we explicitly demonstrate the non-Abelian fusion rules and the braid statistics that characterize the anyons. This is based on showing that the presence of vortices leads to zero modes in the spectrum. These can acquire finite energy due to short range vortex-vortex interactions. By studying the spectral evolution as a function of the vortex separation, we unambiguously identify the zero modes with the fusion degrees of freedom of non-Abelian anyons.

To calculate the non-Abelian statistics, we show how the vortex transport can be implemented through local manipulation of the couplings. This enables us to employ the eigenstates of the model to simulate a process where a vortex winds around another. The corresponding evolution of the degenerate ground state space is given by a Berry phase, which under suitable conditions coincides with the statistics. By considering a range of finite size systems, we find a physical regime where the Berry phase gives the predicted statistics of the anyonic vortices with high fidelity.

Finally, we study the full-vortex sector of the model and find that it supports a previously undiscovered topological phase. This new phase emerges from the phase with non-Abelian anyons due to their interactions. To study the transitions between the different topological phases appearing in the model, we consider the Fermi surface, whose topology captures the characteristic long-range properties. Each phase

is found to be characterized by a distinct number of Fermi points, with the number depending on distinct global Hamiltonian symmetries. To study how the Fermi surfaces evolve into each other at phase transitions, we consider the low-energy field theory that is described by Dirac fermions. We show that phase transition driving perturbations translate to a coupling to chiral gauge fields, that always lead to Fermi point transport. By studying this transport, we obtain analytically the extended phase space of the model and its properties.

Contents

Acknowledgements	i
Abstract	iii
1 Introduction	1
1.1 Motivation and the structure of the thesis	5
2 Kitaev's Honeycomb Lattice Model	9
2.1 The spin lattice model	10
2.2 Mapping to free Majorana fermions	12
2.3 Solution for arbitrary periodic vortex configurations	14
2.4 The phase diagram in the absence of vortices	18
2.4.1 The Chern number	20
2.4.2 Ising anyons	22
2.5 Numerical diagonalization	26
2.6 Summary	27
3 Non-Abelian Fusion Rules and Braid Statistics	29
3.1 Gauge/coupling configuration equivalence and vortex transport . . .	30
3.2 Fusion rules from the spectral evolution	32
3.2.1 Zero modes and vortex interactions	33
3.2.2 The low-energy spectrum	36
3.2.3 Zero modes as fusion degrees of freedom	39
3.2.4 Discussion	40

Contents

3.3	Non-Abelian statistics as a Berry phase	42
3.3.1	Statistics and holonomies	42
3.3.2	Discrete holonomies	46
3.3.3	Holonomy due to vortex transport	48
3.3.4	The study of the holonomy	49
3.3.5	Discussion	54
3.4	Summary	56
4	Going Beyond: A New Chiral Topological Phase	59
4.1	The full-vortex sector	60
4.1.1	Symmetries of the Fermi surface	62
4.2	The Fermi surface evolution	65
4.2.1	The low-energy field theory of Dirac fermions	66
4.2.2	Topological phase transitions driven by gauge fields	68
4.3	The role of anyon-anyon interactions in the phase transition	73
4.4	Summary	77
5	Conclusions	79
	Bibliography	85

List of Figures

2.1	The bi-colourable honeycomb lattice with the enumeration and orientation conventions	10
2.2	An illustration of the generalized unit cell	15
2.3	The vortex-free sector phase diagram	19
2.4	A diagrammatic illustration of the fusion basis states and the F - and R -moves	24
3.1	The gauge/coupling configuration equivalence	30
3.2	Continuous vortex transport by locally manipulating the couplings .	31
3.3	Zero modes due to interacting vortices	34
3.4	Convergence of the zero mode energy and the interaction length scale ξ	35
3.5	Fermion and vortex gaps as functions of K	36
3.6	The low-energy spectrum of the non-Abelian phase	38
3.7	Vortex braiding on the lattice	44
3.8	The monodromy of Ising anyons	45
3.9	The fermion gap and the degeneracy splitting during the vortex transport	50
3.10	The fidelities of the holonomy for different system sizes	53
4.1	A coupling configuration giving rise to the full-vortex sector	60
4.2	The full-vortex sector phase diagram	61
4.3	The vortex-free and the full-vortex sector band structures	63
4.4	Fermi surface topology and the Chern number	68

4.5	The evolution of the Fermi points under phase transition driving perturbations	69
4.6	The extended phase space	72
4.7	A schematic illustration of the emergence of the full-vortex band structure due to interacting anyonic vortices	74
4.8	The full-vortex sector as a dual lattice of the honeycomb lattice . . .	76

Chapter 1

Introduction

I started my journey into topologically ordered systems more or less by an accident. When back in 2005 I was pondering about a possible Master's thesis topic, all I knew was that I wanted to do something quantum information related. It turned out that my previous supervisor did not know much about quantum information. His latest research concerned quantum field theory in a non-commutative space-time, which could hardly be further away. However, where physical theories are related to particular problems, the mathematical structures underlying them know not of such restrictions. The same mathematics may play a role in systems which have nothing to do with each other. It was such a connection that set me on my way to topologically ordered systems.

In non-commutative geometry one uses a piece of mathematics known as quantum groups to quantize the space-time geometry [1]. My supervisor had encountered them also earlier in connection with discrete lattice gauge theories [2]. Such theories were known to give rise to *anyons*, particles with exotic intermediate statistics between bosons and fermions, that were first envisioned by Leinaas and Myrheim [3] and later developed in a more physical setting by Wilczek [4, 5]. However, due to their limited applicability and the extreme physical conditions required, the research of anyons had stayed on the fringes of contemporary theoretical physics. This all changed with the seminal paper by Alexei Kitaev, [6], where he was the first to

propose employing anyons for intrinsically fault-tolerant quantum computation, i.e. performing *topological quantum computation* [7]. This paper was conceived already in 1997, but it got published in a peer-reviewed journal only in 2003. So, when my supervisor suggested me doing the master's thesis on this topic, it was still a novel field with nothing but open questions.

During spring 2006 when I was putting finishing touches on my Master's thesis [8], I discovered the KITP program "Topological Phases and Quantum Computation" which one could follow online. The mood of the talks was enthusiastic, although the field seemed to lack cohesion with a number of potential approaches and techniques, all with their own advantages and shortcomings. This feeling was best captured in an earlier talk by Michael Freedman [9], which I quoted for the opening paragraph of my Master's thesis. Now four years later, our understanding of topological phases has taken significant steps forward. Still, I find these words resonating enough with what is fascinating about the field for them to be repeated here:

"... you don't want to do it unless there is a sweet way to do it. That is sort of the way I feel about topological quantum computation, that the word topological is going to make it sweet, that we are not going to take some system and just make it more and more isolated, colder and colder and force one or two more qubits in a year out of it. We are going to do something that is beautiful and elegant and then even if we fail, we have at least pursued the right course and will probably learn something interesting about solid state physics on the way."

-Michael H. Freedman, 2004, [9]

Looking at the field of topological quantum computing today, the research is still more about "learning something interesting about solid state physics", than putting the final pieces together. Referring to the recent advances in topologically ordered systems as just "something interesting", however, does no justice to them.

On the conceptual side, a more holistic picture has been obtained. Anyon models with up to 4 particle types have been catalogued [10], the general properties of sys-

tems giving rise to them have been classified [11, 12], and the connections between different approaches have also been clarified [13–16]. Topological entanglement entropy, [17, 18], has been established as a robust characteristic of topological order in finite temperatures [19], and the recently introduced entanglement spectrum, [20], promises to provide a new characterization. The abstract theory of anyons has also been extended to account for anyon-anyon interactions [21]. These were discovered to drive phase transitions between topological phases [22–25], which can also result from a condensation of anyons [26, 27]. Also, whereas a few years ago Preskill’s lecture notes, [28], were the standard reference for topological quantum computing, nowadays there exist several comprehensive review articles [29, 30].

The fractional quantum Hall effect has long been the primary field of research in topologically ordered systems. The recent years have seen more candidate trial wave functions being proposed [31–33], and our understanding of the known ones has improved [34]. With the proliferation of plausible candidates though, the field seems to be waiting for a decisive experiment to guide the theory. Steps towards this direction were taken by the first attempt to verify the existence of non-Abelian anyons. Where the Abelian quasiparticles of the celebrated Laughlin state, [35], had been detected by various groups [36, 37], the direct detection of non-Abelian anyons, [38], had remained an open question. A simple interferometric scheme was proposed in 2006 [39, 40], and it was over the following years translated to an experiment on the Moore-Read state [41]. Although non-conclusive, it gave for the first time strong direct evidence for the existence of non-Abelian anyons [42].

Similar rapid experimental advances took place also with recently discovered topological insulators [43–45]. Only a few years from the theoretical prediction, Majorana fermions, that are essentially non-Abelian anyons, were detected [46, 47]. This led to a curious paradigm shift. Whereas back in 2006 the Fibonacci anyons were the holy grail due to their universality for quantum computing, the experimental accessibility suddenly made the Majorana fermions the hottest topic in the field [48]. Although they are not universal for quantum computation by themselves,

various supplementary schemes have been considered [49, 50].

Instead of searching for anyons in nature, one can nowadays envision engineering systems that support them in a laboratory. These usually take the form of spin lattice models that can potentially be realized in optical lattices [51–54] or in superconducting arrays [55]. In the optical lattices the experiments for verifying topological order have been proposed [56], and the required steps to probe the anyons directly have been considered [57–59]. On the other hand, in Josephson-junction arrays topologically protected qubits have already been demonstrated [60], and extended encoding schemes have been proposed [61].

Among the lattice models a pioneering role has been played by the Kitaev’s honeycomb lattice model [62]. Its attractiveness is based in its analytic tractability as well as it supporting both Abelian and non-Abelian topological phases. The simple interactions required suggest that it is also likely to be the first one fully realized in an optical lattice experiment [51]. This richness comes with a price though. Unlike string-net, [63], or quantum double models, [6], that involve experimentally complex interactions, the honeycomb lattice model is not tailored to identically support anyons. This means that their characterization and control is both elusive and experimentally hard. It is this combination of promise and challenge that has made the model so fruitful for studying topologically ordered phases.

Since its introduction in 2005, the honeycomb lattice model has given birth to numerous projects, with even some of its footnotes being developed into PRL level publications. The original enthusiasm surrounding the model was based on the Abelian phase, because it supports the so called toric code anyons, that are the prototype for topological quantum memories [6]. Their emergence from the honeycomb lattice model has been studied in numerous works [64–66]. Lately the interest has shifted to the more elusive non-Abelian phase, which supports the so called Ising anyons. These are essentially identical to the topical Majorana fermions [62]. Recent studies have led to an explicit demonstration of edge states [67], topological degeneracy [68] and entanglement entropy [20]. A variation of the original model with

spontaneous time-reversal symmetry breaking, [69], and a generalization to higher spin systems, [70], have also been introduced. The non-Abelian Ising anyons have also been the topic of my research. The original contributions include the demonstration of the vortex interactions and fusion rules [71], the direct calculation of the non-Abelian statistics [72], as well as a discovery of a new chiral Abelian phase [73].

1.1 Motivation and the structure of the thesis

Topological order can be probed in many ways. Although partial characterization can be obtained by studying, for instance, the ground state degeneracy [74] or the entanglement entropy [17, 18], the ultimate unambiguous characterization is always given by the statistics of the anyonic excitations. Unfortunately, this is usually very hard. The emergence of anyons is a direct consequence of long-range entanglement in the ground state, which can be characterized by a topological invariant called the *Chern number* [75]. It was a remarkable discovery that in some systems like the fractional quantum Hall effect, it is related to physically measurable quantities [76, 77]. The problem of characterization becomes the much simpler problem of measuring these currents.

However, in other systems like lattice models there is no such physical relation. The information given by the Chern number is also limited, because it only tells that a particular topological phase exists. It tells nothing about the microscopics which influence the physics in any realistic system. For all practical purposes, one always wants to study the anyonic excitations directly. A prime example of this is the recent interferometric experiment on the non-Abelian fractional quantum Hall state [41]. Although the conductivity predicting a state with non-Abelian anyons had been measured to high accuracy [78], no one knew beforehand whether the non-Abelian anyons could actually be realized in an experiment, not to even talk of employing them for quantum information processing.

Our aim is to perform theoretically a similar direct study on the honeycomb lattice model. While the low-energy theory of the Abelian phase of the honeycomb

lattice model can be obtained using perturbation theory, no such prescription exists for the non-Abelian phase. For a model that is exactly solvable, one should be able to understand the non-Abelian anyons better than only through the Chern number, as done in the original work [62]. This is important for both theoretical and experimental reasons. The honeycomb lattice model is attractive for experiments, because it involves only simple interactions. The trade-off is that anyonic excitations are harder to identify. The microscopics of the model can endow them with non-topological properties, such as interactions in our case, that can smear out their anyonic character. Therefore, our original motivation was to do “The Dirty Work”, i.e. to derive explicitly the defining properties of the anyonic vortices, and to study at which length scales the topological properties emerge undressed by the microscopic physics. Only by understanding how the anyons arise from the microscopic model can one come up with schemes to control them.

Moreover, understanding the system beyond the Chern number is important, because interactions between anyons have recently been discovered to lead to new topological phases [24, 25]. When applied to the honeycomb lattice model, this theory of anyon-anyon interaction driven phase transitions suggested that the non-Abelian phase should give rise to a new phase with chiral Abelian anyons. Indeed, we found a sector of the model where this happens, which provided the first verification of the novel theory from a microscopic model.

Our aim was to go beyond mere verification. Since the honeycomb lattice model is now supporting three distinct topological phases, all with distinct characteristics, it provided an ideal setting to study phase transitions between them. To this end we considered the Fermi surface of the model as its different topologies can be related to different phases [79]. It provides a suitable platform to study the phase transitions as, unlike the Chern number, it evolves continuously under perturbations. Motivated by the success of low-energy field theory picture in graphene [80], we set out to study the Fermi surface evolution in terms of the low-energy theory of Dirac fermions. The hypothesis was that phase transition driving perturbations would lead to Fermi point

transport, which in the low-energy theory of Dirac fermions could be understood as being due to a coupling to gauge fields. By studying the transport we should then be able to obtain the critical behavior analytically.

The thesis is organized as follows:

Chapter 2: Kitaev's Honeycomb Lattice Model

In this chapter we review the honeycomb lattice model and the mapping to free Majorana fermions as originally introduced by Kitaev [62]. We generalize the solution to arbitrary vortex sectors. The relevant concepts to analyze the spectrum are introduced and the phase space of the vortex-free sector is reviewed. We introduce the Chern number as a characterization of the different topological phases and summarize the properties of the non-Abelian Ising anyons.

This chapter is partially based on the published collaborative work [71]. The analytic study of the generalized solution included in this thesis is by myself and Dr. Jiannis Pachos. The numerics at the end of the published paper are contributed by the NUI Maynooth group headed by Dr. Jiri Vala. These do not form part of the thesis.

Chapter 3: Non-Abelian Fusion Rules and Braid Statistics

In this chapter we employ the solution to arbitrary vortex sectors to explicitly demonstrate the characteristic non-Abelian fusion rules and braid statistics of the Ising anyons. We introduce first an equivalence between the vortex sectors and coupling configurations, which provides a method to physically implement vortex transport. We employ this to study the spectral evolution as the separation between the vortices is varied. Oscillating short-range interactions are discovered, and they are argued to reveal the characteristic fusion rules. Finally, we calculate the non-Abelian statistics as a vortex is transported around another. By considering various finite system sizes, we show how the braid statistics can be obtained as a Berry phase corresponding to the evolution of the eigenstates during the transport

Chapter 1. Introduction

process.

The first part concerning the fusion rules is based again on the published work [71], although the results and analysis here extend those of the published version. The second part on the braid statistics is based on the published work by myself and Dr. Jiannis Pachos [72].

Chapter 4: Going Beyond: A New Chiral Topological Phase

In this chapter we show that the full-vortex sector of the honeycomb lattice model supports a new topological phase with chiral Abelian anyons. We demonstrate that this new phase appears due to the anyon-anyon interactions discovered in Chapter 3. These give rise to a new band structure characterized by an emergent Hamiltonian symmetry. The phase transitions between the different topological phases are studied by considering the evolution of the Fermi surface under perturbations. We show that this is equivalent to considering the low-energy field theory of Dirac fermions coupled to gauge fields. Two distinct types of topological phase transitions are identified based on Hamiltonian symmetries and the extended phase space including the new phase is outlined.

This chapter is based on work with Dr. Jiannis Pachos, [73].

Chapter 5: Conclusions

In this final chapter we summarize and discuss our results. Their extensions as well as future problems are considered.

Chapter 2

Kitaev's Honeycomb Lattice Model

In this chapter we review the honeycomb lattice model of Kitaev [62]. In Section 2.1 we introduce the spin lattice model and consider the important local symmetries that underlie its analytic tractability. In Section 2.2 we present the mapping to free Majorana fermions, which enables the model to be solved exactly. The exact treatment of arbitrary vortex sectors is presented. As a verification of our method, in Section 2.3 we review the phase space of the vortex-free sector, which supports both Abelian and non-Abelian anyons. The different phases are characterized by the Chern number, which gives the anyonic properties of the vortices. As we are interested here only on the non-Abelian Ising anyons, their relevant properties are summarized. The vortex-free sector is simple enough to accommodate analytic treatment, but in general this is not possible. In Section 2.4 we discuss how to treat the eigenvalues and eigenvectors when the diagonalization is performed numerically.

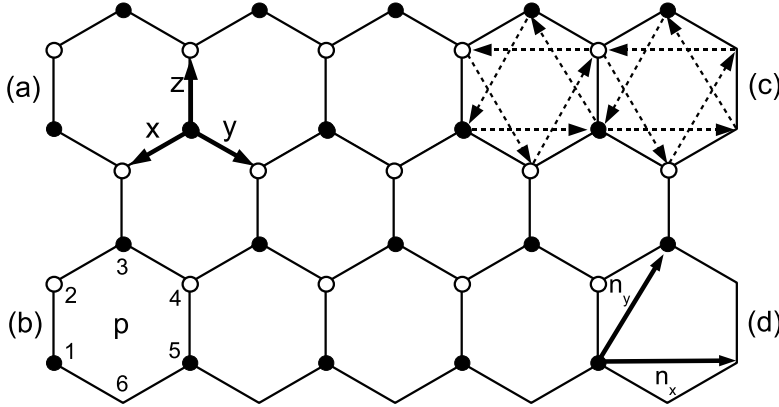


Figure 2.1: The bi-colourable honeycomb lattice with the black and white sites denoting the two triangular sublattices. (a) The links are labeled as x , y and z and oriented such that there is always an arrow pointing from black sites to white sites. (b) A single plaquette p with its six sites enumerated. (c) The oriented summation convention for the next to nearest neighbour interactions originating from the external magnetic field [62]. (d) The elementary unit cell with lattice basis vectors \mathbf{n}_x and \mathbf{n}_y .

2.1 The spin lattice model

The Kitaev's honeycomb lattice model, [62], consists of spin $\frac{1}{2}$ particles residing at the vertices of a honeycomb lattice. The spins interact according to the Hamiltonian

$$H = - \sum_{\alpha \in \{x,y,z\}} \sum_{(i,j) \in \alpha\text{-links}} J_{ij}^{\alpha} \sigma_i^{\alpha} \sigma_j^{\alpha} - K \sum_{(i,j,k)} \sigma_i^x \sigma_j^y \sigma_k^z, \quad (2.1)$$

where J_{ij}^{α} are positive nearest neighbour couplings on links (ij) , and $\alpha = x, y$ or z depending on the link's orientation (see Figure 2.1(a) for link labeling). The second term is an effective magnetic field of magnitude K . The sum runs over the sites such that every plaquette p contributes the six terms

$$\begin{aligned} \sum_{(i,j,k) \in p} \sigma_i^x \sigma_j^y \sigma_k^z &= \sigma_1^z \sigma_2^y \sigma_3^x + \sigma_2^x \sigma_3^z \sigma_4^y + \sigma_3^y \sigma_4^x \sigma_5^z + \\ &\quad \sigma_4^z \sigma_5^y \sigma_6^x + \sigma_5^x \sigma_6^z \sigma_1^y + \sigma_6^y \sigma_1^x \sigma_2^z, \end{aligned}$$

where the sites have been enumerated as shown in Figure 2.1(b). This term can be obtained as a third order term in a perturbative expansion when an anisotropic weak (Zeeman) magnetic field of the form $H_h = \sum_i \mathbf{h} \cdot \boldsymbol{\sigma}_i$ is applied. In this case the couplings are given by $K \approx \frac{h^x h^y h^z}{(J_{ij}^\alpha)^2}$, where one assumes all the couplings J_{ij}^α to be roughly equal. The model approximates the one with a Zeeman term when $h^\alpha \ll J_{ij}^\alpha$, but in general one can regard (2.1) also as an independent model.

The physical motivation to add this term is that like the Zeeman term it explicitly breaks the time-reversal invariance, while unlike the Zeeman term it preserves the exact solvability of the model. To be precise, time-reversal symmetry is described by a an anti-linear unitary operator \hat{T} , which acts on Pauli operators as

$$\hat{T} \sigma_i^\alpha \hat{T}^\dagger = -\sigma_i^\alpha. \quad (2.2)$$

Any product of an even number of Pauli operators with real coefficients will respect the time-reversal symmetry, whereas any odd product, such as the Zeeman or the three-spin term, will violate it. The advantage of using a Hamiltonian with the three-spin coupling (2.1) is that it has the important local symmetries

$$[H, \hat{w}_p] = 0, \quad \left([\hat{w}_p, \hat{w}_{p'}] = 0, \quad \prod_p \hat{w}_p = \mathbb{1} \right), \quad (2.3)$$

where $\hat{w}_p = \sigma_1^x \sigma_2^y \sigma_3^z \sigma_4^x \sigma_5^y \sigma_6^z$ are Hermitian *plaquette operators*. The product is over all plaquettes p and this constraint applies only when the system is defined on a compact manifold. These local symmetries are at the heart of the exact solvability of the model. Since \hat{w}_p are conserved quantities, the Hilbert space \mathcal{L} of N spins on an infinite plane can be partitioned into $2^{N/2}$ sectors \mathcal{L}_w of dimension $2^{N/2}$, each labeled by a distinct pattern $w = \{w_p\}$ of the eigenvalues $w_p = \pm 1$. The physics of each sector can be considered independently and in the corresponding subspaces the three-spin term gives the leading order contribution from an external weak magnetic field.

2.2 Mapping to free Majorana fermions

The Hamiltonian can be brought to a quadratic form by representing the spin operators with Majorana fermions. Let us introduce two complex fermionic modes $a_{1,i}$ and $a_{2,i}$ residing at each lattice site i . These can be written in terms of four Majorana fermions by

$$c_i = a_{1,i} + a_{1,i}^\dagger, \quad b_i^x = i(a_{1,i}^\dagger - a_{1,i}), \quad b_i^y = a_{2,i} + a_{2,i}^\dagger, \quad b_i^z = i(a_{2,i}^\dagger - a_{2,i}), \quad (2.4)$$

where now all b_i^α and c_i anti-commute with each other and satisfy $b_i^{\alpha\dagger} = b_i^\alpha$, $c_i^\dagger = c_i$. Let us represent the spin matrices at site i in terms of the Majorana fermions by

$$\sigma_i^\alpha = i b_i^\alpha c_i. \quad (2.5)$$

This representation respects the algebra of the Pauli matrices if one demands in addition that the states in the physical space $|\Psi\rangle \in \mathcal{L}$ have to satisfy

$$D_i |\Psi\rangle = |\Psi\rangle, \quad D_i \equiv b_i^x b_i^y b_i^z c_i, \quad [D_i, \sigma_j^\alpha] = 0. \quad (2.6)$$

This follows from the operator identity $\mathbb{1} = i\sigma_i^x \sigma_i^y \sigma_i^z = b_i^x b_i^y b_i^z c_i$. Observing that using (2.4) we can write $D_i = (1 - 2a_{1,i}^\dagger a_{1,i})(1 - 2a_{2,i}^\dagger a_{2,i})$, the constraint D_i can be interpreted as performing a projection from the four-dimensional space spanned by two complex fermion modes a_1 and a_2 onto a two-dimensional subspace where both of the complex fermionic modes are either empty or full. In this subspace our representation of the spin operators is faithful.

Employing (2.5) the Hamiltonian terms become

$$\sigma_i^\alpha \sigma_j^\alpha = -i \hat{u}_{ij} c_i c_j \quad \text{and} \quad \sigma_i^x \sigma_j^y \sigma_k^z = -i \hat{u}_{ik} \hat{u}_{jk} D_k c_i c_j,$$

where we have defined the anti-symmetric Hermitian *link operators*

$$\hat{u}_{ij} = i b_i^\alpha b_j^\alpha, \quad \left(\hat{u}_{ij} = -\hat{u}_{ji}, \quad \hat{u}_{ij}^2 = 1, \quad \hat{u}_{ij}^\dagger = \hat{u}_{ij} \right), \quad (2.7)$$

with $\alpha = x, y, z$ depending on the type of link (ij) . Consequently, in the physical space \mathcal{L} the Hamiltonian (2.1) takes the quadratic form

$$H = \frac{i}{4} \sum_{i,j} \hat{A}_{ij} c_i c_j, \quad \hat{A}_{ij} = 2J_{ij} \hat{u}_{ij} + 2K \sum_k \hat{u}_{ik} \hat{u}_{jk}. \quad (2.8)$$

The oriented nearest (the first term of \hat{A}_{ij}) and next-to-nearest (the second term of \hat{A}_{ij}) neighbour summations are expressed conveniently pictorially in Figures 2.1(a) and 2.1(c), respectively. The antisymmetry of the \hat{u}_{ij} is taken into account by using a convention such that one assigns an overall $+$ ($-$) to every term involving sites i and j when the arrow points from i to j (j to i). If two sites are not connected by an arrow the corresponding \hat{A}_{ij} element is zero.

The honeycomb lattice model as a lattice gauge theory

In the fermionized picture the Hamiltonian acquires a new physical interpretation. One can verify that the Hamiltonian acts on the physical subspace, i.e. $[H, D_i] = 0$, and that the link operators are local symmetries, i.e. $[H, \hat{u}_{ij}] = 0$. However, since $\{\hat{u}_{ij}, D_i\} = 0$, sectors labeled by their eigenvalue patterns $u = \{u_{ij} = \pm 1\}$ are not part of the physical space \mathcal{L} . On the other hand, the plaquette operators (2.3), which still commute with the Hamiltonian, become the products of the link operators and act in \mathcal{L} ,

$$\hat{w}_p = \prod_{i,j \in p} \hat{u}_{ij}, \quad [\hat{w}_p, D_i] = 0. \quad (2.9)$$

These observations allow for the following lattice gauge theory interpretation. The link operators \hat{u}_{ij} can be thought of as classical Z_2 gauge fields with local gauge transformations D_i . As a single plaquette is the smallest loop that can be constructed from the gauge fields \hat{u}_{ij} , the gauge invariant plaquette operators \hat{w}_p can be identified with the Wilson loop operators. Consequently, the eigenvalues $w_p = -1$ can be interpreted as having a π -flux *vortex* living on the plaquette p . The different physical sectors of the model are then equivalent to configurations of vortices, that are created by fixing the gauge u , i.e. the pattern of the eigenvalues of the gauge

fields. The eigenvalues $u_{ij} = -1$ can be visualized as an unphysical string passing through the link (ij) , that either connects two vortices or belongs to a loop. The unphysicality follows from the constraint (2.6), which can be always satisfied by performing the projection

$$|\Psi_w\rangle = \mathbf{D}|\Psi_u\rangle, \quad \mathbf{D} = \prod_{i=1}^N \left(\frac{\mathbb{1} + D_i}{2} \right), \quad (2.10)$$

where $|\Psi_u\rangle$ is some state belonging to a gauge sector u . Due to the anti-commutation of D_i and \hat{u}_{ij} , the physical state $|\Psi_w\rangle \in \mathcal{L}$ will be an equal amplitude superposition of all loops and strings compatible with the vortex sector w .

2.3 Solution for arbitrary periodic vortex configurations

Let us now consider in more detail the form of Hamiltonian (2.8) for general periodic vortex sectors and its diagonalization using a Fourier transformation. For convenience, but without affecting the physics, the honeycomb geometry is deformed by choosing the lattice basis vectors to be $\mathbf{n}_x = (1, 0)$ and $\mathbf{n}_y = (0, 1)$. To study general vortex sectors, we define a (L_x, L_y) -unit cell, containing $2L_xL_y$ sites and assume u to be fixed such that it is translationally invariant with respect to

$$\mathbf{v}_x = L_x\mathbf{n}_x = (L_x, 0), \quad \mathbf{v}_y = L_y\mathbf{n}_y = (0, L_y). \quad (2.11)$$

This cell is illustrated in Figure 2.2. For convenience, the labeling of site i on the original honeycomb lattice can be broken down to $i = (\mathbf{r}, \mathbf{l}, \lambda)$, where \mathbf{r} is a vector in basis $\{\mathbf{v}_x, \mathbf{v}_y\}$ indicating the location of the unit cell, the vector $\mathbf{l} = (l_x, l_y)$ in basis $\{\mathbf{n}_x, \mathbf{n}_y\}$ specifies a particular z -link inside the unit cell and $\lambda = b, w$ denotes the sublattice the site belongs to.

A Fourier transformation of the operators $c_{\lambda, \mathbf{l}, \mathbf{r}}$ with respect to \mathbf{r} is given by

$$c_{\lambda, \mathbf{l}, \mathbf{r}} = \sqrt{2} \int_{\text{BZ}}^{(L_x, L_y)} d^2p e^{i\mathbf{p}\cdot\mathbf{r}} c_{\lambda, \mathbf{l}, \mathbf{p}}, \quad (2.12)$$

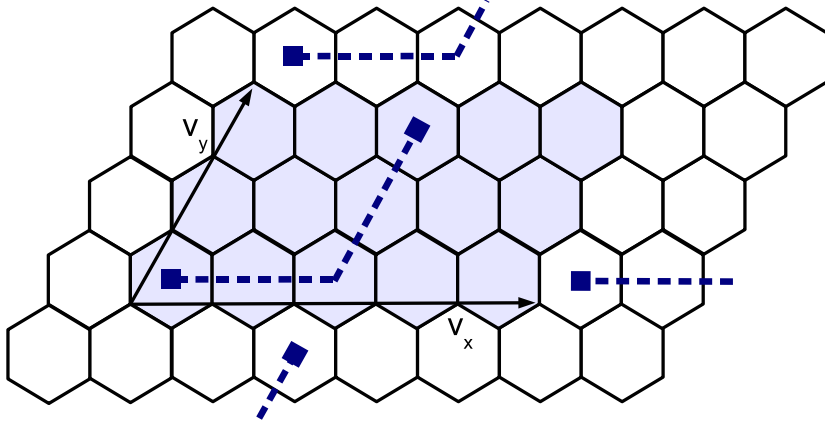


Figure 2.2: An illustration of the generalized (L_x, L_y) -unit cell using a $(5, 3)$ -unit cell (shaded plaquettes) containing two vortices (blue squares). The gauge sector u giving rise to this vortex configuration is given, for instance, by setting $u_{ij} = -1$ on the links crossed by the string connecting the vortices (blue dashed line), while $u_{ij} = 1$ on all other links. This configuration is periodic with respect to $\mathbf{v}_x = (5, 0)$ and $\mathbf{v}_y = (0, 3)$, with the pattern u repeated all across the infinite lattice.

where the integral is over the first Brillouin zone corresponding to the (L_x, L_y) -unit cell

$$\int_{\text{BZ}}^{(L_x, L_y)} d^2p \equiv \int_{-\pi/L_x}^{\pi/L_x} \frac{dp_x}{\sqrt{2\pi/L_x}} \int_{-\pi/L_y}^{\pi/L_y} \frac{dp_y}{\sqrt{2\pi/L_y}}. \quad (2.13)$$

In the Fourier basis the Hamiltonian (2.8) is reduced to the canonical form

$$H = \frac{1}{2} \int_{\text{BZ}}^{(L_x, L_y)} d^2p \begin{pmatrix} \mathbf{c}_{b,\mathbf{p}} \\ \mathbf{c}_{w,\mathbf{p}} \end{pmatrix}^\dagger \begin{pmatrix} h_{bb,\mathbf{p}} & h_{bw,\mathbf{p}} \\ h_{bw,\mathbf{p}}^\dagger & -h_{bb,\mathbf{p}}^T \end{pmatrix} \begin{pmatrix} \mathbf{c}_{b,\mathbf{p}} \\ \mathbf{c}_{w,\mathbf{p}} \end{pmatrix}, \quad (2.14)$$

where $\mathbf{c}_{\lambda,\mathbf{p}}^\dagger = (c_{\lambda,(1,1),\mathbf{p}}^\dagger, \dots, c_{\lambda,(L_x, L_y),\mathbf{p}}^\dagger)$, and $h_{bb,\mathbf{p}}$ and $h_{bw,\mathbf{p}}$ are $L_x L_y \times L_x L_y$ matrices describing the nearest and next-to-nearest interactions, respectively.

The elements of the matrices $h_{bb,\mathbf{p}}$ and $h_{bw,\mathbf{p}}$ can be derived by considering all the allowed couplings inside the unit cell. All terms describing couplings between sites i and i' belonging to the unit cell, i.e. when $i = (\mathbf{r}, \mathbf{l}, \lambda)$ and $i' = (\mathbf{r}, \mathbf{l}', \lambda')$, follow straight from (2.8). On the other hand, when $\mathbf{r}' = \mathbf{r} + m\mathbf{v}_x + n\mathbf{v}_y$, the corresponding terms acquire due to Fourier transform, (2.12), the extra phases $e^{i\mathbf{p} \cdot (m\mathbf{v}_x + n\mathbf{v}_y)}$ with

Chapter 2. Kitaev's Honeycomb Lattice Model

$m, n = \pm 1$. Carrying out this analysis for arbitrary (L_x, L_y) -unit cells, one finds that the non-vanishing elements of $h_{bw, \mathbf{p}}$ and $h_{wb, \mathbf{p}} = h_{bw, \mathbf{p}}^\dagger$ are given explicitly by

$$\mathbf{c}_b^\dagger h_{bw} \mathbf{c}_w = 2i \sum_{\mathbf{l}=(1,1)}^{(L_x, L_y)} \begin{pmatrix} +u_{l,l} & J_z & c_{b,l}^\dagger c_{w,l} \\ +u_{l,l-n_x} & J_x e^{i\delta(l_x-1)\mathbf{p}\cdot\mathbf{v}_x} & c_{b,l}^\dagger c_{w,l-n_x} \\ +u_{l,l-n_y} & J_y e^{i\delta(l_y-1)\mathbf{p}\cdot\mathbf{v}_y} & c_{b,l}^\dagger c_{w,l-n_y} \end{pmatrix}, \quad (2.15)$$

and

$$\mathbf{c}_w^\dagger h_{wb} \mathbf{c}_b = 2i \sum_{\mathbf{l}=(1,1)}^{(L_x, L_y)} \begin{pmatrix} -u_{l,l} & J_z & c_{w,l}^\dagger c_{b,l} \\ -u_{l,l+n_x} & J_x e^{-i\delta(l_x-L_x)\mathbf{p}\cdot\mathbf{v}_x} & c_{w,l}^\dagger c_{b,l+n_x} \\ -u_{l,l+n_y} & J_y e^{-i\delta(l_y-L_y)\mathbf{p}\cdot\mathbf{v}_y} & c_{w,l}^\dagger c_{b,l+n_y} \end{pmatrix}. \quad (2.16)$$

The addition in the indices $\mathbf{l} = (l_x, l_y)$ is understood $(l_x \bmod L_x, l_y \bmod L_y)$ and $\delta(x) = 1$ for $x = 0$ and $\delta(x) = 0$ otherwise. Likewise, the diagonal blocks $h_{bb, \mathbf{p}}$ and $h_{ww, \mathbf{p}} = -h_{bb, \mathbf{p}}^T$ originating from the three-spin term are given by

$$\mathbf{c}_b^\dagger h_{bb} \mathbf{c}_b = 2iK \sum_{\mathbf{l}=(1,1)}^{(L_x, L_y)} \begin{pmatrix} +u_{l,l+n_y}^l & e^{-i\delta(l_y-L_y)\mathbf{p}\cdot\mathbf{v}_y} & c_{b,l}^\dagger c_{b,l+n_y} \\ -u_{l,l-n_x+n_y}^{l-n_x} & e^{i\delta(l_x-1)\mathbf{p}\cdot\mathbf{v}_x} e^{-i\delta(l_y-L_y)\mathbf{p}\cdot\mathbf{v}_y} & c_{b,l}^\dagger c_{b,l-n_x+n_y} \\ -u_{l,l+n_x}^l & e^{-i\delta(l_x-L_x)\mathbf{p}\cdot\mathbf{v}_x} & c_{b,l}^\dagger c_{b,l+n_x} \\ +u_{l,l+n_x-n_y}^{l-n_y} & e^{-i\delta(l_x-L_x)\mathbf{p}\cdot\mathbf{v}_x} e^{i\delta(l_y-1)\mathbf{p}\cdot\mathbf{v}_y} & c_{b,l}^\dagger c_{b,l+n_x-n_y} \\ +u_{l,l-n_x}^{l-n_x} & e^{i\delta(l_x-1)\mathbf{p}\cdot\mathbf{v}_x} & c_{b,l}^\dagger c_{b,l-n_x} \\ -u_{l,l-n_y}^{l-n_y} & e^{i\delta(l_y-1)\mathbf{p}\cdot\mathbf{v}_y} & c_{b,l}^\dagger c_{b,l-n_y} \end{pmatrix}, \quad (2.17)$$

and

$$\begin{aligned}
 \mathbf{c}_w^\dagger h_{ww} \mathbf{c}_w = & 2iK \sum_{l=(1,1)}^{(L_x, L_y)} \\
 & \left(\begin{array}{lll}
 -u_{l, l+n_y}^{l+n_y} & e^{-i\delta(l_y-L_y)\mathbf{p}\cdot\mathbf{v}_y} & \mathcal{C}_{w,l}^\dagger \mathcal{C}_{w, l+n_y} \\
 +u_{l, l-n_x+n_y}^{l+n_y} & e^{i\delta(l_x-1)\mathbf{p}\cdot\mathbf{v}_x} e^{-i\delta(l_y-L_y)\mathbf{p}\cdot\mathbf{v}_y} & \mathcal{C}_{w,l}^\dagger \mathcal{C}_{w, l-n_y+n_y} \\
 +u_{l, l+n_x}^{l+n_x} & e^{-i\delta(l_x-L_x)\mathbf{p}\cdot\mathbf{v}_x} & \mathcal{C}_{w,l}^\dagger \mathcal{C}_{w, l+n_x}, \\
 -u_{l, l+n_x-n_y}^{l+n_x} & e^{-i\delta(l_x-L_x)\mathbf{p}\cdot\mathbf{v}_x} e^{i\delta(l_y-1)\mathbf{p}\cdot\mathbf{v}_y} & \mathcal{C}_{w,l}^\dagger \mathcal{C}_{w, l+n_x-n_y} \\
 -u_{l, l-n_x}^l & e^{i\delta(l_x-1)\mathbf{p}\cdot\mathbf{v}_x} & \mathcal{C}_{w,l}^\dagger \mathcal{C}_{w, l-n_x} \\
 +u_{l, l-n_y}^l & e^{i\delta(l_y-1)\mathbf{p}\cdot\mathbf{v}_y} & \mathcal{C}_{w,l}^\dagger \mathcal{C}_{w, l-n_y} \end{array} \right), \quad (2.18)
 \end{aligned}$$

where we have used the short-hand notation $u_{k,l}^j \equiv u_{k,j} u_{j,l}$.

These expressions give the most general Hamiltonian for periodic vortex sectors, that can be studied at the thermodynamical limit. After choosing a particular vortex sector, (2.9), by fixing the $u_{ij} = \pm 1$ on all links inside the unit cell, the Hamiltonian can be readily diagonalized. This gives in general

$$H = \int_{\text{BZ}}^{(L_x, L_y)} d^2p \left(\sum_{i=1}^{L_x L_y} E_{i,\mathbf{p}} b_{i,\mathbf{p}}^\dagger b_{i,\mathbf{p}} - \sum_{i=1}^{L_x L_y} \frac{E_{i,\mathbf{p}}}{2} \right), \quad (2.19)$$

where $b_{i,\mathbf{p}}$ are $L_x L_y$ fermionic mode operators and $E_{i,\mathbf{p}}$ are the positive eigenvalues corresponding to each momentum mode. In an n -vortex sector, the ground state $|\Psi_0^{nv}\rangle$ with energy E_0^{nv} , and the lowest lying excited state $|\Psi_{i,\mathbf{p}_0}^{nv}\rangle$ on the i th band with energy E_i^{nv} are given by

$$|\Psi_0^{nv}\rangle = \mathbf{D} \prod_{i=1}^{L_x L_y} \prod_{-\pi \leq p_x, p_y \leq \pi} b_{i,\mathbf{p}} |\phi\rangle, \quad E_0^{nv} = - \int_{\text{BZ}}^{(L_x, L_y)} d\mathbf{p} \sum_{i=1}^{L_x L_y} \frac{E_{i,\mathbf{p}}}{2}, \quad (2.20)$$

and

$$|\Psi_{i,\mathbf{p}_0}^{nv}\rangle = \mathbf{D} b_{i,\mathbf{p}_0}^\dagger |\Psi_0^{nv}\rangle, \quad E_i^{nv} = \Delta_i^{nv} + E_0^{nv}, \quad (2.21)$$

respectively. Here \mathbf{D} performs the gauge symmetrization (2.10), $|\phi\rangle$ is an arbitrary reference state and Δ_i^{nv} is the energy gap with respect to the ground state defined

by $\Delta_i^{nv} \equiv \min_{\mathbf{p}} E_{i,\mathbf{p}}^{nv}$.

2.4 The phase diagram in the absence of vortices

The phase diagram in the absence of vortices has been studied in the original work [62]. In this section we reproduce these results using our more general Hamiltonian (2.14), and outline the previously known phase space by studying the behavior of the energy gaps. Further, we introduce the Chern number, which can be used to characterize the different topologically ordered phases appearing in the honeycomb lattice model.

The vortex-free configuration ($w_p = 1$ on all plaquettes) can be created, for instance, by setting $u_{ij} = 1$ on all links in (2.15)-(2.18). Let us also assume that all the couplings J_x , J_y and J_z have uniform values on all x -, y - and z -links, respectively. The resulting system is periodic with respect to each z -link. Choosing then simply a $(1, 1)$ -unit cell gives a 2×2 Hamiltonian, (2.14), with

$$\begin{aligned} h_{bw,\mathbf{p}} &= 2i (J_z + J_x e^{ip_x} + J_y e^{ip_y}) = if(\mathbf{p}), \\ h_{bb,\mathbf{p}} &= 4K (\sin(p_x - p_y) + \sin(p_y) - \sin(p_x)) = g(\mathbf{p}). \end{aligned}$$

The Hamiltonian is diagonal, (2.19), in the basis of the fermionic operators

$$b_{\mathbf{p}} = \Lambda_{\mathbf{p}} \left(c_{2,\mathbf{p}} + i \frac{E_{\mathbf{p}} - g_{\mathbf{p}}}{f_{\mathbf{p}}} c_{1,\mathbf{p}} \right), \quad \Lambda_{\mathbf{p}}^2 = \frac{|f_{\mathbf{p}}|^2}{(E_{\mathbf{p}} + g_{\mathbf{p}})^2 + |f_{\mathbf{p}}|^2}, \quad (2.22)$$

where the eigenvalues $\pm E_{\mathbf{p}}$ are given by

$$\begin{aligned} E_{\mathbf{p}} &= \sqrt{|f_{\mathbf{p}}|^2 + g_{\mathbf{p}}^2}, \\ |f_{\mathbf{p}}|^2 &= 4(J_x^2 + J_y^2 + J_z^2 + 2(J_x J_z \cos p_x + J_x J_y \cos(p_x - p_y) + J_y J_z \cos p_y)), \\ g_{\mathbf{p}}^2 &= 16K^2 (\sin p_y - \sin p_x + \sin(p_x - p_y))^2. \end{aligned} \quad (2.23)$$

These expressions agree with [62].

There it was shown that in the vortex-free sector the honeycomb lattice model

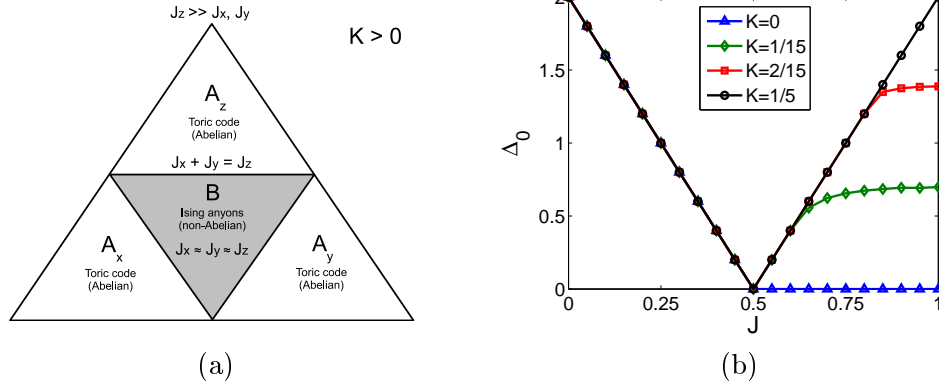


Figure 2.3: (a) An illustration of the vortex-free sector phase diagram with four distinct phases A_x, A_y, A_z and B . The phases A_α occurs when the couplings of type $J_\alpha \gg J_\beta, J_\gamma$ and the phase B when they all roughly equal. The boundaries between the phases A_α and B are given by $J_\alpha = J_\beta + J_\gamma$. The A_α phases support Abelian toric code anyons ($\nu = 0$), whereas for $K > 0$ the B phase supports non-Abelian Ising anyons ($\nu = -1$). (b) The behavior of the energy gap $\Delta^{0\nu}$ across the transition between A_z and B phases. Here $J = J_x = J_y$ when $J_z = 1$. The phase A_z is always gapped with $\Delta^{0\nu}$ depending only on J , whereas the B phase is only gapped when $K > 0$. The phase transition occurs for all K at $J = \frac{1}{2}$ where the gap vanishes and the Chern number changes.

exhibits four distinct phases denoted by A_x, A_y, A_z and B . These appear for different values of the couplings J_α such that the system is in the B -phase when one violates all the inequalities

$$|J_y| + |J_z| \leq |J_x|, \quad |J_x| + |J_z| \leq |J_y|, \quad |J_x| + |J_y| \leq |J_z|. \quad (2.24)$$

The phase boundaries are given by the equalities and the phases A_α occur when only $|J_\beta| + |J_\gamma| \leq |J_\alpha|$ holds and the other two inequalities are violated. The resulting phase space is illustrated in Figure 2.3(a).

This analysis of the phase space relies on the behavior of the *energy gap*, i.e. the energy of the lowest lying state above the ground state,

$$\Delta^{0\nu} = \min_{\mathbf{p}} E_{\mathbf{p}}, \quad (2.25)$$

as a function of the parameters J_α and K . Stable topological phases exist only for

a non-vanishing gap, with points of vanishing gap signaling phase transitions. We plot in Figure 2.3(b) the behavior of the gap Δ^{0v} as calculated from (2.23). The A_α phases are always gapped, whereas the B -phase is gapped only when $K \neq 0$. In the first the gap depends only on J_α whereas in the latter it depends on both J_α and K with $\Delta^{0v} = 6\sqrt{3}K$ when $J_x = J_y = J_z = 1$. The gap vanishes always at $J_z = J_x + J_y$ as expected from (2.24). The different behavior of the gap is due to topologically distinct Fermi surfaces in the phases A_α and B . We will return to discuss their role in the characterization of the phases in Chapter 4.

2.4.1 The Chern number

The study of the energy gap reveals the phase space structure, but does not tell anything about the properties of the phases. To probe whether they are topologically ordered, one can study whether the ground state degeneracy depends on the topology of the space [74], whether the entanglement entropy has a constant term [17, 18], or ultimately study directly the statistics of the excitations [94]. These all can be connected to the properties of the ground state, which can be captured by calculating by the so called spectral *Chern number* ν . It is a topological invariant whose importance to topologically ordered phases was first appreciated in the context of quantum Hall effect [75, 76]. Later it was shown to characterize also more general systems [77, 82, 83].

The Chern number can take only integer values, each corresponding to a different phase with different anyonic properties. In a non-interacting gapped free-fermion system with broken time-reversal symmetry, it gives the following information on the statistical properties of the vortices [83]:

- $\nu = 0$: non-chiral Abelian anyons (e.g. $\nu = 0$ for the toric code)
- ν even: chiral Abelian anyons
- ν odd: chiral non-Abelian anyons (e.g. $\nu = \pm 1$ for the Ising anyons)

In the honeycomb lattice model, there exists altogether eight different anyon models,

that correspond to different ν 's. These have been catalogued in [62].

The Chern number is of particular importance in quantum Hall systems, where its value is directly proportional to the physically measurable off-diagonal conductivity [76]. In the honeycomb lattice model there is no direct physical analogue, but it is still useful in the theoretical characterization of the different phases. It can be explicitly calculated from the eigenstates using the definition [84]

$$\nu = \frac{1}{2\pi i} \int_{BZ} d^2p (\partial_{p_x} \mathcal{A}_{y,\mathbf{p}} - \partial_{p_y} \mathcal{A}_{x,\mathbf{p}}), \quad (2.26)$$

where $\mathcal{A}_{\alpha,\mathbf{p}} = \langle \Psi_{0,\mathbf{p}} | \partial_{p_\alpha} | \Psi_{0,\mathbf{p}} \rangle$ and $|\Psi_{0,\mathbf{p}}\rangle$ is a momentum component of the ground state (2.20). Mathematically, the Chern number classifies the $U(L_x L_y)$ fibre bundle above the Brillouin zone formed by the $L_x L_y$ occupied modes belonging to the ground state (2.20).

For the vortex-free case $|\Psi_{0,\mathbf{p}}\rangle = |\psi_{1,\mathbf{p}}^-\rangle$ with the analytic expressions (2.22) and the Chern number can be evaluated analytically. However, in general the analytic expressions are not available and the Chern number must be evaluated numerically. A particularly useful form is given in [85]. Using an $n \times n$ mesh for the Brillouin zone, the Chern number (2.26) can be written as

$$\nu = \frac{1}{2\pi} \sum_{i,j=1}^{n-1} \langle \Psi_{i,j} | \Psi_{i+1,j} \rangle \langle \Psi_{i+1,j} | \Psi_{i+1,j+1} \rangle \langle \Psi_{i+1,j+1} | \Psi_{i,j+1} \rangle \langle \Psi_{i,j+1} | \Psi_{i,j} \rangle, \quad (2.27)$$

where $|\Psi_{i,j}\rangle = |\Psi_{0,(p_x^i, p_y^j)}\rangle$ with $p_\alpha^i = -\frac{\pi}{L_\alpha} + \frac{2\pi}{L_\alpha} \frac{i-1}{n-1}$. This form is particularly convenient for calculations involving sparse vortex sectors. Evaluating the Chern number for the four phases shown in Figure 2.3(a), we obtain $\nu = 0$ for A_x , A_y and A_z , which means that the vortices behave as non-chiral Abelian toric code anyons. On the other hand, for the phase B one obtains $\nu = \pm 1$ (the sign depends on the sign of K), which corresponds to chiral non-Abelian Ising anyons.

It was also shown in [85] that the Chern number is robust with respect to the discretization of the momentum space, i.e. to the mesh size n . This means the phases characterized by it should be insensitive to the system size, with topological

order persisting down to small systems. This is a point we will be challenging from a physical point of view in this thesis. Although the Chern number can indeed change only at the phase transitions, we will show that system size does affect significantly the physics. Without inducing a phase transition, these microscopic effects affect the excitation spectrum and its properties, depriving it from the expected anyonic behavior.

2.4.2 Ising anyons

By definition, anyons are particles obeying statistics that is neither bosonic or fermionic. This exotic statistics leads to the anyons being labeled by some conserved *topological quantum numbers*. Usually when talking about the low-energy theories of topologically ordered phases, one talks in general about *anyon models*. These refer to a set of all particles appearing in the system that carry conserved quantum numbers. An anyon model describes the conservation of these quantum numbers as well as the mutual statistics of the particles, some which are anyonic and some other bosonic or fermionic. Mathematically these concepts are best unified through category theory [62]. In this thesis we are interested in the so called non-Abelian Ising anyons that appear in the B -phase of the honeycomb lattice model. Their defining properties as an anyon model are summarized below.

The Ising anyon model has three types of *particles types*: 1 (vacuum), ψ (fermion) and σ (non-Abelian anyon). These labels can be thought of as the topological quantum numbers. The *fusion rules*, i.e. conservation laws for the quantum numbers, are given by

$$\psi \times \psi = 1, \quad \psi \times \sigma = \sigma, \quad \sigma \times \sigma = 1 + \psi, \quad (2.28)$$

with the vacuum fusing trivially with the other particle types. The fusion rule for the σ 's implies that there is a degree of freedom associated with the different ways a number of σ 's can fuse. This is a unique property of non-Abelian anyons. As the global quantum numbers have to be always conserved, this degree of freedom appears when there is more than one way of fusing n σ particles to a given particle

a. To illustrate this, consider four σ particles, for which the repeated associative application of (2.28) gives

$$\sigma \times \sigma \times \sigma \times \sigma = 1 + 1 + \psi + \psi. \quad (2.29)$$

This means that there are two distinct ways the four σ 's can fuse to either the vacuum 1 or to the fermion ψ .

These fusion degrees of freedom, or *fusion channels*, can be encoded in the *fusion space* V_{σ^4} . Due to the two possible global sectors 1 and ψ , it breaks down to two orthogonal two-dimensional subspaces, $V_{\sigma^4} = V_{\sigma^4}^1 \oplus V_{\sigma^4}^\psi$. The bases in $V_{\sigma^4}^a$ are given by the states associated with different intermediate fusion outcomes with respect to some chosen fusion ordering. For future purposes, let us consider $V_{\sigma^4}^\psi$ and choose a pair-wise fusion channel basis, where the basis states are associated with the following processes:

$$\begin{aligned} |\Psi_1\rangle : & \quad (\sigma \times \sigma)_1 \times (\sigma \times \sigma)_2 \rightarrow \psi \times 1 = \psi, \\ |\Psi_2\rangle : & \quad (\sigma \times \sigma)_1 \times (\sigma \times \sigma)_2 \rightarrow 1 \times \psi = \psi. \end{aligned} \quad (2.30)$$

These are illustrated diagrammatically in Figure 2.4(a). The state $|\Psi_1\rangle$ ($|\Psi_2\rangle$) corresponds to pair 1 (2) fusing to a ψ , with the other fusing to vacuum. In both cases the global sector is ψ .

Different choices for the fusion order of the σ particles correspond to different bases. As there are only a finite number of fusion order choices for a finite number of particles, all the bases are related by so called *F-moves*, whose action is illustrated in Figure 2.4(b). These are a finite set of unitaries that act in the fusion space. They are obtained by solving a set equations known as pentagon equations [62]. For the fusion rules (2.28), the non-trivial *F-moves* acting in $V_{\sigma^4}^\psi$ are given by

$$F \equiv F_{\sigma^4}^\psi = \frac{1}{\sqrt{2}} \begin{pmatrix} 1 & 1 \\ 1 & -1 \end{pmatrix}, \quad \bar{F} \equiv F_{\sigma\psi\sigma}^\psi = F_{\psi\sigma\psi}^\sigma = -\mathbb{1}, \quad (2.31)$$

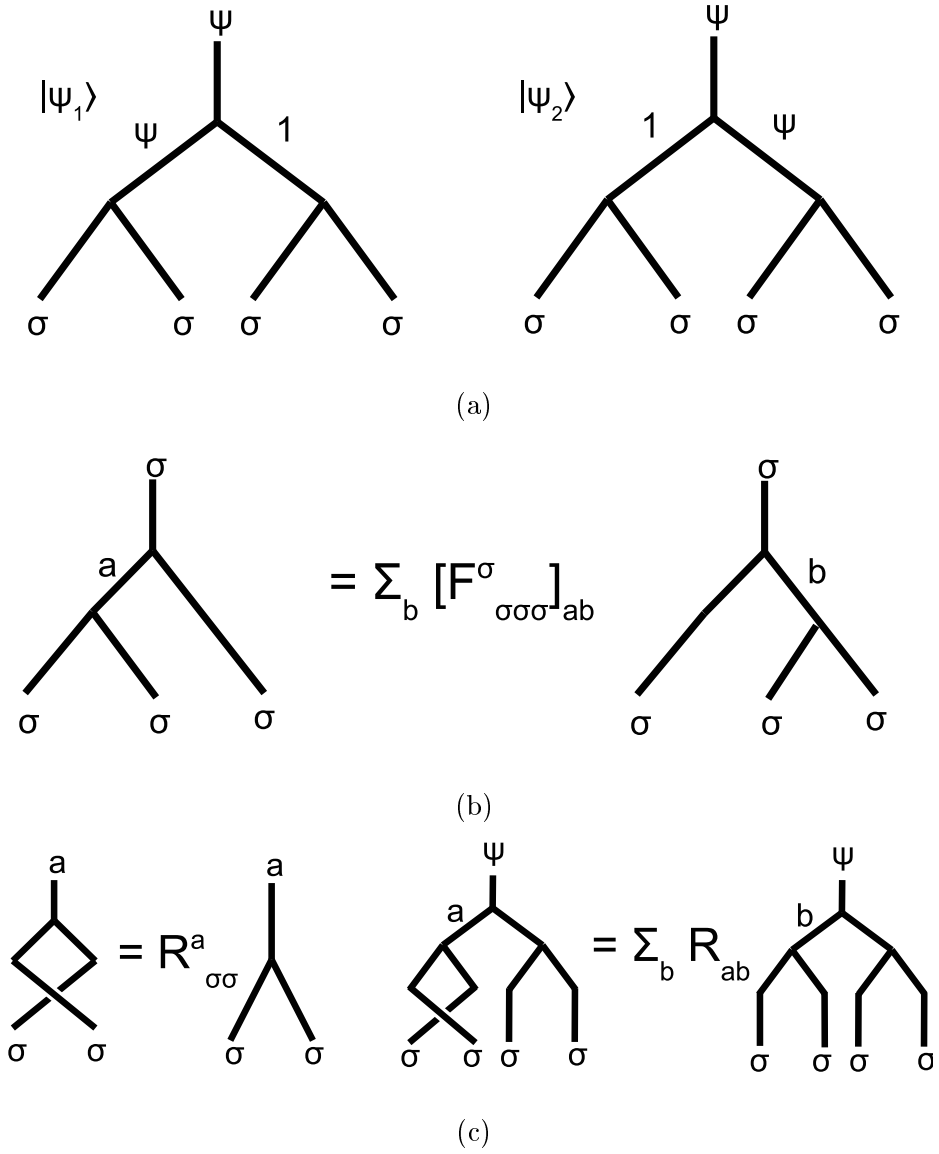


Figure 2.4: Diagrammatic representations of the topological properties of anyons. The diagrams represent world lines of the particles with time flowing upwards. (a) The basis in $V_{\sigma^4}^\psi$ is chosen such that the state $|\psi_i\rangle$ corresponds to pair i fusing to a ψ . (b) Basis changes are implemented by fusing the anyons in different orders. The F -move $F_{\sigma^3}^\sigma \equiv F_{\sigma^4}^\psi$ gives the expansion of the state in the new basis in terms of the original basis states. (c) When two σ 's are exchanged clockwise, the braid matrices $R_{\sigma\sigma}^a$ assign different phases depending on the fusion outcome a . In the fusion space $V_{\sigma^4}^\psi$ it acts as a diagonal matrix whenever the σ 's belonging to a same pair are exchanged.

which both are given in the basis $\{|\Psi_1\rangle, |\Psi_2\rangle\}$ (2.30).

When the σ particles are exchanged, there can be non-trivial evolution within the fusion space $V_{\sigma^4}^\psi$. This process is described by a braid operator, or an *R-move*, whose action is illustrated in Figure 2.4(c). Possible braid operators consistent with the *F*-moves can be obtained by solving the so called hexagon equations, which might in general have several solutions. When the σ 's belonging to the same pair are exchanged, the solution corresponding to the Ising anyons is given by

$$R = e^{-i\frac{\pi}{8}} \begin{pmatrix} 1 & 0 \\ 0 & i \end{pmatrix}, \quad (2.32)$$

which describes states corresponding to different fusion channels acquiring different phases. When the σ anyons from different pairs are exchanged or transported around the each, the evolution is more complicated, but it can always be constructed as some sequence of only the *F*-moves, (2.31), and the *R*-moves, (2.32). We will consider such evolutions in Section 3.3 where the characteristic non-Abelian statistics are evaluated from the eigenstates of the model.

To summarize, at a purely mathematical level an anyon model is specified by its particle content $(\{1, \psi, \sigma\})$, the fusion rules (2.28) and the *F*-, (2.31), and *R*-moves, (2.32). Any evolution in a pure topological phase can be understood only in terms of these discrete objects. In the presence of non-Abelian anyons, one expects the fusion space to be manifest as a global ground state degeneracy. The statistics correspond to the evolution of the ground state space under exchanges of the anyons. However, in real physical systems this is rarely the case due to the microscopics of the model. In Chapter 3 we will study to what degree and at what length scales do the characteristics of Ising anyons appear for the vortices in the honeycomb lattice model.

2.5 Numerical diagonalization

To study the physics of the vortices, we need to employ large systems with sparse vortex sectors. As the size of the Hamiltonian (2.14) grows polynomially with the size of the unit cell, analytical solution can be readily obtained only for the limiting cases of vortex-free [62] or full-vortex configuration [71, 86]. In general, the diagonalization of the Hamiltonian (2.14) with the components (2.15)-(2.18) has to be performed numerically. This corresponds still to exact treatment of the model. No numerical approximations are involved except for the discretization of the Brillouin zone.

In general, the diagonalization amounts to finding the eigenvalues $E_{i,\mathbf{p}}$ and eigenvectors $|\psi_{i,\mathbf{p}}^\pm\rangle$ that satisfy

$$H_{\mathbf{p}}|\psi_{i,\mathbf{p}}^\pm\rangle = \pm E_{i,\mathbf{p}}|\psi_{i,\mathbf{p}}^\pm\rangle, \quad (2.33)$$

where $H_{\mathbf{p}}$ is the $2L_xL_y \times 2L_xL_y$ matrix with components h_{bb} and h_{bw} in (2.14). The normalized complex valued vectors $|\psi_{i,\mathbf{p}}^+\rangle$ ($|\psi_{i,\mathbf{p}}^-\rangle$) represent the fermionic one particle modes $b_{i,\mathbf{p}}^\dagger$ ($b_{i,\mathbf{p}}$), whereas the eigenvalues $E_{i,\mathbf{p}}$ coincide with those in (2.19). We call (2.33) the *mode spectrum* of the system.

Apart from the eigenvalues $E_{i,\mathbf{p}}$ that can be obtained directly from the mode spectrum, we will also need the eigenstates corresponding to the ground state, (2.20), and various excited states, (2.21). As the Hamiltonian is diagonal in a basis of free fermions, these can be constructed as Slater determinants of the vectors $|\psi_i^-\rangle$ [87], which represent the anti-commutation properties of the operators b_i . Assuming the Brillouin zone to be discretized using a $n \times n$ mesh, the ground state (2.20) is represented by

$$|\Psi_0\rangle = \mathbf{D} \sum_{\{\mathbf{q}_i\} \in \text{BZ}} \sum_{k,\dots,l=1}^{L_xL_y} \frac{\varepsilon_{k,\dots,l}^{L_xL_y}}{\sqrt{L_xL_y!}} \frac{\varepsilon_{\mathbf{q}_1,\dots,\mathbf{q}_{n^2}}^{n^2}}{\sqrt{n^2!}} |\psi_{k,\mathbf{q}_1}^-\rangle \otimes \dots \otimes |\psi_{l,\mathbf{q}_{n^2}}^-\rangle, \quad (2.34)$$

where $\varepsilon_{i,j,\dots,k}^a$ is the fully anti-symmetric tensors of rank a . Choosing the reference state in (2.20) such that $b_{i,\mathbf{p}}^\dagger|\phi\rangle = 0$, the excited states (2.21) can be similarly

represented by

$$|\Psi_{i,\mathbf{p}_0}\rangle = \mathbf{D} \sum_{\substack{\{\mathbf{q}_i\} \in \text{BZ} \\ \{\mathbf{q}_i\} \neq \mathbf{p}_0}} \sum_{k,\dots,l=1}^{L_x L_y} \frac{\varepsilon_{k,\dots,l}^{L_x L_y}}{\sqrt{(L_x L_y)!}} \frac{\varepsilon_{\mathbf{q}_1,\dots,\mathbf{q}_{n^2-1}}^{n^2-1}}{\sqrt{(n^2-1)!}} |\psi_{k,\mathbf{q}_1}^-\rangle \otimes \dots \otimes |\psi_{l,\mathbf{q}_{n^2-1}}^-\rangle. \quad (2.35)$$

In order to perform the gauge symmetrization \mathbf{D} numerically, one should diagonalize the Hamiltonian $H_{\mathbf{p}}$ for all equivalent gauges u under the local gauge transforms (2.6) and form the corresponding linear combinations manually. For our purposes this turns out not to be necessary, because all quantities of physical interest can be expressed in terms of inner products. Since $\langle \Psi | D_k D_l | \Psi \rangle = \delta_{kl}$, which follows from $\{D_i, \hat{u}_{ij}\} = 0$, only the states in the same gauge can have overlap. Hence, all the inner products can be calculated using a single gauge choice u .

The fact one never needs to explicitly construct the representations of the states is also a crucial technical point. The number of elements in (2.34) and (2.35) grows exponentially with the system size and hence they are in general too large to be stored in a computer.

2.6 Summary

In this first chapter we have reviewed the Kitaev's honeycomb lattice model and its diagonalization through the mapping to free Majorana fermions. At the heart of the exact solvability is the breaking of the full Hilbert space in the sectors labeled by patterns of vortices. Previously only the limiting vortex-free sector had been studied. We generalized the solution of the model to arbitrary vortex sectors where the Hamiltonian has the components (2.15)-(2.18). In general these systems are too complicated to accommodate analytic treatment, but they can be studied numerically without employing any approximation methods.

This generalization of the solution allow us to go beyond the previously studied vortex-free sector. We are now able to consider large systems with only a few vortices and thereby directly study how they influence the spectrum. In particular, our aim is to derive directly the properties of the Ising anyons that should appear as the

Chapter 2. Kitaev's Honeycomb Lattice Model

low-energy vortex excitations in the B -phase. This will be the topic of Chapter 3.

The full-vortex sector has been studied for $K = 0$ in [86]. Our generalized solution allows us to consider also the $K > 0$ case, which turns out to have dramatic consequences for B -phase. It will turn out to support a new chiral Abelian phase, which we will study in detail in Chapter 4.

Chapter 3

Non-Abelian Fusion Rules and Braid Statistics

In this chapter we do “The Dirty Work”, i.e. employ the solutions of sparse vortex sectors to explicitly demonstrate the characteristic non-Abelian fusion rules and braid statistics of the Ising anyons. To this end, we first introduce in Section 3.1 an equivalence between the gauge sectors and the coupling configurations. This enables a theoretical interpolation between vortex sectors and provides a physical protocol for vortex transport. In Section 3.2 we study the spectral evolution as the separation between vortices is varied. The vortices are found to introduce zero modes into the spectrum, which, however, can acquire finite energy when the vortices are brought near each other. We argue that the vortices are interacting and that these interactions reveal the characteristic fusion rules of Ising anyons. By studying the interactions we obtain a characteristic length scale for the pure topological phase. In Section 3.3 we calculate the non-Abelian statistics as a vortex is transported around another. By considering various finite system sizes, we show how the braid statistics can be obtained as a Berry phase corresponding to the evolution of the eigenstates during the transport process.

As we are interested only on the properties of the non-Abelian Ising anyons, we set $|J_x| = |J_y| = |J_z| = 1$ on all links for the purposes of this chapter.

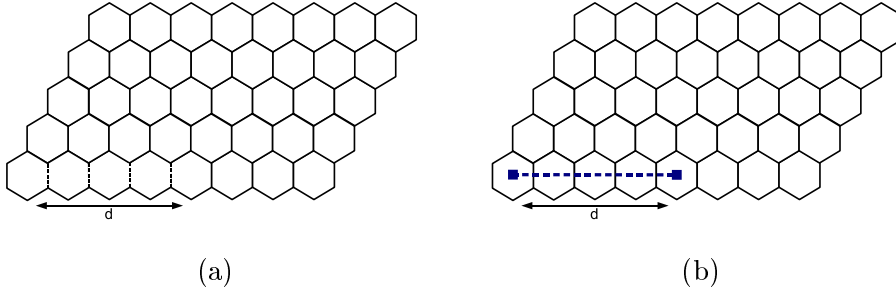


Figure 3.1: The equivalence between (a) the coupling configurations J and (b) vortex configurations w . Fixing the gauge by setting $u_{ij} = 1$ on all links, but tuning the couplings such that $J_{ij} = 1$ on all solid links and $J_{ij} = -1$ on all dashed links is equivalent to creating the vortex configuration shown in (b).

3.1 Gauge/coupling configuration equivalence and vortex transport

As described in the previous chapter, vortex configurations $w = \{w_p\}$ are created through (2.9) by fixing the gauge configuration $u = \{u_{ij}\}$. In order to manipulate w , one should thus manipulate u locally. Even though u is not by itself gauge invariant and thus not a physical parameter of the model, we can effectively manipulate it through the coupling configurations $J = \{J_{ij}\}$. As can be seen from (2.8), u_{ij} appears always uniquely paired with a local coupling J_{ij} . Therefore, as $u_{ij} = -1$ with $J_{ij} > 0$ is equivalent to $u_{ij} = 1$ with $J_{ij} < 0$, we can regard the value of the gauge field just as the sign of the couplings,

$$u_{ij} = \text{sign}(J_{ij}), \quad \Rightarrow \quad J_{ij} \rightarrow -J_{ij} \Leftrightarrow u_{ij} \rightarrow -u_{ij}. \quad (3.1)$$

Strictly speaking one should also imprint these signs on the local values of K . However, when the term approximates an external magnetic field, i.e. when $K \ll J_{ij}$, controlling the signs of J_{ij} is sufficient. Therefore, assuming that the system has been prepared in the ground state belonging to the vortex-free sector [88], we can treat the gauge sectors, and thereby the vortex sectors, just as some non-homogenous coupling configurations J with varying overall signs. From now on, we adopt this dual

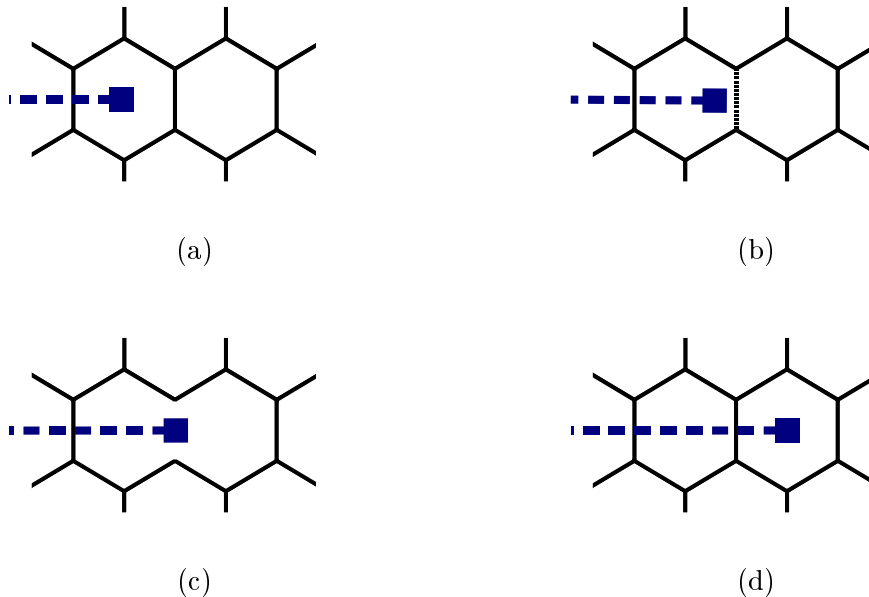


Figure 3.2: A protocol for vortex transport in s steps through local coupling manipulation. (a) Initially the coupling configuration is chosen such that $J_{ij} = -1$ on the links crossed by the dashed line, while $J_{ij} = 1$ on all other links. This corresponds to a vortex on the left plaquette. (b) Consider changing the value coupling on the link in the middle from $J_{ij} = 1$ to $J_{ij} = -1$ in S steps of size $\frac{2}{S}$. At step s its value is $J_{ij}^s = 1 - \frac{2s}{S}$, which we interpret as the vortex occupying a location away from the plaquette center. (c) When $J_{ij}^s = 0$, the Wilson loop operator is defined only on the composite plaquette. As the vortex occupies both plaquettes simultaneously, we interpret it as being right in the middle. (d) Finally, as $J_{ij}^s \rightarrow -1$, the vortex moves smoothly to the plaquette on the right.

perspective, which allows to relate the manipulation of vortices to the manipulation of physically tunable parameters. We will still be referring to gauge and vortex sectors, but these terms should be understood as referring to coupling configurations that give rise to them.

To study the physics of the vortices, we define a sparse vortex configuration by choosing a large (L_x, L_y) -unit cell and consider the system in the vortex-free sector by setting $u_{ij} = 1$ on all links. Consider then tuning the coupling configuration such that $J_z = -1$ on the d first z -links of the first row of the unit cell as shown in Figure 3.1(a). Due to the equivalence (3.1), this amounts to creating two vortices separated linearly by d links as shown in Figure 3.1(b). By varying d we can study the spectral

evolution as a function of the vortex separation up to distances of $d = L_x/2$.

Instead of just placing vortices on plaquettes, we can imagine carrying out the vortex transport "continuously" as follows. If the sign of the coupling J_{ij} at the link $d+1$ is reversed in S steps of size $\frac{2}{S}$ such that at step s the value is $J_{ij} = 1 - \frac{2s}{S}$, the process will result in vortex transport as illustrated in Figures 3.2(a)-(d). We denote the continuous vortex separation by $d_s = d + \frac{s}{S}$, where s denotes the intermediate vortex position and $d_S = d+1$. Intuitively we can then regard the intermediate steps for which $|J_{ij}| < 1$ as the vortex occupying some intermediate position in between the plaquettes. Although there is no a priori reason for this interpretation, we will show below that the spectrum does indeed evolve continuously under such transport process. Moreover, if this protocol is carried out on a link between empty plaquettes or plaquettes with two vortices, the resulting process corresponds to creation and annihilation of vortices, respectively. This means that we can study also the spectral evolution when interpolating between vortex sectors of varying vortex occupation.

We note that it is also experimentally motivated to treat the vortex sectors and the coupling configurations on equal footing. Given sufficient site addressability, the local control of the couplings J_{ij} is also how one could perform vortex creation and transport in the proposed optical lattice implementations of the honeycomb lattice model [51, 53].

3.2 Fusion rules from the spectral evolution

In this section we study how the presence of vortices modifies the spectrum and how it depends on the vortex separation d_s . Ideally we would like to use as large a unit cell as possible in order to isolate the vortices from each other. It turns out that unit cells of around 400 plaquettes (800 spins), such as a (20, 20)-unit cell, are sufficient to extract the asymptotic behavior when $d_s \rightarrow \infty$. The resulting Hamiltonians are sparse 800×800 matrices, which can be diagonalized numerically using Matlab on a tabletop computer. Employing (2.20) and (2.21), we can then calculate the ground state E_{0,d_s}^{nv} and various excited state energies Δ_{i,d_s}^{nv} corresponding to the

vortex separation d_s at an n -vortex sector.

3.2.1 Zero modes and vortex interactions

Figures 3.3(a)-(c) show the energy behavior of the three lowest lying modes in the absence of vortices, and in the presence of two and four well separated vortices, respectively. The first shows the already known fact that in the absence of vortices the spectrum is gapped with all Δ_{i,d_s}^{0v} being nearly degenerate and non-zero. On the other hand, when a pair of vortices is introduced, Figure 3.3(b) shows that Δ_{1,d_s}^{2v} becomes vortex separation dependent. The energy of the mode oscillates with separation and converges to zero as $d_s \rightarrow \infty$, whereas both Δ_{2,d_s}^{2v} and Δ_{3,d_s}^{2v} remain insensitive to it. From Figure 3.3(c) we see that when a second vortex pair is introduced away from the first one, both Δ_{1,d_s}^{4v} and Δ_{2,d_s}^{4v} acquire the oscillatory d_s dependence, while Δ_{3,d_s}^{4v} remains insensitive. By considering a system of n isolated vortex pairs, we find that the n lowest lying modes acquire this behavior.

Due to the large d_s behavior, we call these modes *zero modes*. Since they only appear in the presence of vortices and their energy decays with vortex separation, we interpret the vortices having strong short-range interactions. In the presence of $2n$ vortices there are n zero modes in the spectrum, which means that the diagonalized Hamiltonian (2.19) takes the form

$$H = \int_{\text{BZ}} d^2p \left[\sum_{i=n+1}^{L_x L_y} E_{i,\mathbf{p}} b_{i,\mathbf{p}}^\dagger b_{i,\mathbf{p}} + \sum_{i=1}^n \epsilon_{i,\mathbf{p}}^{d_s} z_{i,\mathbf{p}}^\dagger z_{i,\mathbf{p}} - \left(\sum_{i=n+1}^{L_x L_y} \frac{E_{i,\mathbf{p}}}{2} + \sum_{i=1}^n \frac{\epsilon_{i,\mathbf{p}}^{d_s}}{2} \right) \right]. \quad (3.2)$$

We have renamed the n smallest eigenvalues and the corresponding modes as $\epsilon_{i,\mathbf{p}}^{d_s}$ and $z_{i,\mathbf{p}}$, respectively. Figures 3.3(b) and 3.3(c) suggest that when the vortex pairs are far from each other, $\epsilon_{i,\mathbf{p}}^{d_s}$ take the form

$$\epsilon_{n,\mathbf{p}_0}^{d_s} \sim \Delta_{n+1}^{2nv} \cos(\omega d_s) e^{-\frac{d_s}{\xi}}, \quad (3.3)$$

where $\omega > 0$ and $\xi > 0$ depend on the couplings and parametrize the frequency of the oscillations and the convergence of the energy, respectively.

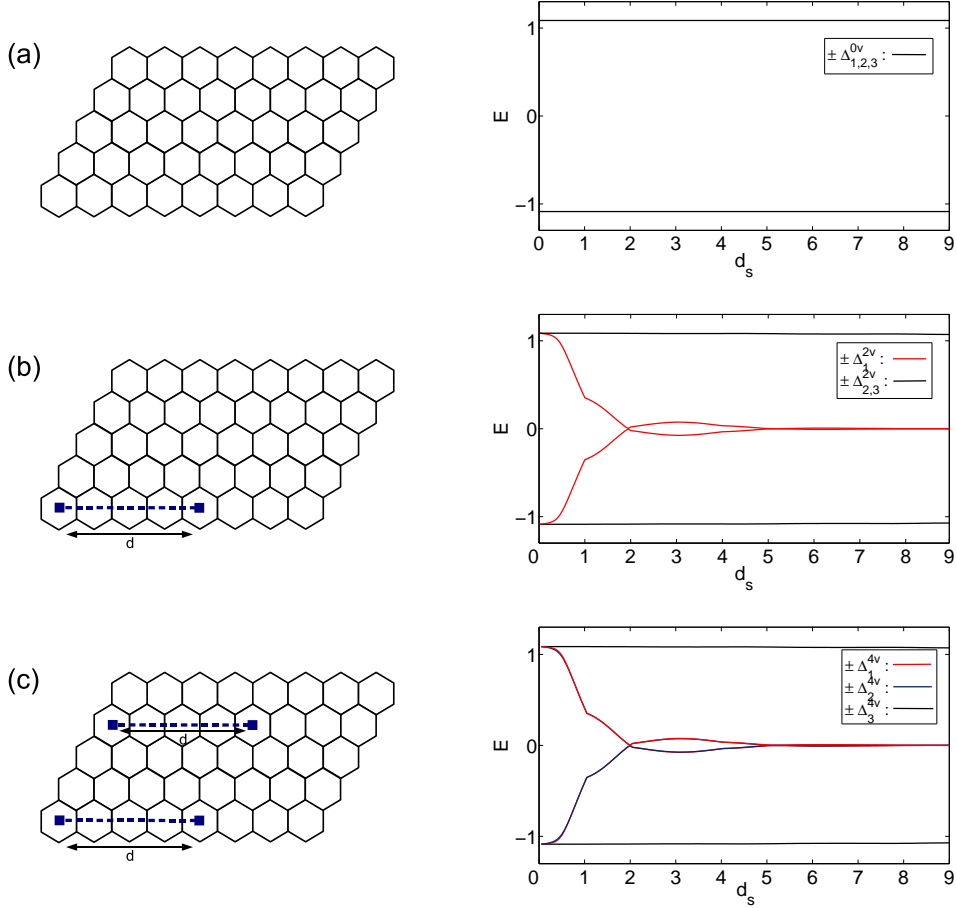


Figure 3.3: The mode spectrum, (2.33), for the three lowest lying modes with energies Δ_{1,d_s} , Δ_{2,d_s} and Δ_{3,d_s} . (a) In the absence of vortices all the modes are gapped and there is trivially no d_s dependence. (b) In the presence of a single vortex pair Δ_{1,d_s}^{2v} oscillates with separation and converges to zero energy $d_s \rightarrow \infty$. Δ_{2,d_s}^{2v} and Δ_{3,d_s}^{2v} are independent of d_s . (c) In the presence of two vortex pairs (nine rows apart, picture not on scale), both Δ_{1,d_s}^{4v} and Δ_{2,d_s}^{4v} acquire this identical d_s dependence (the plots overlap) while Δ_{3,d_s}^{4v} is still insensitive. The plots are produced for $K = 0.1$ and $S = 20$ using a $(20, 20)$ -unit cell.

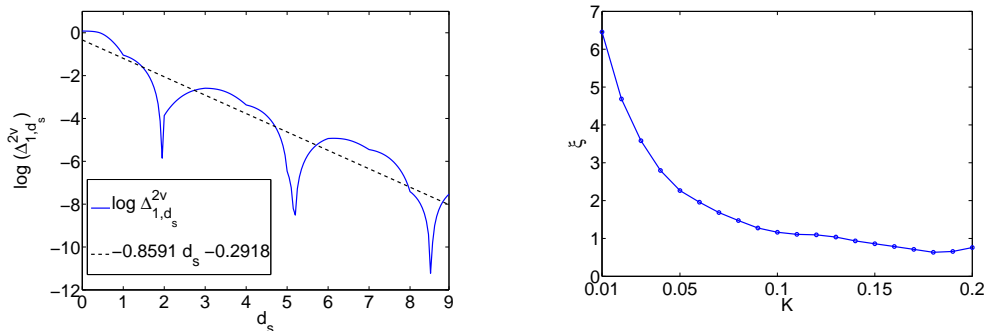


Figure 3.4: A study of the 2-vortex ground state degeneracy as functions of the vortex separation d_s and magnetic field K using a $(20, 20)$ -unit cell. (a) A plot of $\log(\Delta_{2,d_s}^{2v})$ for $K = 0.1$. A linear fit gives $\xi \approx 1.2$ (in units of d_s) for the characteristic length scale. (b) ξ a function of K showing $\xi \approx \frac{0.12}{K}$ behavior.

In particular, we are interested in the magnitude of ξ as it gives the characteristic length scale of the interactions that are not part of the pure topological theory. In Figure 3.4(a) we plot $\ln(\Delta_{1,d_s}^{2v})$ when $K = 0.1$ for the 2-vortex system illustrated in Figure (3.3)(b). The linear fit with negative slope confirms the exponential convergence of the zero mode energy with vortex separation, and distance between successive dips gives the half of the wavelength of the oscillations. By performing similar linear fits for $\ln(\Delta_{1,d_s}^{2v})$ for a range of K 's, we obtain Figure 3.4(b), which shows $\xi \sim K^{-1}$ behavior with $\xi \approx 1$ when $K = 0.12$. For a particular value of K , we expect the system to be well described by the Ising anyon theory when the vortex separation satisfies $d_s \gg \xi$.

The oscillatory behavior of the interactions, (3.3), does not play a significant role in the present discussion and thus we leave its systematic study for future work. To summarize it briefly, our numerical studies have shown that the frequency ω depends primarily on the couplings J , such that the frequency is higher the closer one is to the phase boundaries (2.24). In Chapter 4 we will connect at a heuristic level these interaction oscillations to the phase space behavior of the full-vortex sector.

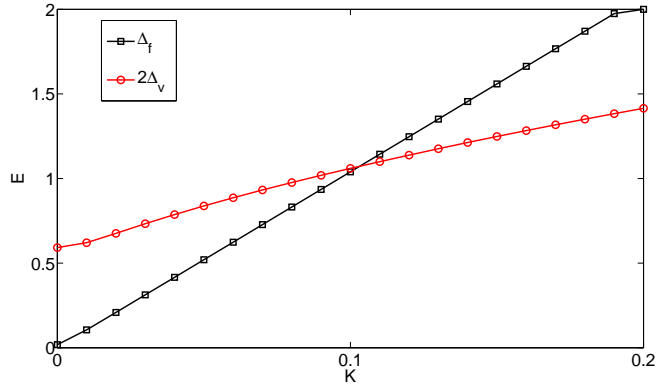


Figure 3.5: The behavior of the fermion gap, Δ_f , and the vortex gap, $2\Delta_v$, in a 2-vortex system as functions of K . The scaling is nearly linear in both cases.

3.2.2 The low-energy spectrum

To outline the full low-energy spectrum of the model, we consider the energy gaps to non-zero mode states and the relative ground state energies of different vortex sectors. These are also of interest, because they describe the stability of the non-Abelian phase against thermal fluctuations.

Figures (3.3)(a)-(c) show that $\Delta_{n+1}^{2nv} = \Delta_1^{0v}$, i.e. that the energy of the first non-zero mode coincides always with the fermion gap of the the vortex-free sector. This suggests that in general the fermion gap for an $2n$ -vortex system should be defined as

$$\Delta_f \equiv \Delta_{n+1}^{2nv} = \min_{\mathbf{p}} E_{n+1, \mathbf{p}}. \quad (3.4)$$

This implies that the modes $b_{i, \mathbf{p}}$ in (3.2) still describe free fermions, and reinforces the notion that the modes $z_{i, \mathbf{p}}$, although being fermionic operators, describe some new degrees of freedom due to the presence of vortices. We will discuss their interpretation in a moment.

We can also define asymptotically the *vortex mass* as the relative ground state energy of the vortex-free and 2-vortex sectors,

$$2\Delta_v = \lim_{d_s \rightarrow \infty} (E_{0, d_s}^{2v} - E_0^{0v}). \quad (3.5)$$

It describes the amount of energy needed to create a pair of vortices out of vacuum and take them far enough for the interaction to be negligible. We plot in Figure 3.5 the behavior of both (3.4) and (3.5), which shows that both increase roughly linearly with K . The fermion gap vanishes for $K = 0$, the vortices have mass also in the gapless phase.

We can combine the mode spectra and the vortex gaps for the 0-, 2-vortex sectors to outline the full low-energy spectrum of the Hamiltonian (3.2). Figure 3.6(a) shows the evolution of the lowest lying states in the 2-vortex sector relative to the ground state energy E_0^{0v} of the vortex-free sector. At large d_s the states $|\Psi_0^{2v}\rangle$ and $z_1^\dagger|\Psi_0^{2v}\rangle$ differing by the occupation of the zero mode are degenerate with energies $2\Delta_v$ above the vortex-free ground state. As the vortices are brought closer, the degeneracy is lifted due to the mode z_1^\dagger acquiring energy, i.e. $\epsilon_1^{d_s}$ becoming non-zero as shown in Figure 3.3(b). As $d_s \rightarrow 0$, the vortices are brought to the same plaquette which corresponds to fusing them. We observe that the energy corresponding to $|\Psi_0^{2v}\rangle$ evolves to the energy of the ground state $|\Psi_0\rangle$ of the vortex-free sector. On the other hand, $z_1^\dagger|\Psi_0^{2v}\rangle$ evolves to $b_{1,\mathbf{p}_0}^\dagger|\Psi_0\rangle$, the first excited free fermion state in the vortex-free sector.

Before proceeding to connect this spectral evolution with the fusion rules, let us comment on the hopping of the energies in Figure 3.6(a). It is due to the employed transport protocol. The minima always occur for integer values of d_s , i.e. for configurations uniform in amplitude, $|J_{ij}| = 1$, whereas the maxima occur at $d_{S/2}$, i.e. when the transported vortex occupies a composite plaquette twice the size of a regular plaquette (see Figure 3.2(c)). We note that $E_0^{2v,d_{S/2}} - E_0^{2v,d_S} \approx \Delta_v$, which means an energy of Δ_v is required to move a vortex to an adjacent plaquette. This suggests that we can think the vortex mass Δ_v equivalently as the depth of a local potential that confines the vortices at the plaquettes. The energy gaps Δ_f and Δ_v give a measure of the stability of the vortex sectors against thermal fluctuations at temperature T . When $T \ll \Delta_f, \Delta_v$, the creation and propagation of both fermions and vortex excitations is exponentially suppressed.

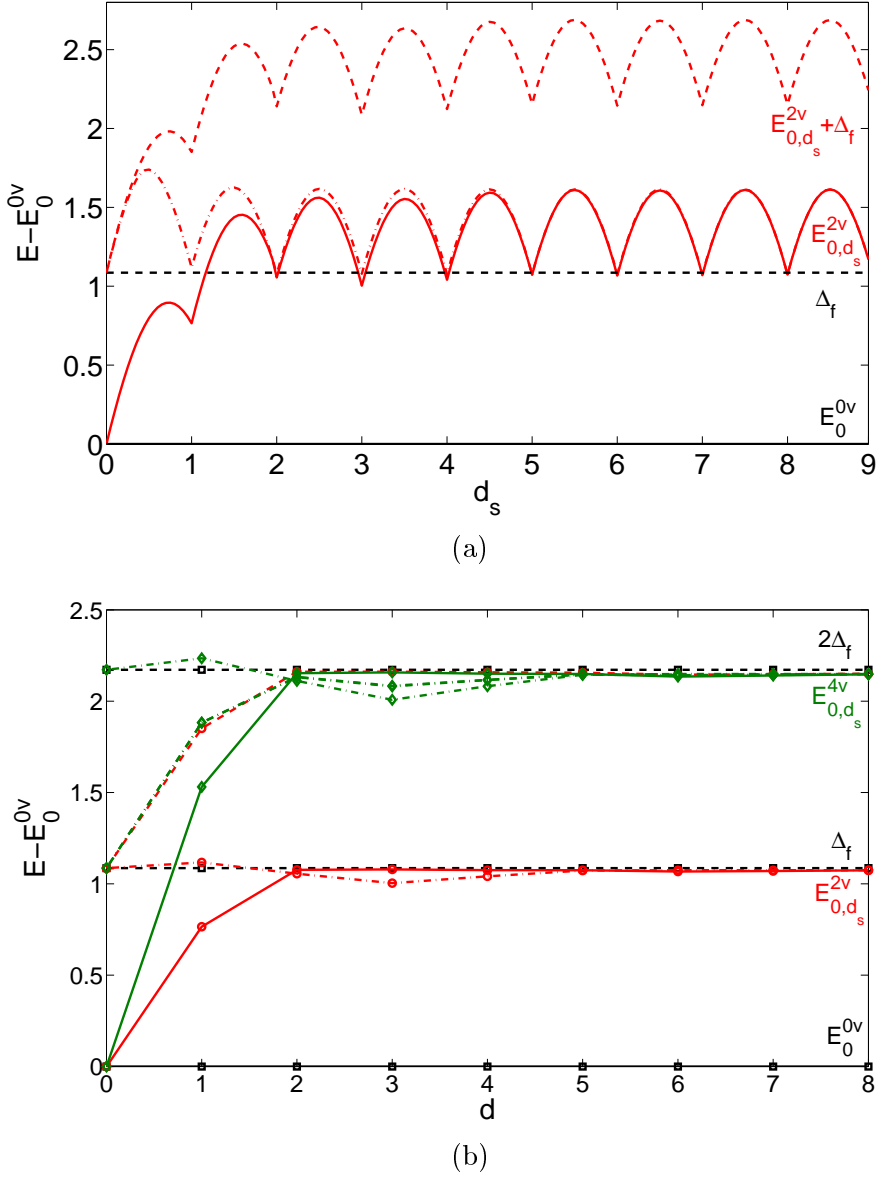


Figure 3.6: The low-energy spectrum of the B -phase when $|J_\alpha| = 1$ and $K = 0.1$ as a function of vortex separation. All the energies in the 2-vortex (red lines) and 4-vortex (green lines) sectors are with respect to the ground state energy of the vortex-free sector (black lines). The solid lines are the total ground state energies, the dash-dotted ones are states with occupied zero modes and the dashed lines correspond to lowest lying free fermion states over the respective vortex sectors. (a) The 2-vortex low-energy spectrum as a function of d_s . (b) The low-energy spectrum including both 2- and 4-vortex sectors for the integer values of d_s . The near degeneracy of the 2-vortex ground state with the first excited state of the vortex-free sector, i.e. $\Delta_f \approx 2\Delta_v$, is accidental due to the choice of $K = 0.1$ as shown in Figure 3.5.

3.2.3 Zero modes as fusion degrees of freedom

The distinct behavior of the 2-vortex states $|\Psi_0^{2v}\rangle$ and $z_1^\dagger|\Psi_0^{2v}\rangle$ in Figure 3.6(a) as $d_s \rightarrow 0$ suggests that the occupation of the zero mode corresponds to the fusion channel of the vortices. Let us identify the σ particles of the Ising anyon model with the vortices, and the ψ 's with free fermion modes b_i^\dagger . Then in accordance with the fusion rules (2.28), an occupied zero mode means that the σ 's will fuse to a ψ , whereas unoccupied mode implies that the fusion will give the vacuum 1.

This is further confirmed in Figure 3.6(b), where we plot the low-energy spectrum including the 4-vortex sector when the separation of the two vortex pairs is varied pair-wise (see Figure 3.3(c)). The plot is only for the integer values of d_s to omit the irrelevant hopping behavior. The 4-vortex sector has the physically non-trivial two-dimensional fusion spaces $V_{\sigma^4}^1$ and $V_{\sigma^4}^\psi$, (2.29). The spectral evolution shows that when the vortices are fused, there are two nearly degenerate states (either z_1 or z_2 occupied) that become the first excited state in the vortex-free sector. The states with neither or both zero modes occupied become the ground state or the two fermion state, respectively. Therefore we can identify these four states with the fusion space basis states as:

$$\begin{aligned} |\Psi_0^{2v}\rangle \in V_{\sigma^4}^1 &: (\sigma \times \sigma)_1 \times (\sigma \times \sigma)_2 \rightarrow 1 \times 1 = 1, \\ z_1^\dagger z_2^\dagger |\Psi_0^{2v}\rangle \in V_{\sigma^4}^1 &: (\sigma \times \sigma)_1 \times (\sigma \times \sigma)_2 \rightarrow \psi \times \psi = 1, \end{aligned} \quad (3.6)$$

and

$$\begin{aligned} z_1^\dagger |\Psi_0^{2v}\rangle \in V_{\sigma^4}^\psi &: (\sigma \times \sigma)_1 \times (\sigma \times \sigma)_2 \rightarrow \psi \times 1 = \psi, \\ z_2^\dagger |\Psi_0^{2v}\rangle \in V_{\sigma^4}^\psi &: (\sigma \times \sigma)_1 \times (\sigma \times \sigma)_2 \rightarrow 1 \times \psi = \psi. \end{aligned} \quad (3.7)$$

The appearance of the fusion degrees of freedom as zero modes can be understood in the context of p -wave superconductors to which the honeycomb lattice model can be mapped [89]. There one can explicitly show that vortices bind unpaired massless Majorana fermions γ_i [83, 90], that are responsible for the non-Abelian behavior [81, 91, 92]. As $\gamma_i^\dagger = \gamma_i$ by definition, one can not define a local degree of freedom for an isolated Majorana mode. However, two such modes localized at

i and $i + 1$, regardless of how far separated they are spatially, can be combined to a complex fermion mode $z_i = (\gamma_i + i\gamma_{i+1})/2$. The occupation of this mode is a non-local property of a pair and it corresponds to the two possible fusion outcomes of the anyonic vortices. When the vortices are nearby, tunneling processes between the vortex cores lead to an oscillating interaction that lifts the degeneracy of the fusion channels [93]. In the honeycomb lattice model we do not observe directly the localized Majorana modes, but the oscillating zero modes, (3.3), are exactly as predicted by this dual picture.

3.2.4 Discussion

By studying the spectral evolution as a function of vortex separation, we have demonstrated that the presence of vortices in the B -phase introduces zero modes and that these can be identified with the fusion degrees of freedom of the Ising anyons. The anyonic vortices are shown to exhibit exponentially decaying interactions whose magnitude oscillates with the vortex separation. When the vortices are nearby, the vacuum channel is always energetically favoured. We found that the range of these interactions is controlled by the K dependent parameter ξ . For vortex separations $d_s \gg \xi$, the states corresponding to the fusion channels are degenerate, and we anticipate the low-energy spectrum to be well approximated by the pure topological theory.

To identify the fusion rules from the zero modes, it was sufficient to consider only the very short and the very long-range behavior and neglect the oscillatory term in (3.3). Although these limiting behaviors are not altered by its inclusion, our further numerical studies have shown that the oscillations depend strongly on the couplings J_α . As one approaches the phase boundaries (2.24), their frequency increases while the period decreases. As long as only very few vortices are present, the physics of the non-Abelian phase is unaffected by them. However, when the vortex density is increased, i.e. when many vortices interact simultaneously with each other, these oscillations quickly smear out the vacuum channel as the favoured fusion channel.

This turns out to have dramatic consequences on the collective states of interacting anyons that can give rise to completely new phases. This effect will be discussed in more detail in Chapter 4.

Apart from the interactions, another interesting microscopic detail of the model is the dependence of the vortex mass Δ_v on the local coupling configurations. As showed in Figure 3.6(a), it seems to be directly proportional to the number of plaquettes the vortex occupies. This suggests that the ground state admits partial stabilizer representation in terms of the plaquette operators, which agrees with the form derived in [68]. The vortex mass can also be interpreted in terms p -wave superconductor picture. Since Δ_v gives the amount of energy required to move a vortex to an adjacent plaquette, it can be equivalently viewed as the height of the potential barrier confining the Majorana modes to the vortex cores. This interpretation agrees with a larger K suppressing the interactions (3.3). As a larger K increases also the potential barrier, it suppresses the tunnelings which can be understood as giving rise to them [93].

3.3 Non-Abelian statistics as a Berry phase

In this section we explicitly calculate the non-Abelian statistics of the σ anyons. We transport the vortices around each other using the protocol in Figure 3.2 and evaluate the corresponding evolution in the fusion space as a Berry phase. By considering various finite systems, we are able to identify parameter ranges where it corresponds to the statistics of Ising anyons with high fidelity. Together with the fusion rules derived above from the spectral evolution, this conclusively demonstrates the non-Abelian character of Kitaev's honeycomb lattice model.

3.3.1 Statistics and holonomies

In general, when z_1 and z_2 are the coordinates of some point-like particles, their statistics is given by the transformation of the collective wave function under their permutation,

$$\psi(z_1, z_2) = U\psi(z_2, z_1), \quad (3.8)$$

where U is the characteristic statistical phase or matrix. Due to topological arguments [3], in three or more spatial dimensions U must satisfy $U^2 = 1$. The only solutions are $U = \pm 1$, which correspond to bosons and fermions. On the other hand, in two spatial dimensions one can have $U^2 \neq 1$, which can give rise to anyonic statistics. In particular, if $U = e^{i\theta}$ for some phase θ , the statistics is called Abelian, and the particles are *Abelian anyons*. If U is a unitary matrix acting in a degenerate state space, the particles are called *non-Abelian anyons*.

In real physical systems the permutation of the coordinates corresponds to adiabatically transporting the particles such that their positions are swapped [94]. Often single exchanges can not be defined unambiguously. Instead one needs to consider evolutions where a particle winds around another along a suitable chosen closed path C . Regardless of the local details of the path, the process then is topologically equivalent to two successive exchanges. As the evolution of the system is cyclic, the wave function can acquire a non-trivial Berry phase Γ_C [95], or more generally,

a *holonomy* [96]. In the presence of degenerate states, Γ_C can be a matrix implementing a rotation in the degenerate subspace [97]. In general, the evolution due to cyclic adiabatic transport can be split as $\Gamma_C = \Gamma_C^g \Gamma_C^t$ into two contributions. Here Γ_C^g describes the geometric contribution, that depends on the local geometry of the path. On the other hand, Γ_C^t depends only on the path's topology, i.e. only on the evolution in the configuration space, which on a simply connected two-dimensional manifold is due the particles encircling each other [98]. Therefore, if the path C can be chosen such that $\Gamma_C^g = \mathbb{1}$, the holonomy coincides with the mutual statistics of the particles, i.e. $\Gamma_C = U^2$. For bosons and fermions this is always trivial, with any non-trivial evolution being a sign of anyonic statistics.

One can satisfy $\Gamma_C = \Gamma_C^t$ if one demands that the evolution C is not only cyclic in all parameters employed, but that it is cyclic such that it spans no area in position space [62]. In the honeycomb lattice setting, a suitable path is illustrated in Figure 3.7(a), where the dashed lines indicate the two oriented parts C_1 and C_2 of the total path C . The evolution along this path is cyclic in the space of coupling configurations J where the transport is implemented. Neither does it span any spatial area as C always involves both C_i and C_i^{-1} . Figures 3.7(b) and 3.7(c) illustrate that different ordering of the parts C_1 and C_2 give rise to topologically distinct evolutions. The evolution C_l links the world lines of the particles from different pairs and thus should correspond to the statistics of exchanging the particles twice. On the other hand, C_o spans exactly the same path in the position space, but topologically it corresponds to trivial evolution in the configuration space.

If one regards the vortices connected by a solid lines being paired, the evolution C_l in Figure 3.7(b) corresponds to exchanging twice the vortices belonging to different pairs. Restricting to considering a global ψ sector, i.e. considering the evolution in $V_{\sigma^4}^\psi$, and adopting the pair-wise fusion basis (3.7), we can predict the outcome of such an evolution from the abstract theory of Ising anyons. In Figure 3.8(a) we illustrate the required sequence of F -, (2.31), and R -moves, (2.32). One must first use an F to move to a basis where the braided anyons are fused, then apply R^2

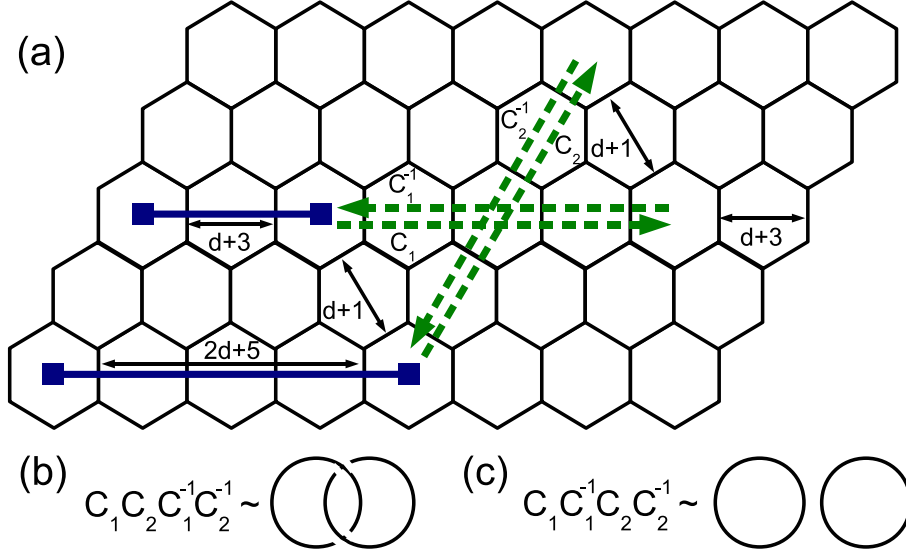
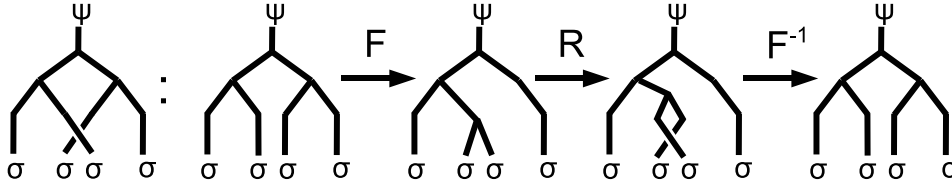


Figure 3.7: (a) The honeycomb lattice containing two vortex pairs. The parameter d controls the minimal vortex separation in units of links. It is related to the unit cell dimensions through $L_x = 4(d+1)$ and $L_y = 2d+1$ (picture not on scale). The four dashed arrows C_1, C_1^{-1}, C_2 and C_2^{-1} are the oriented parts of the path C along which the vortices are transported. (b) $C_l = C_1 C_2 C_1^{-1} C_2^{-1}$ is topologically equivalent to a link. (c) $C_o = C_1 C_1^{-1} C_2 C_2^{-1}$ is topologically equivalent to two unlinked loops.

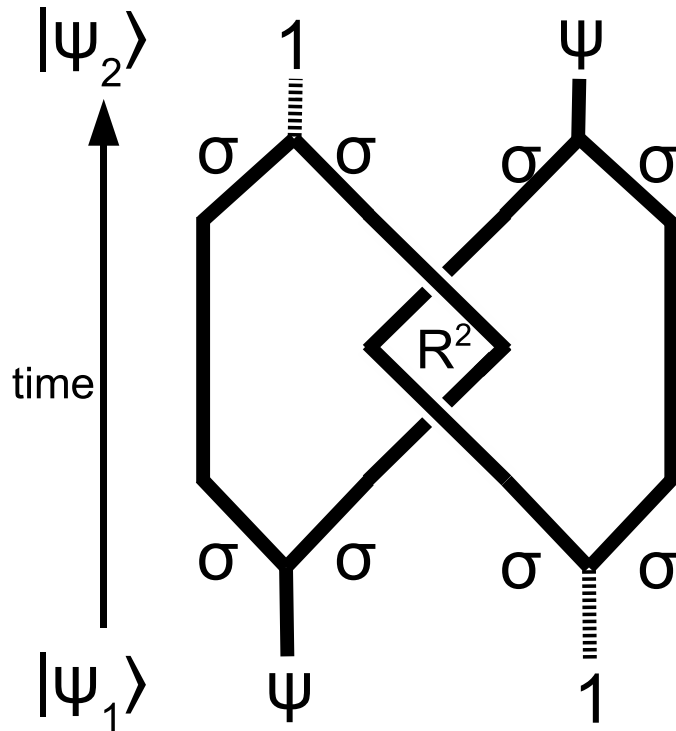
to perform the braiding, and subsequently use $F^{-1} = F$ to return to the original basis. In general, the process where a particle winds around another is known as a *monodromy*. For this particular case it is given by

$$\bar{R}^2 = FR^2F = e^{-\frac{\pi}{4}i} \begin{pmatrix} 0 & 1 \\ 1 & 0 \end{pmatrix}. \quad (3.9)$$

The overall phase is a characteristic to the Ising anyons, whereas the off-diagonality is a characteristic of non-Abelian anyons in general. As the basis on which \bar{R}^2 acts is associated with the information about which pair fuses to a ψ , the monodromy provides an intuitive illustration of the non-locality of the fusion degrees of freedom. This process is illustrated in Figure 3.8(b). Regardless of how far the σ particles are spatially, their monodromy, (3.9), will result in a process which can be viewed as a ψ particle being teleported between the two pairs.



(a)



(b)

Figure 3.8: (a) To find the evolution corresponding to braiding anyons from different pairs, one must first use the F -moves to rotate to a basis where the anyons to be braided are fused, i.e. where the action of R is defined (see Figure 2.4(c)). After applying R to implement the exchange, one can return to the original basis with F^{-1} to find the corresponding evolution. (b) When the σ 's from different pairs are exchanged twice, the evolution in $V_{\sigma^4}^\psi$ with basis $\{|\Psi_1\rangle, |\Psi_2\rangle\}$ is proportional to a σ^x rotation, (3.9). This process can be thought of as a ψ being teleported between the two pairs.

3.3.2 Discrete holonomies

To evaluate the accumulated wave function evolution corresponding to the monodromy, we need to employ the transport protocol of Figure 3.2 to simulate the vortex transport using discrete steps. To this end we derive first a convenient discrete expression for the holonomy.

Consider a Hamiltonian $H(\lambda)$ with n -fold degeneracy $\{|\Psi_\alpha(\lambda)\rangle|\alpha = 1, \dots, n\}$ that depends on some parameters λ . When we adiabatically vary λ along a closed path C , the evolution of the degenerate subspace is given by the holonomy [97]

$$\Gamma_C = P \exp \oint_C A^\mu(\lambda) d\lambda_\mu, \quad [A^\mu(\lambda)]_{\alpha\beta} = \langle \Psi_\alpha(\lambda) | \frac{d}{d\lambda^\mu} | \Psi_\beta(\lambda) \rangle \quad (3.10)$$

where P denotes path ordering in λ , and $A^\mu(\lambda)$ is the connection in the space of states $|\Psi_\alpha(\lambda)\rangle$ above the control parameter space. Let us discretize the path C into T infinitesimal intervals of length $\delta\lambda$ with λ_t denoting the control parameter value at step t . We can write

$$\Gamma_C = \lim_{T \rightarrow \infty} P \prod_{t=1}^T [\mathbb{1} + \delta\lambda_\mu A^\mu(\lambda_t)]. \quad (3.11)$$

Discretizing the derivative in $A^\mu(\lambda)$, it follows that

$$[A^\mu(\lambda_t)]_{\alpha\beta} = \frac{1}{\delta\lambda_\mu} \langle \Psi_\alpha(\lambda_{\mu,t}) | \Psi_\beta(\lambda_{\mu,t+1}) \rangle - \delta_{\alpha\beta}. \quad (3.12)$$

Inserting this into the discretized holonomy (3.11), and grouping the states at step t together, we obtain

$$\Gamma_C = \lim_{T \rightarrow \infty} P \prod_{t=1}^T \left(\sum_{\alpha=1}^n |\Psi_\alpha(\lambda_t)\rangle \langle \Psi_\alpha(\lambda_t)| \right). \quad (3.13)$$

This convenient form means that in the limit $\delta\lambda \rightarrow 0$ the holonomy can be calculated as an ordered product of projectors onto the ground state space at each step t along the path C .

Resolving the gauge freedom

In general, the non-Abelian holonomy (3.10) is not gauge invariant. This is due to the freedom to rotate the basis vectors at every step t by $|\Psi_\alpha(\lambda_t)\rangle \rightarrow g_t|\Psi_\alpha(\lambda_t)\rangle$ by some $n \times n$ unitary matrix g_t . This transforms the connection A^μ at step t by

$$g_t : \quad A^\mu(\lambda_t) \rightarrow g_t^\dagger A^\mu(\lambda_t) g_t + g_t^\dagger \partial_\mu g_t. \quad (3.14)$$

It follows that the holonomy transforms as

$$g : \quad \Gamma_C \rightarrow g \Gamma_C g^\dagger, \quad (3.15)$$

where $g \equiv g_1 = g_T$, which is guaranteed by choosing explicitly $|\Psi_\alpha(\lambda_1)\rangle = |\Psi_\alpha(\lambda_T)\rangle$ [98]. Because $\text{Tr}(\Gamma_C) = \text{Tr}(g^\dagger \Gamma_C g)$, only the trace of a non-Abelian holonomy is gauge invariant, and thus resolving the full form of the matrix Γ_C is in general not unambiguous.

In an actual physical system like ours, the states $|\Psi_\alpha\rangle$ are never perfectly degenerate. This means that instead of g being a rotation in a degenerate space, it only assigns independent phases to each state, i.e. $g = \text{diag}(e^{i\phi_1}, \dots, e^{i\phi_n})$. The diagonal elements of Γ_C will be naturally gauge invariant, with the off-diagonal elements acquiring some correlated phases. To be precise, when Γ_C is a 2×2 unitary, the gauge transform acts as

$$g : \begin{cases} [\Gamma_C]_{12} & \rightarrow [\Gamma_C]_{12} e^{i(\phi_1 - \phi_2)} \\ [\Gamma_C]_{21} & \rightarrow [\Gamma_C]_{21} e^{-i(\phi_1 - \phi_2)} \end{cases} \quad (3.16)$$

When Γ_C is unitary, and predominantly off-diagonal, i.e. $||[\Gamma_C]_{12}| = |[\Gamma_C]_{21}| \approx 1$, we can remove the phases by replacing the off-diagonal elements of Γ_C with

$$[\Gamma_C]_{12}, [\Gamma_C]_{21} \rightarrow \pm \sqrt{[\Gamma_C]_{12} [\Gamma_C]_{21}}. \quad (3.17)$$

The residual overall sign freedom is fixed by continuity requirements.

3.3.3 Holonomy due to vortex transport

To reduce the complexity of the calculations, we consider a finite system of $2L_xL_y$ spins on a torus. This is equivalent to a (L_x, L_y) -unit cell with elements (2.15)-(2.18) when one sets $\mathbf{p} = 0$ everywhere. The initial four-vortex configuration is shown in 2.1(a), where the d parametrizes the minimal vortex separation at all times during the transport process.

As shown in the previous section, for large d this system has altogether four degenerate ground states arising from a pair of zero modes. Due to the conservation of the global fermionic parity, the degenerate states split into two orthogonal subspaces $V_{\sigma_4}^1$ and $V_{\sigma_4}^\psi$ spanned by the pair-wise fusion channel states (3.6) and (3.7), respectively. For technical reasons we consider here the latter case, where the numerical representations, (2.35), of the states $|\Psi_1\rangle \equiv z_1^\dagger |\Psi_0^{2v}\rangle$ and $|\Psi_2\rangle \equiv z_2^\dagger |\Psi_0^{2v}\rangle$ are given by

$$|\Psi_\alpha\rangle = \sum_{\substack{\{k,\dots,l=1\} \\ k,\dots,l \neq \alpha}}^{L_xL_y-1} \frac{\varepsilon_{k,\dots,l}}{\sqrt{(L_xL_y-1)!}} |\psi_k^-\rangle \otimes \cdots \otimes |\psi_l^-\rangle. \quad (3.18)$$

The continuous transport of the vortices is simulated by tuning the local couplings J in T_S steps along the path C in an ordered manner. Let us denote by $|\Psi_\alpha^{t_s}\rangle$ the eigenvectors at step t_s , $1 \leq t_s \leq T_S$, where t indexes a particular plaquette along the path and s the intermediate locations as required for the transport in Figure 3.2. Using the properties of determinants, the inner products of the eigenvector representations (3.18) from steps t_s and t'_s are given by

$$\langle \Psi_\alpha^{t_s} | \Psi_\beta^{t'_s} \rangle = \det(B_{\alpha\beta}^{t_s t'_s}), \quad [B_{\alpha\beta}^{t_s t'_s}]_{kl} = \langle \psi_k^-(t_s) | \psi_l^-(t'_s) \rangle, \quad (3.19)$$

where $\langle \psi_k^-(t_s) | (|\psi_l^-(t'_s)\rangle)$ spans now the modes belonging to the state $\langle \Psi_\alpha^{t_s} | (|\Psi_\beta^{t'_s}\rangle)$.

Taking $\{\lambda\} = \{J\}$ to be the control parameter space and assuming T_S to be a sufficiently large, the discrete holonomy (3.13) for the degenerate states (3.18) is

well approximated by

$$\Gamma_C \approx P \prod_{t_s=1}^{T_S-1} \begin{pmatrix} \det(B_{11}^{t_s, t_s+1}) & \det(B_{12}^{t_s, t_s+1}) \\ \det(B_{21}^{t_s, t_s+1}) & \det(B_{22}^{t_s, t_s+1}) \end{pmatrix}. \quad (3.20)$$

This means that there is a simple algorithm to evaluate the holonomy:

1. Diagonalize the Hamiltonian at each step t_s corresponding to a particular coupling configuration J .
2. Form the four inner products (3.19) of the eigenvectors from steps t_s and t_{s+1} .
3. Multiply the matrices containing the inner products together according to (3.20).

This algorithm is convenient for two reasons. First, one never needs to construct the states (3.18), which in general are too large to be stored on a computer. The inner products (3.19) can be evaluated using only the mode spectrum (2.33). Second, all these steps can be carried out in parallel.

3.3.4 The study of the holonomy

To study how the holonomy depends on the system size, degeneracy of the states $|\Psi_\alpha\rangle$ and the fermion gap in a finite system, we calculate Γ_C for a range of K using the three parametrizations shown in Table 3.1.

Adiabaticity of the transport

As the vortices are transported, their relative separations vary. Due to the vortex-vortex interactions, this means that the spectrum varies also with t_s during the braiding process. To consider the effect on Γ_C , we define the minimal fermion gap, Δ , and the maximum energy splitting between the two ground states, δ , by

$$\Delta = \min_{t_s} (E_3^{t_s} - E_2^{t_s}), \quad \delta = \max_{t_s} (E_2^{t_s} - E_1^{t_s}), \quad (3.21)$$

	d	S	T_S	$2L_xL_y$
(i)	2	$2 \cdot 10^3$	$32 \cdot 10^3$	120
(ii)	3	$2 \cdot 10^3$	$48 \cdot 10^3$	224
(iii)	4	$4 \cdot 10^3$	$128 \cdot 10^3$	360

Table 3.1: Three parametrizations (i), (ii) and (iii) for which the holonomy is evaluated. Here d is the minimal vortex separation in units of links, S is the number of steps in changing the sign of the coupling at every link, $T_S = 8Sd$ is the total number of steps in C and $2L_xL_y = 8(d+1)(2d+1)$ gives the number of spins in the system. S has been increased in (iii) to suppress accumulation of discretization errors due to longer path.

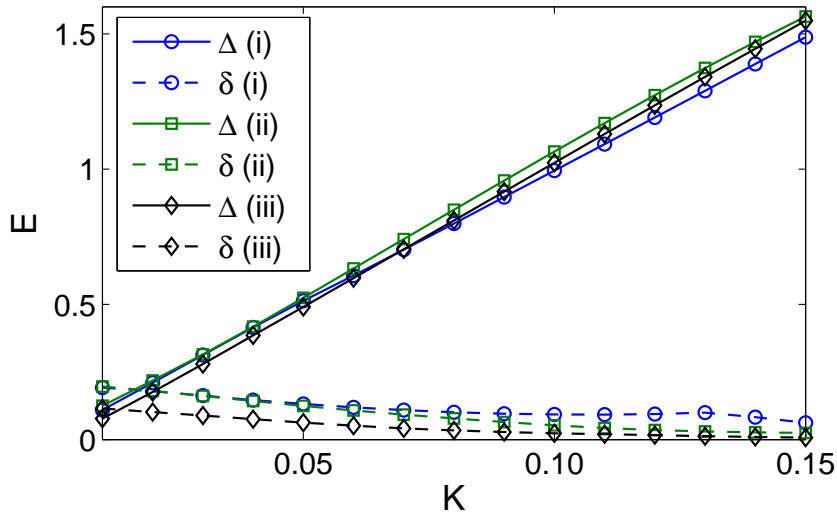


Figure 3.9: The minimal fermion gap Δ and the maximum energy splitting between the ground states δ , (3.21) as functions of K for parametrizations (i), (ii) and (iii) given in Table 3.1. In agreement with the results on the thermodynamic limit, the fermion gap grows linearly and the degeneracy improves with increasing K for all parametrizations. The fermion gap is relatively insensitive to the vortex separation, whereas the degeneracy improves when the vortices are further apart.

respectively, where $E_k^{t_s}$ is now the k th eigenvalue at step t_s . These are plotted in Figure 3.9 for the three parametrizations (i)-(iii) of the holonomy. We observe that both the fermion gap and the level of degeneracy improve as K and d increase. These agree with the behavior in the thermodynamic limit as studied in Section 3.2.

Under the adiabatic approximation the holonomy corresponds to the exact time evolution when $\Delta \gg \delta$ and $\delta \rightarrow 0$ [99]. To physically accommodate these conditions in a finite size system, the vortex transport should be fast enough compared to δ for the states $|\Psi_\alpha^{t_s}\rangle$ to appear as degenerate, but slow enough compared to Δ so that no fermionic excitation is produced.

We expect the parametrization (iii) where the vortices are furthest from each other to be physically the most relevant one. Figure 3.9 shows that for it $\frac{\delta}{\Delta} \lesssim 10^{-2}$ when $K \gtrsim 0.07$. This region can support the adiabaticity conditions and hence we take $K \approx 0.07$ as a lower bound for identifying a stable topological phase for the finite size system in consideration.

The results

To quantitatively study the holonomy, we introduce a fidelity measure for a target matrix U and a test matrix V as

$$s(U, V) = \frac{1}{4} \text{Tr} \left(UV^\dagger + VU^\dagger \right). \quad (3.22)$$

When U and V are unitary 2×2 matrices, we have that $s(U, V) = 1$ if and only if $U = V$, while in general $s(U, V) \leq 1$.

We consider first the unitarity of the transport. It is captured by the fidelity $s(\mathbb{1}, \Gamma_{C_l} \Gamma_{C_l}^\dagger)$, which measures how close $\Gamma_{C_l} \Gamma_{C_l}^\dagger$ is to an identity matrix. We plot it in Figure 3.10(a), where we can see that the unitarity measure is above 98% for all parametrizations (i)-(iii) when $K \lesssim 0.10$. For larger K we observe the unitarity reducing, which we interpret being due to the coarse graining in our simulation. The employed algorithm, (3.20), approximates the holonomy well for the parametrizations (i)-(iii) only when $K \lesssim 0.10$. Therefore, we take this as a bound for our

simulation's physical relevance. Together with the lower bound due to adiabaticity of the transport, we expect the holonomy to coincide with an actual time evolution in the range $0.07 \lesssim K \lesssim 0.10$.

The monodromy \bar{R}^2 , (3.9), is characterized by its off-diagonality. When the transport is unitary, we can also characterize Γ_C by its off-diagonal elements. After the gauge fixing (3.17), we take them to be some complex numbers $[\Gamma_C]_{12} = [\Gamma_C]_{21} = re^{i\theta}$, where $0 \leq r \leq 1$ and $0 \leq \theta \leq 2\pi$. To study Γ_C we construct two different fidelity measures, which take the form:

$$s(|\bar{R}^2|, |\Gamma_C|) = r, \quad (3.23)$$

$$\bar{s}(\bar{R}^2, \Gamma_C) = \frac{1}{2}[s(\bar{R}^2, \Gamma_C) + 1] = \frac{1}{2}[r \cos(\frac{\pi}{4} + \theta) + 1]. \quad (3.24)$$

Here $|U|$ denotes a matrix U with its elements replaced by their absolute values. $s(|\bar{R}^2|, |\Gamma_C|)$ measures the off-diagonality that characterizes \bar{R}^2 , whereas $\bar{s}(\bar{R}^2, \Gamma_C)$ is the total fidelity that accounts also for the overall phase. The residual sign ambiguity in the gauge fixing, (3.17), has been resolved based on the continuity of \bar{s} .

The holonomies for the three parametrizations (i), (ii) and (iii) in Table 3.1 are plotted in Figures 3.10(b)-(d), respectively. We consider each separately:

- (i) The holonomy shows no significant off-diagonality over the considered range of K . We attribute this to the too small size of the system (120 spins) where the vortices are always too near each other ($d = 2$).
- (ii) The holonomy is predominantly off-diagonal for $0.02 \lesssim K \lesssim 0.04$. There is also a small region around $K \approx 0.02$ with $\bar{s} > 0.9$. However, since in this region $\frac{\delta}{\Delta} > 10^{-1}$, the adiabaticity conditions do not hold and thus we disregard it as unphysical.
- (iii) The holonomy is predominantly off-diagonal for $0.02 \lesssim K \lesssim 0.09$. The total fidelity, \bar{s} , has two regimes of interest in this region. Around $0.02 \lesssim K \lesssim 0.05$ it takes the limiting value $\bar{s} \approx 0.481$, and in the region $0.08 \lesssim K \lesssim 0.10$ it peaks at $\bar{s} \approx 0.991$. These correspond to overall phases of the so called $SU(2)_2$ ($\bar{s} = 1/2$)

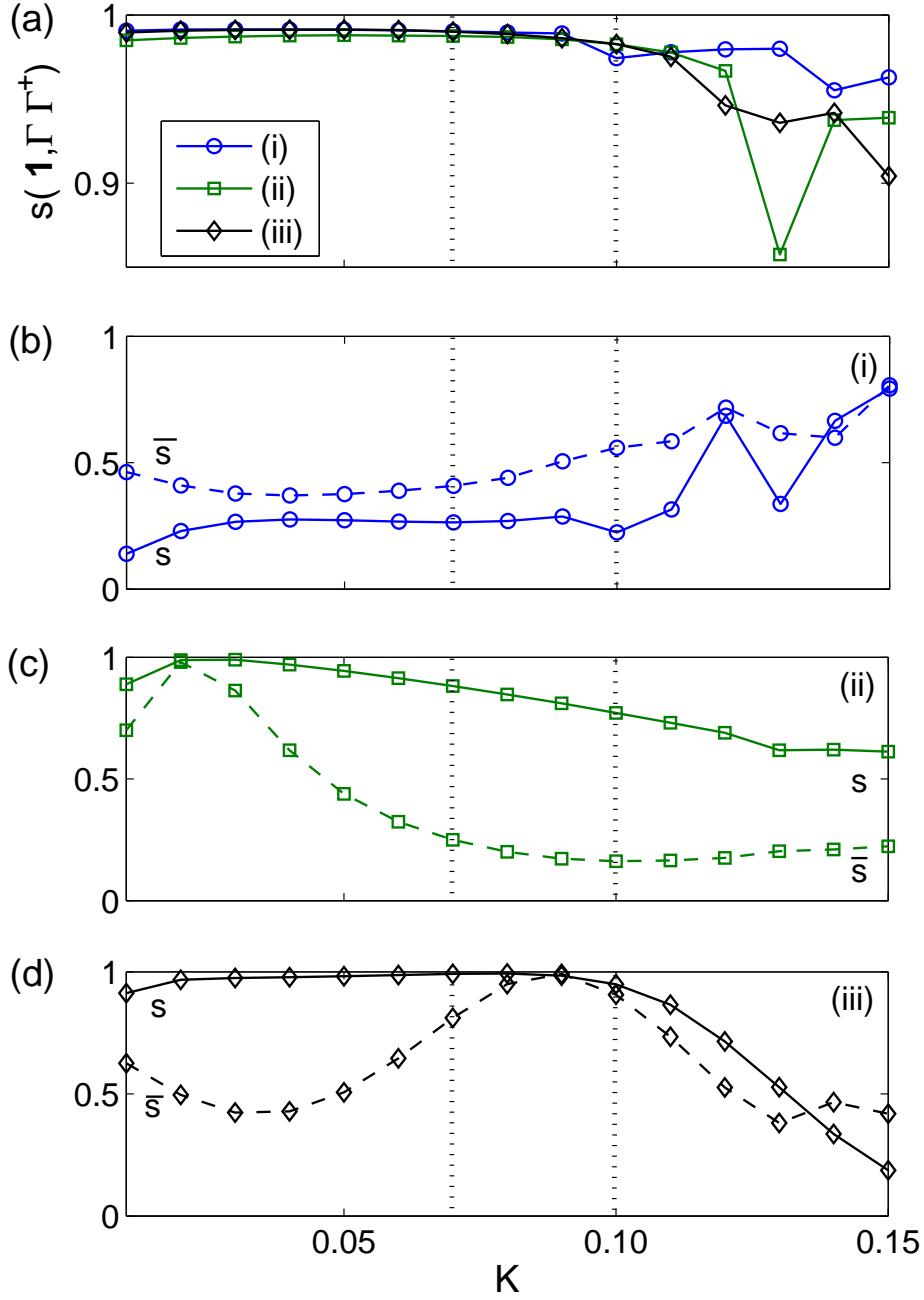


Figure 3.10: (a) The unitarity measure, $s(\mathbb{1}, \Gamma_{C_l} \Gamma_{C_l}^\dagger)$, as a function of K for the three configurations given in Table 3.1. The measure of off-diagonality, $s(|\bar{R}^2|, |\Gamma_{C_l}|)$, and the total fidelity, $\bar{s}(\bar{R}^2, \Gamma_{C_l})$, as a function of K for the parametrizations (b) (i), (c) (ii) and (d) (iii). Based on unitarity and the adiabaticity, we expect a stable phase in the area $0.07 \lesssim K \lesssim 0.10$ bounded by the dashed vertical lines.

and the Ising anyons ($\bar{s} = 1$), respectively. Both theories have the same particle content with the fusion rules (2.28), but their statistics differ [10]. We disregard the again $0.02 \lesssim K \lesssim 0.05$ regime, because it does not accommodate the adiabaticity conditions. On the other hand, the $0.08 \lesssim K \lesssim 0.10$ regime is physically relevant in the light of both adiabaticity and the coarse graining in our simulation. In this regime the holonomy is both off-diagonal and has the highest total fidelity.

Finally, we verify the topological nature of our calculation for all the parametrizations. First, when the evolution is topologically trivial as shown in Figure 3.7(c), $\Gamma_{C_o} \approx \mathbb{1}$ with error less than 10^{-2} . Second, when the orientation of the braiding is reversed, we obtain inverse evolution, i.e. $\Gamma_{C_l^{-1}} = \Gamma_{C_l}^\dagger$. Third, the holonomy is not affected by path deformations $C \rightarrow C'$, i.e. $\Gamma_C = \Gamma_{C'}$, as long as the topology of the path remains invariant. Together these mean that the holonomy Γ_C depends only on the space-time topology of the path C when it is chosen as shown in Figure 3.7(a). The result of our simulation should therefore correspond to the statistics of the vortices.

3.3.5 Discussion

The main results are that the off-diagonality of the holonomy Γ_C improves systematically with the system size, and that the highest total fidelity $\bar{s} \approx 0.991$ appears in the physical region $0.07 \lesssim K \lesssim 0.10$. We regard these giving a validation of the non-Abelian nature of the vortices as well as providing strong support that they are indeed Ising anyons. Our method is validated by the explicit demonstration that the holonomy depends only on the space-time topology of the path C .

In Section 3.2 we identified the length scale ξ associated with the vortex-vortex interactions. The improvement of the holonomy with increasing system size can be directly related to the minimal vortex separation becoming larger and larger than ξ . For the parametrization (iii), there holds always $d \gtrsim 4\xi$ in the physical region, which provides damping of the interactions by a factor of at least 10^{-2} . We regard

this as providing a good approximation of the $d_s \gg \xi$ criteria for the topological behavior to emerge in a finite size system.

The physical domain of K was chosen such that it accommodated both the adiabaticity and unitarity. The first was based on the energy splitting and fermion gaps, while the latter is due to the coarse graining in the simulation. Although we observe systematic improvement of off-diagonality with increasing system size, strictly speaking only the parametrization (iii) accommodates both of these criteria simultaneously. In order to unambiguously confirm that the statistics converges to the Ising statistics as the system size increases, one needs better numerics with larger vortex separation d and more continuous transport, i.e. larger S . Larger systems should also resolve the asymmetry between the off-diagonality and the total fidelity. The first exhibits now systematic improvement with the system size, while such behavior is absent for the latter. It would be interesting to study whether the phase is indeed more sensitive to the degeneracy splitting than the non-Abelian character given by the off-diagonality. Were the model ever employed for quantum information processing, such studies would relate directly to the fidelities of quantum gates.

Our method of tuning the couplings J on the links along the path can be directly translated, given sufficient site addressability, to how one could perform vortex transport in the experiments. Therefore, a calculation like ours provides exact predictions for experiments performed in finite size systems. However, it has been recently shown that the sector with a single ψ -particle should not actually exist on a torus [68]. This problem could be circumvented by carrying out a similar calculation with a third vortex pair far away from the two used in the braiding. This can be used to hide another ψ particle, such that the fermionic parity is even and the degenerate ground states are still separated from the rest of the spectrum by the energy gap. This calculation would be technically identical to ours and thus we would expect similar results. Unfortunately systems of this nature were too large for us to consider and thus better numerics are again desirable.

The reason we carried out the calculation in the sector with a single ψ -particle

is purely technical. In order to calculate the inner products, (3.19), required for the holonomy, the two degenerate states, (3.18), have to include an equal number of the modes $|\psi_i^-\rangle$. In a sector with four vortices, this is possible only when employing states that differ by the inclusion of the zero mode z_1^\dagger or z_2^\dagger . Physically there is nothing prohibiting considering the global vacuum sector. It would be desirable to find a method to carry out a similar calculation also directly there.

Despite of these technical limitations, we regard our study providing an important general demonstration that a direct calculation of non-Abelian statistics is possible in a variety of physically relevant systems. Similar calculations have been performed previously by only using trial wave functions [34, 94, 100]. Ours is the first to employ exact eigenstates.

3.4 Summary

In this chapter we have explicitly demonstrated the non-Abelian fusion rules and braid statistics of the Ising anyons by using the exact solutions of the model. In the first part we found that the anyonic vortices are interacting with a characteristic length ξ that depends inversely on the magnitude K of the time-reversal symmetry breaking term. When the vortices are nearby, the interactions allowed us to associate different degenerate states with the fusion degrees of freedom.

In the second part we calculated the braid statistics as a holonomy associated with process where a vortex is transported around another. For the largest considered system where the vortex separation satisfied $d > 4\xi$, we found a region in K where the holonomy coincides with high fidelity to the statistics of the Ising anyons. As this region also accommodates the adiabaticity conditions, we regard it as a strong direct evidence for existence of non-Abelian anyons in the honeycomb lattice model.

This concludes “The Dirty Work”, which consisted of the explicit demonstration of properties which, in a sense, were all anticipated by a single integer, the Chern number $\nu = -1$. However, we showed that the information it gives on the physics

of the system is limited. New physics was discovered in the form of the interactions, which set limits on the system size and the vortex density for the predicted topological behavior to be manifest. Understanding these limits is of crucial importance to experiments, which will eventually be performed in finite size systems. Also, only by understanding the microscopics of the system can one envisage control procedures to carry out the experiments. A prime example of this is our method of simulating vortex transport through manipulating the couplings J locally. As this corresponds to how transport could be implemented also in laboratory, the performed calculations provide exact predictions for such experiments. Likewise, the energy gaps and the lifting of zero mode degeneracy provide measures of stability and ways to detect the fusion channels of the vortices, respectively.

The essential new discovery was the interactions, that are not part of the pure topological theory, but arise due to the underlying microscopic model. Their role has so far been two-fold. The identification of the zero modes with fusion channels was only possible because of them. On the other hand, they made the calculation of the statistics harder resource-wise. The vortices had to be kept as far as possible, and thus larger systems were required. However, their significance for the physics of the honeycomb lattice model goes beyond just modifying the pure topological theory. In the next chapter we will show that the interactions can drive phase transitions to completely new topological phases.

Chapter 4

Going Beyond: A New Chiral Topological Phase

In this chapter we study the B -phase in the full-vortex sector of the honeycomb lattice model. In Section 4.1 we obtain the band structure analytically and outline the phase space of the full-vortex sector. The B -phase is characterized now by Chern number $\nu = \pm 2$, which implies a new phase where the vortices behave as chiral Abelian anyons. By studying the Fermi surface of the model, we identify an emergent symmetry that is responsible for the new phase. To study the transitions to the toric code ($\nu = 0$) and Ising ($\nu = -1$) phases, we consider in Section 4.2 the evolution of the Fermi surface under global perturbations. This is discovered to be equivalent to considering the low-energy field theory of Dirac fermions coupled to gauge fields. We identify two distinct types of topological phase transitions based on Fermi surface symmetries and outline the extended phase space. Finally, in Section 4.3 we illustrate the role of anyon-anyon interactions on the transition between the non-Abelian Ising phase and the new chiral Abelian phase.

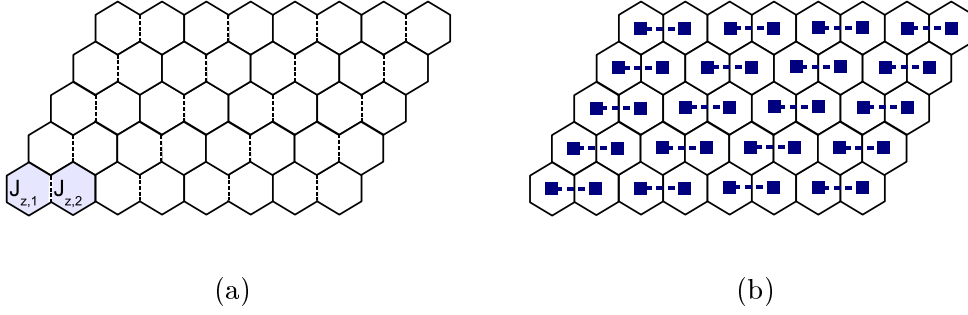


Figure 4.1: The full-vortex configuration can be created, for instance, by allowing the sign J_z to alternate in direction \mathbf{n}_x , while keeping the J_x and J_y couplings positive. Dashed links denote the links where $J_z < 0$. (a) Inside the two plaquette unit cell this is equivalent to setting $J_{z,1} = -J_{z,2}$, which gives (b) a vortex on every plaquette.

4.1 The full-vortex sector

The chiral Abelian phase emerges in the B -phase ($J_x \approx J_y \approx J_z$ and $K > 0$) of the full-vortex sector ($w_p = -1$ on all plaquettes). This sector can be created by choosing a $(2,1)$ -unit cell and using a gauge where, for instance, u_{ij} alternates on z -links in direction \mathbf{n}_x . In terms of couplings, (3.1), this is equivalent to setting inside the unit cell $J_{z,1} = -J_{z,2}$ as illustrated in Figures 4.1(a) and 4.1(b).

Inserting these couplings into (2.15)-(2.18), we obtain a Hamiltonian which is unitarily equivalent to [86]

$$H_{\mathbf{p}} = \begin{pmatrix} h_{bb} & h_{bw} \\ h_{bw}^\dagger & -h_{bb}^\top \end{pmatrix}, \quad (4.1)$$

where

$$h_{bw} = \begin{pmatrix} i(J_x e^{ip_x} + J_y e^{ip_y}) & iJ_z \\ iJ_z & i(-J_x e^{ip_x} + J_y e^{ip_y}) \end{pmatrix} \quad (4.2)$$

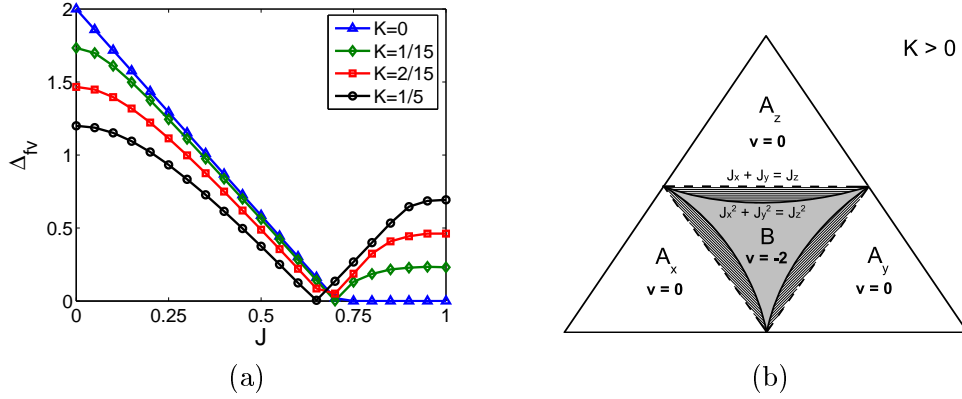


Figure 4.2: (a) The fermion gap Δ^{fv} as a function of $J = J_x = J_y$ when $J_z = 1$ for different values of K . The gap vanishes at $J = 1/\sqrt{2}$ when $K = 0$, but shifts to smaller J as K is increased. When $J = 1$ the gap scales as $\Delta^{fv} \approx 2\sqrt{2}K$. (b) The phase diagram of the full-vortex sector. The shaded area shows the region where the phase transitions occurs with the exact value of J_z depending on K . In the full-vortex sector the B -phase supports chiral Abelian anyons described by Chern number $\nu = -2$.

and

$$h_{bb} = K \begin{pmatrix} \sin(p_x - p_y) & \sin(p_y) - i \cos(p_x) \\ \sin(p_y) + i \cos(p_x) & -\sin(p_x - p_y) \end{pmatrix}. \quad (4.3)$$

Diagonalization gives again the double spectrum with the eigenvalues

$$\pm E_{i,\mathbf{p}} = \pm 2\sqrt{f(\mathbf{p}) + (-1)^i 2\sqrt{g(\mathbf{p})}}, \quad i = 1, 2, \quad (4.4)$$

where

$$\begin{aligned} f_{\mathbf{p}} &= J_x^2 + J_y^2 + J_z^2 + 4K^2(\sin^2(p_x - p_y) + \sin^2 p_y + \cos^2 p_x), \\ g_{\mathbf{p}} &= J_x^2 J_y^2 \cos^2(p_x - p_y) + J_x^2 J_z^2 \sin^2 p_x + J_y^2 J_z^2 \cos^2 p_y + \\ & 4K^2 \left[J_x^2 \sin^2 p_y + J_y^2 \cos^2 p_x + J_x^2 \sin^2(p_x - p_y) \right. \\ & \quad \left. - (J_x J_y + J_x J_z + J_y J_z) \sin(p_x - p_y) \sin p_y \cos p_x \right]. \end{aligned}$$

The expressions for the eigenvectors are too complicated to be obtained analytically.

Similar to the study of the vortex-free sector in Section 2.3, we outline the phase space structure of the full-vortex sector by considering the behavior of the energy gap

$$\Delta^{fv} = \min_{\mathbf{p}} E_{1,\mathbf{p}}. \quad (4.5)$$

Figure 4.2(a) shows the behavior of Δ^{fv} as functions of J and K . In contrast to the vortex-free sector, in the full-vortex sector the gap persists deeper into the B -phase with the gap closing point depending now also on K . This in agreement with [86], where the phase boundaries for $K = 0$ between the A - and B -phases in the full-vortex sector were shown to be

$$|J_x|^2 = |J_y|^2 + |J_z|^2, \quad |J_y|^2 = |J_z|^2 + |J_x|^2, \quad |J_z|^2 = |J_x|^2 + |J_y|^2. \quad (4.6)$$

The B -phase is again gapped only if $K \neq 0$. The phase space of the full-vortex sector is illustrated in Figure 4.2(b).

Evaluating the Chern numbers, (2.26), in the full-vortex sector, one finds that the A_α -phases still give $\nu = 0$ implying Abelian toric code anyons. However, the B -phase gives now $\nu = -2$, which means it is a new topologically ordered phase. In this phase the vortices behave as certain chiral Abelian anyons as catalogued in [62]. To clarify how vortices can appear in the full-vortex sector, we emphasize again that the full-vortex sector should be viewed as the sign-alternated coupling configuration over the vortex-free sector (see Figures 4.1(a) and 4.1(b)). Over this background vortices can be defined as usual through the plaquette operators (2.9).

4.1.1 Symmetries of the Fermi surface

To understand why the B -phase turns out to be described by a new topological phase, we study first its spectrum. Let us normalize the couplings as $J_x = J_y = 1$ and $J_{z,1} = -J_{z,2} = 1$, which amounts to considering the system in the middle of the B -phase. In particular, we are interested in the *Fermi surface*, the manifold of occupied states of highest energy, that plays an integral role in fermion systems [79].

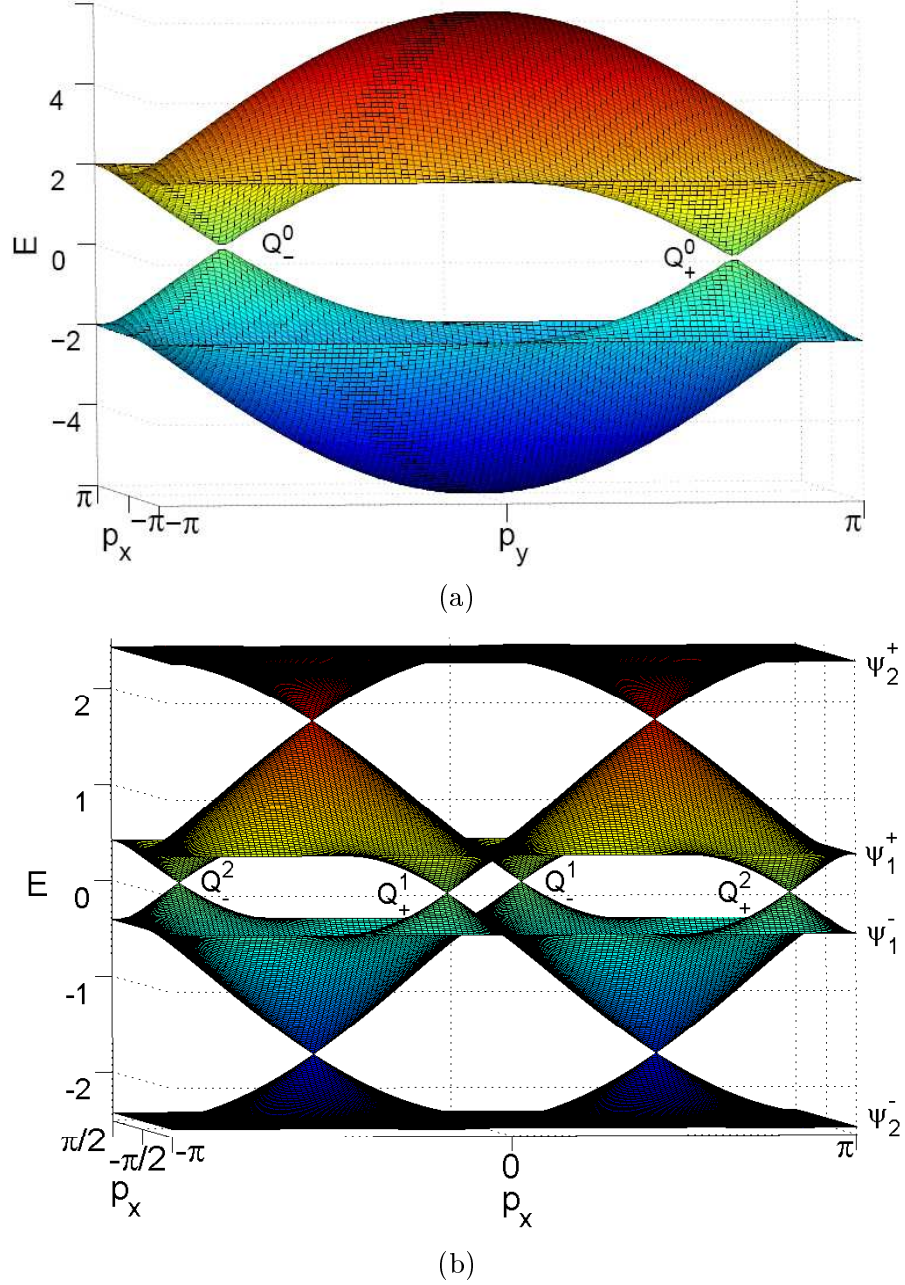


Figure 4.3: (a) The vortex-free band structure, (2.23), and (b) the full-vortex band structure, (4.4), of the phase B plotted across the first Brillouin zone when $J_x = J_y = J_z = 1$ and $K = 0$. In the first case there are two Fermi points at $\mathbf{Q}_{\pm}^0 = \pm(\frac{2\pi}{3}, -\frac{2\pi}{3})$, whereas in the latter case there are four Fermi points at $\mathbf{Q}_{\pm}^1 = \mp(\frac{\pi}{3}, \frac{\pi}{6})$ and $\mathbf{Q}_{\pm}^2 = \pm(-\frac{\pi}{3}, \frac{5\pi}{6})$. The dispersion relation is linear around all the Fermi points.

Chapter 4. Going Beyond: A New Chiral Topological Phase

Different Fermi surface topologies correspond in general to different phases.

In our case the Fermi surface coincides with the band $-E_{1,\mathbf{p}}$, as it contains the states highest (lowest negative) energy that belong to the ground state (2.20). It is best visualized by plotting the band structure across the first Brillouin zone. For comparison, we plot in Figures 4.3(a) and 4.3(b) the band structure of both the vortex-free, (2.23), and full-vortex sectors, (4.4). Both are characterized by conical *Fermi points* around which the dispersion relation is linear. To be precise, there are momenta \mathbf{Q} around which $E_{1,\mathbf{p}}$ satisfies

$$E_{1,\mathbf{Q}} = 0, \quad E_{1,\mathbf{Q}+\mathbf{k}} \sim \mathbf{k}, \quad |\mathbf{k}| \ll 1. \quad (4.7)$$

The crucial difference is that while the vortex-free sector that has two Fermi points ($\mathbf{Q}_{\pm}^0 = \pm(\frac{2\pi}{3}, -\frac{2\pi}{3})$), the full-vortex sector has four ($\mathbf{Q}_{\pm}^1 = \mp(\frac{\pi}{3}, \frac{\pi}{6})$ and $\mathbf{Q}_{\pm}^2 = \pm(-\frac{\pi}{3}, \frac{5\pi}{6})$). This means that they have distinct topologies, and hence correspond to different phases in agreement with different Chern numbers. For $K > 0$ the Fermi points are gapped with the dispersion relation around them becoming quadratic. However, the characterization of the phases based on their Fermi surface topologies still holds. Only when gaps close and reopen can the topology change permanently.

As the Fermi surface topology can differentiate between different phases, it is important to understand what physical properties of a theory can give rise to a particular Fermi surface. These are in general related to the global spatial symmetries Hamiltonian, which act locally in the momentum space. Let us consider the Hamiltonian (4.1) of the full-vortex sector, which has the following symmetries when $K = 0$:

$$\Gamma = \sigma^z \otimes \mathbb{1} : \quad \Gamma H_{\mathbf{p}} \Gamma^{\dagger} = -H_{\mathbf{p}}, \quad (4.8)$$

$$\Theta = \sigma^x \otimes \mathbb{1} : \quad \Theta H_{\mathbf{p}} \Theta^{\dagger} = -H_{-\mathbf{p}}, \quad (4.9)$$

$$\Lambda = \mathbb{1} \otimes \sigma^y : \quad \Lambda H_{\mathbf{p}} \Lambda^{\dagger} = -H_{\mathbf{p}+\pi\mathbf{n}_y}. \quad (4.10)$$

Γ and Θ describe the particle-hole and sublattice symmetries that guarantee the

double spectrum and the even number of Fermi points, respectively. They both arise due to the honeycomb lattice geometry and they are therefore present already in the vortex-free Hamiltonian with the spectrum shown in Figure 4.3(a).

The symmetry Λ is new and specific only to the full-vortex sector. It acts on the indices that correspond to the two z -links inside the unit cell. Exchanging these links maps $(J_{z,1}, J_{z,2}) = (-1, 1) \rightarrow (1, -1)$, which preserves the full-vortex sector. It is still a non-trivial transformation, because the corresponding gauges are inequivalent under the local gauge transformations D_i , (2.6). At the level of the honeycomb lattice, Λ can be thought of as an emergent global Z_2 lattice symmetry, that is responsible for the further doubling of the Fermi points. In Section 4.3 we provide another interpretation in terms of the vortex-vortex interactions.

When $K \neq 0$, i.e. when the time-reversal symmetry is broken, the symmetries (4.8)-(4.10) hold no longer independently. However, they can be combined such that the Hamiltonian still satisfies

$$\Gamma_1 \equiv i\Gamma\Theta = \sigma^y \otimes \mathbb{1} : \quad \Gamma_1 H_{\mathbf{p}} \Gamma_1^\dagger = H_{-\mathbf{p}}, \quad (4.11)$$

$$\Gamma_2 \equiv \Gamma\Lambda = \sigma^z \otimes \sigma^y : \quad \Gamma_2 H_{\mathbf{p}} \Gamma_2^\dagger = H_{\mathbf{p} + \pi \mathbf{n}_y}. \quad (4.12)$$

These guarantee that the double spectrum structure still holds and that the relative locations of the Fermi points remain invariant even when they are gapped. As the structure of the Fermi surface is fully contained in the symmetries (4.11) and (4.12), it is natural to expect that breaking them will lead phase transitions. This will be the topic of next section.

4.2 The Fermi surface evolution

In principle one could carry out an analysis like that of Chapter 3 to verify the characteristic properties of the new chiral Abelian anyons. We leave this for future work and concentrate here instead on the phase transitions. This is performed by studying the evolution of the Fermi surface that was shown above to distinguish the

different phases. Unlike the Chern number, the Fermi surface evolves continuously under perturbations and hence it provides a natural setting to study the phase transitions. To this end we consider the low-energy theory of Dirac fermions, which allows us to relate the Chern number to the Fermi surface topology and provides a dual picture in terms of coupling to gauge fields.

4.2.1 The low-energy field theory of Dirac fermions

We have identified above the global Hamiltonian symmetries (4.11) and (4.12) that are responsible for the distinct Fermi surface topologies. At the phase transitions where the topologies change, the Fermi points have to be created or annihilated pairwise unless both symmetries are simultaneously broken. Therefore, it is natural to assume that perturbations which drive phase transitions lead to a continuous transport of the Fermi points. The way this occurs is most conveniently studied by considering the low-energy theory around the Fermi points.

We set again $J_x = 1, J_y = 1$ and $(J_{z,1}, J_{z,2}) = (-1, 1)$, i.e. consider the system first at the center of the chiral Abelian phase. The linearization is performed by expanding the Hamiltonian (4.1) to first order around the Fermi point \mathbf{Q} by writing $\mathbf{p} = \mathbf{Q} + \mathbf{k}$, with $|\mathbf{k}| \ll 1$. In general, one obtains

$$H_{\mathbf{Q}} = H_{\mathbf{Q}}^0 + H_{\mathbf{Q}}^x k_x + H_{\mathbf{Q}}^y k_y + \mathcal{O}(k^2), \quad (4.13)$$

for some 4×4 matrices $H_{\mathbf{Q}}^n$. When $K = 0$, $H_{\mathbf{Q}}^0$ must have two zero eigenvalues. It follows that we can define a projection onto the 2-dimensional low-energy space by

$$\bar{H}_{\mathbf{Q}} = P U_{\mathbf{Q}} H_{\mathbf{Q}} U_{\mathbf{Q}}^\dagger P, \quad (4.14)$$

where in our normalization $U_{\mathbf{Q}} H_{\mathbf{Q}}^0 U_{\mathbf{Q}}^\dagger = \text{diag}(\sqrt{6}, 0, 0, -\sqrt{6})$ and $P = \text{diag}(0, 1, 1, 0)$. Around each of the four Fermi points \mathbf{Q}_{\pm}^i , the Hamiltonian becomes

$$\bar{H}_{\mathbf{Q}_{\pm}^i} \approx \boldsymbol{\sigma}_{\pm}^i \cdot \mathbf{k}^i \mp \sigma^z \frac{K}{2\sqrt{3}}. \quad (4.15)$$

Here $\sigma_{\pm}^i = (\sigma^x, \pm(-1)^i \sigma^y)$ give different representations of the algebra of Dirac matrices in two dimensions [101]. The momentum has been rescaled by $\mathbf{k}^i = (\frac{a_i k_x - k_y}{1+a_i}, \frac{k_x - a_i k_y}{1+a_i})$, with the Fermi point dependent constant being given by $a_i = 2 - (-1)^i \sqrt{3}$.

Fermi surface topology and the Chern number

Because the low-energy Hamiltonian (4.15) is linear in \mathbf{k} , it describes relativistic Dirac fermions [101]. Due to the appearance of the term proportional to σ^z , the fermions are massive. We interpret this mass to be due to a scalar field of magnitude K , which couples chirally, i.e. with a different sign, at the different Fermi points. The effect of such chiral coupling is to give opposite mass to the Dirac fermions at \mathbf{Q}_+^i and \mathbf{Q}_-^i . This general mechanism where the Fermi points are gapped due to time-reversal symmetry breaking was discovered by Haldane [82]. It is known to give rise to a chiral phase, which is characterized by a non-zero Chern number such that every Fermi point pair will contribute $\nu = \pm 1$.

We can verify this argument in our case by using a topological argument given by Kitaev [62], which relates the Fermi surface topology to the Chern number. Let us first normalize the Hamiltonian (4.15) by $\hat{H}_{\mathbf{k}} = \bar{H}_{\mathbf{k}}/|\bar{H}_{\mathbf{k}}|$. As a function of \mathbf{k} across the whole Brillouin zone, $\hat{H}_{\mathbf{k}}$ can then be interpreted as defining an orientation preserving mapping from a torus (the first Brillouin zone) to a unit sphere enclosing the origin (coordinates given in the basis $\{\sigma^\alpha\}$). The number of times this map winds around the sphere gives the Chern number [102]. When $K = 0$ the orientation of the Fermi points can be characterized by the winding number [103]

$$\mu_Q = \frac{1}{4\pi i} \oint_{C_Q} \text{Tr} (\Gamma H_{\mathbf{p}}^{-1} dH_{\mathbf{p}}), \quad (4.16)$$

where C_Q is a loop in the momentum space around Fermi point \mathbf{Q} and $\Gamma = \sigma^z \otimes \mathbb{1}$. This orientation is preserved for non-zero K . Due to the chiral coupling of $K > 0$, the neighborhoods of both \mathbf{Q}_+^i (\mathbf{Q}_-^i) with orientations $\mu_{Q_+^i} = +1$ ($\mu_{Q_-^i} = -1$) are mapped to the lower (upper) hemisphere. As the contribution of K vanishes away

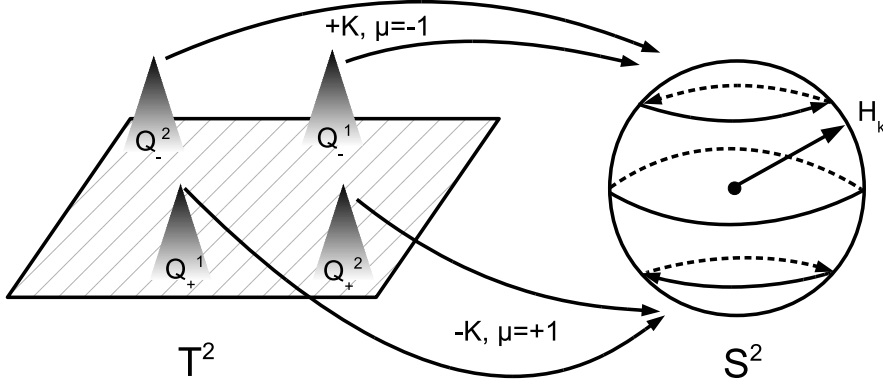


Figure 4.4: The normalized Hamiltonian $\hat{H}_{\mathbf{k}}$ defines a mapping from the Brillouin zone, which is topologically a torus T^2 , to a unit sphere S^2 . Depending on the sign of the term $\pm K\sigma^z$, the Fermi points are mapped to either lower or upper hemisphere. As the ones with same orientations μ end up to same hemispheres, the map winds around the unit sphere twice when viewed from the origin.

from the Fermi points, the rest of the Brillouin zone is mapped to the equator. We illustrate this in Figure 4.4. When viewed from the origin enclosed by the unit sphere, the four Fermi points imply that the map winds twice around the sphere giving the Chern number $\nu = -2$.

4.2.2 Topological phase transitions driven by gauge fields

We have seen above that Fermi points together with the chiral scalar field K give rise to a topologically ordered phase characterized by a non-zero Chern number. Even though a non-zero K is required to open the energy gaps and calculate the Chern number, it does not alter significantly the locations of the Fermi points, which depend predominantly only on the couplings J . Therefore, the phase transitions are due to J perturbations, that can transport the Fermi points. In the low-energy theory of Dirac fermions, this is equivalent to coupling to gauge fields as shown below. We set $K = 0$ for the time being and consider the system in the middle of the chiral Abelian phase ($J_x = 1, J_y = 1$ and $(J_{z,1}, J_{z,2}) = (-1, 1)$).

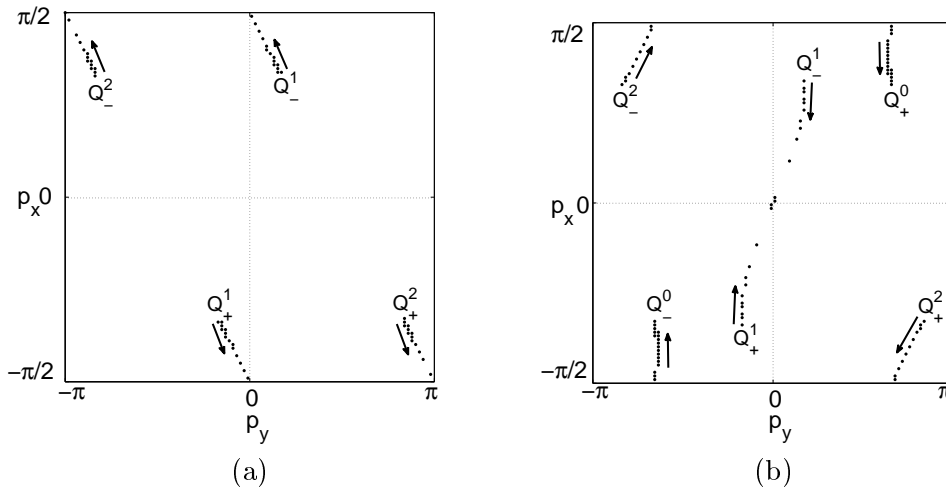


Figure 4.5: A numerical study of the evolution of Fermi point locations (black dots) across the first Brillouin zone when (a) $\delta J_1 = 0 \rightarrow \infty$ ($\nu = -2 \rightarrow 0$ transition) and (b) $\delta J_2 = 0 \rightarrow 1$ ($\nu = -2 \rightarrow -1$ transition). In (a) all the Fermi points annihilate when $\delta J_1^c = \sqrt{2} - 1$, whereas in (b) only the \mathbf{Q}_{\pm}^1 Fermi points annihilate when $\delta J_2^c = \frac{1}{4}$.

Transition to the toric code ($\nu = 0$) phase

Let us consider first the transition to the phase with non-chiral Abelian toric code anyons ($\nu = 0$). It appears, for instance, when $|J_z| \gg |J_x|, |J_y|$ as shown in Figure 4.2. In this limit the transition can be understood as being due to dimerization on the z -links.

We model it as the Hamiltonian perturbation $\delta H_1 = i\delta J_1 \sum_{\mathbf{r}} c_{b,\mathbf{r}} c_{w,\mathbf{r}}$, which in the linearized picture (4.13) around each of the four Fermi points translates to

$$\delta H_{1,\mathbf{Q}_{\pm}^i}^0 = -\delta J_1 \sigma^y \otimes \sigma^x. \quad (4.17)$$

Let us treat the Fermi points \mathbf{Q}_+^i and \mathbf{Q}_-^i as being paired, such that we can combine their Hamiltonians (2.14) as

$$\bar{H}_{\mathbf{Q}^i} = \text{diag}(\bar{H}_{\mathbf{Q}_+^i}, \bar{H}_{\mathbf{Q}_-^i}). \quad (4.18)$$

Assuming then the perturbation to be small, i.e. $\delta J_1 \ll 1$, a projection, (4.14), of

the perturbation (4.17) gives the low-energy Hamiltonian

$$\bar{H}_{\mathbf{Q}^i} + \delta \bar{H}_{j, \mathbf{Q}^i} = \boldsymbol{\alpha}^i \cdot (\mathbf{k}^i + \gamma^5 \mathbf{A}_j^i). \quad (4.19)$$

Here $\boldsymbol{\alpha}^i = (\mathbb{1} \otimes \sigma^x, (-1)^i \sigma^z \otimes \sigma^y)$ form a four-dimensional representation of the Dirac α -matrices, $\gamma^5 = \sigma^z \otimes \mathbb{1}$ is the chiral matrix and

$$\mathbf{A}_1^i = \delta J_1 \frac{(a_i - 1)}{a_i + 1} (1, 1). \quad (4.20)$$

This Hamiltonian describes the Dirac fermions being coupled to a gauge field \mathbf{A}_1^i . In particular, due to the appearance of γ^5 , which describes \mathbf{A}_1^i coupling at the paired Fermi points \mathbf{Q}_+^i and \mathbf{Q}_-^i with opposite signs, we interpret it as a chiral gauge field [104].

As $\mathbf{k}^i = (0, 0)$ no longer gives a vanishing Hamiltonian, the coupling to the gauge field shifts the Fermi points \mathbf{Q}_+^i and \mathbf{Q}_-^i by \mathbf{A}_1^i . Due to chiral coupling, both of the paired points are shifted towards each other, such that the direction is the same for both pairs. This agrees with $\delta H_{1, \mathbf{Q}_\pm^i}^0$ respecting both symmetries (4.11) and (4.12). It implies also that if the Fermi points are to vanish, they have to do it simultaneously. This is indeed the case as shown in Figure 4.5(a), where we plot the trajectories of the Fermi points as functions of the perturbation magnitude δJ_1 . It demonstrates that dimerization in the large δJ_1 limit can cause localization of the fermions on the z -links and thus completely remove the Fermi points.

Transition to the Ising anyon ($\nu = -1$) phase

We can similarly study the transition to the non-Abelian Ising phase ($\nu = -1$), which occurs for the uniform coupling configuration $(J_{z,1}, J_{z,2}) = (1, 1)$. Changing the sign of the couplings on alternating z -links can be modelled by the Hamiltonian perturbation $\delta H_2 = i\delta J_2 \sum_{\mathbf{r}} (1 - e^{i\pi \mathbf{r} \cdot \mathbf{n}_x}) c_{b, \mathbf{r}} c_{w, \mathbf{r}}$, which interpolates between the sign-alternated ($\delta J_2 = 0$, full-vortex sector) and the uniform ($\delta J_2 = 1$, vortex-free sector) couplings configurations.

A linearization of this perturbation around the four Fermi points gives

$$\delta H_{2, \mathbf{Q}_{\pm}^i}^0 = \delta J_2 \sigma^y \otimes (\sigma^x - \mathbb{1}), \quad (4.21)$$

which respects the sublattice symmetry (4.11), but breaks (4.12), the emergent symmetry responsible for the chiral Abelian phase. The low-energy theory is again a Dirac field coupled to a chiral gauge field (4.19), but now with

$$\mathbf{A}_2^i = \frac{\delta J_2}{a_i + 1} (1, (-1)^{i+1} \sqrt{3}). \quad (4.22)$$

The crucial difference is that the components of \mathbf{A}_2^i depend now on the Fermi points, which means that the coupling to this field shifts the pairs \mathbf{Q}_{\pm}^1 and \mathbf{Q}_{\pm}^2 independent of each other. This is confirmed by Figure 4.5(b), where the trajectories of the Fermi points are plotted as functions of δJ_2 . It shows that large δJ_2 distortions can cause the \mathbf{Q}_{\pm}^1 Fermi points to annihilate while only transporting the other two.

We interpret the transitions driven by (4.17) and (4.21) as being fundamentally of different type. The first obeys the global symmetries (4.11) and (4.12), but a localization mechanism drives the transition making the A_{α} phases band insulators with no Fermi points. Still, the ground state is topologically ordered, but the chirality is lost when the Fermi points vanish. On the other hand, δJ_2 driven transition is due to a breaking of one of the symmetries and thus does not completely remove the Fermi points. Although the Fermi surface topology, i.e. the number of Fermi points, and the Hamiltonian symmetries responsible for them hold in principle the same information about the phase, we regard the picture of symmetries more illustrative. While the contrary is not always true, a perturbation breaking a Fermi surface symmetry should always lead to a phase transition.

The extended phase space

Because of the symmetries (4.11) and (4.12), the study of the Fermi point transport holds also for $K \neq 0$. As δJ_i is varied, the gapped Fermi points (the minima/maxima

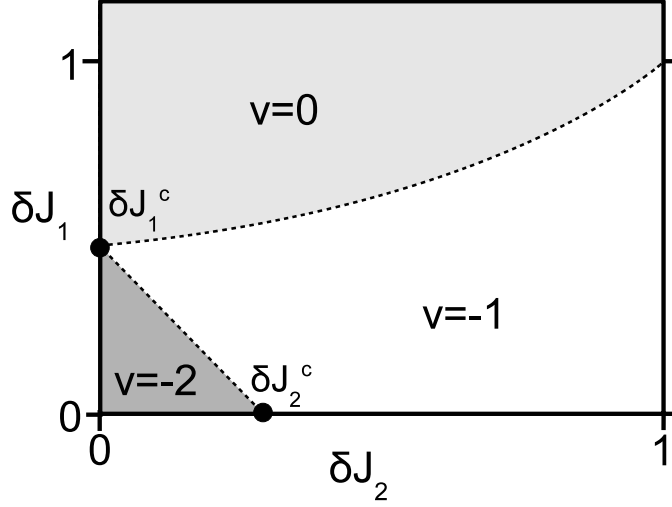


Figure 4.6: A section of the phase space as a function of δJ_1 and δJ_2 when $|J_\alpha| = 1$ and $K > 0$. The dashed lines are the phase boundaries and the circles are the locations of the K dependent critical points $\delta J_1^c = \sqrt{2 + K^2} - 1$ and $\delta J_2^c = \frac{1+K^2}{4}$.

of the bands $E_{1,\mathbf{p}}^\pm$) follow the same trajectories, although slower for larger K . The annihilations still occur at the points $\mathbf{Q}_c = \{(0,0), (\frac{\pi}{2}, 0), (\frac{\pi}{2}, \pi)\}$, where the gap always closes. We can use this information to obtain the K dependent critical points δJ_i^c .

At exactly the critical momenta \mathbf{Q}_c there must hold

$$PU_{\mathbf{Q}_c}(H_{\mathbf{Q}_c}^0 + \delta H_i)U_{\mathbf{Q}_c}^\dagger P = 0, \quad (4.23)$$

which gives at every critical momenta the same single independent equation. For δH_1 , (4.17), and δH_2 , (4.21), this gives the analytic critical points

$$1 + \delta J_1^c = \sqrt{2 + K^2}, \quad (4.24)$$

$$\delta J_2^c = \frac{1 + K^2}{4}, \quad (4.25)$$

respectively. We can see from Figure 4.2(a) that (4.24) agrees with the numerically obtained shifting of the phase transition point.

In Figure 4.6 we outline the extended phase space as functions of δJ_1 and δJ_2 showing the three distinct topological phases. The critical perturbations (4.24) and (4.25) can be translated to relative coupling configurations. In general, the K dependent tri-critical point δJ_1^c occurs when

$$J_z^2 = J_x^2 + J_y^2 + K^2, \quad (4.26)$$

and similarly also for the other phase boundaries, (4.6). Likewise, when $\delta J_1 = 0$ the transition between the chiral phases when occurs when the J_z couplings on the alternating rows satisfy

$$J_{z,1} = \frac{K^2 - 1}{2} J_{z,2}. \quad (4.27)$$

Both (4.26) and (4.27) show that a larger K has a stabilizing effect on the $\nu = -2$ phase by making it more resistant to relative coupling fluctuations. The reason behind this lies in the role of anyon-anyon interactions which are the topic of next section.

4.3 The role of anyon-anyon interactions in the phase transition

The transition from the non-Abelian Ising phase to the chiral Abelian phase has been predicted to arise due to anyon-anyon interactions [14, 25, 105, 106]. The basic idea is that interactions between anyons act as a Hamiltonian on the fusion degrees of freedom by favouring certain fusion channels while assigning an energy penalty to others. This gives rise to a new emergent theory, where the new degrees of freedom are the fusion channels of the underlying anyon model. Although the original microscopic and anyonic properties are lost, the new theory can be thought of as a nucleated topological liquid that can support other types of anyons as collective quasiparticle excitations. Depending on the types of anyons interacting and which fusion channels are favoured, both topological and non-topological phases can

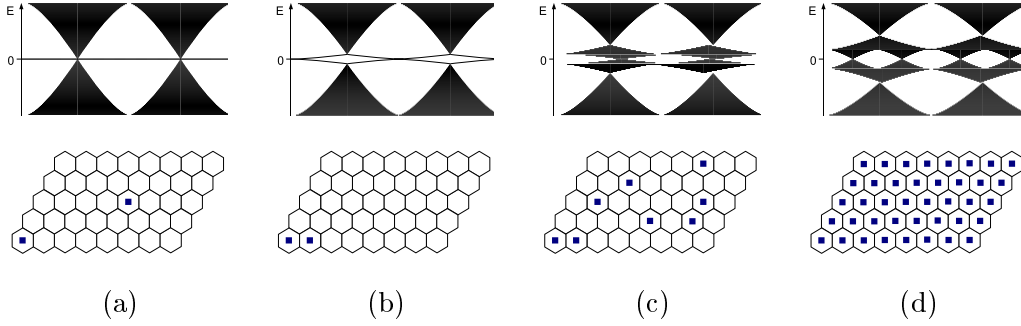


Figure 4.7: A schematic illustration of the emergence of the full-vortex band structure in Figure 4.3 due to interacting anyonic vortices (black squares) as the vortex density is increased. (a) A separated pair of vortices carries a zero mode. (b) Short-range interaction causes the zero mode to acquire momentum dependence. (c) The presence of many interacting vortices causes the zero modes to form a band. (d) The full-vortex band structure.

appear.

As demonstrated by Figure (3.6)(b), the non-Abelian Ising anyons appearing in the honeycomb lattice model are interacting. These interactions exhibit oscillations, (3.3), and their range is controlled by the parameter ξ . When the vortices occupy neighbouring plaquettes, such as in the full-vortex sector, the vacuum fusion channel is always favoured. For this case the general theory predicts that non-Abelian nature is lost, while the chirality is preserved [25]. This is exactly the transition implied by the Chern number change $\nu = -1 \rightarrow -2$, which we have verified both through a direct calculation using eigenstates, (2.26), as well as by studying the Fermi surface evolution, (4.15).

We can establish the role of interactions also from the spectral evolution as the vortex density is increased. Based on numerical studies, we provide a schematic illustration in Figures 4.7(a)-(d):

- (a) As demonstrated in Chapter 3, isolated vortices introduce zero modes, that have zero energy when the vortices are much further from each other than the characteristic interaction length ξ .
- (b) When the vortices are nearby, the zero modes acquire a momentum dependence due to the interactions (3.3).

- (c) When many vortices interact with each other simultaneously, the zero modes describing the fusion channels can be no longer associated with certain vortex pairs. Their characteristic behavior is lost and they start forming a new band structure which is separated from the free-fermion bands.
- (d) Finally, as the vortex density approaches the limiting full-vortex sector, this band acquires the four Fermi points, that characterize the behavior of the new phase. The emergent band and the free-fermion band are separated in energy. Exactly half of the states in the spectrum belong to each.

Based on this spectral evolution, we can identify the bands ψ_1^\pm in Figure 4.3(b) being due to the interacting anyonic vortices, whereas the bands ψ_2^\pm correspond still to the free fermions. As the emergent low-energy bands ψ_1^\pm are responsible for the change in the Fermi surface topology, we can confirm the anyon-anyon interactions as being responsible for the transition.

This role of interactions in the phase transition fits also with the observation that a larger K has a stabilizing effect only on the $\nu = -2$ phase. This has to do with the oscillations in the interactions, (3.3), which imply that anyons at different separations favour different fusion channels. Near the phase boundaries the oscillation period is smaller and thus there is more competition between different fusion channels. A larger K brings down the interaction range ξ and dampens the oscillations, which makes the nearest neighbour interactions stronger relative to longer range ones. Therefore, a larger K extends the area in the phase space where the nearest neighbour interactions responsible for the new phase dominate.

Finally, the role of interactions provides an intriguing alternative way to understand the origin of the emergent symmetry Λ that is responsible for the new phase in the full-vortex sector. Although we can not make this interpretation rigorous yet, we present it here as it paves way to interesting future research. The idea is as follows. In Chapter 3 we reviewed how the Ising anyons can be understood as localized bound states of Majorana fermions γ_i at the vortex cores [83], with the interactions being due to their tunneling [93]. In the full-vortex sector the vortices

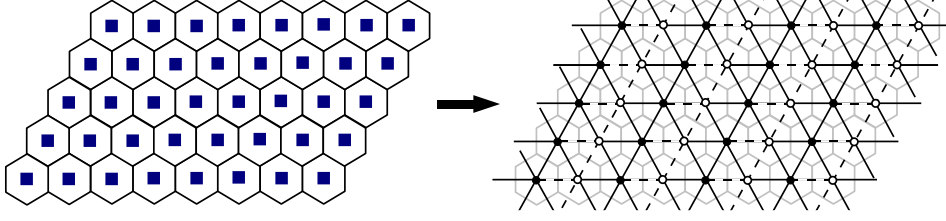


Figure 4.8: In the full-vortex sector the vortices occupy the vertices of the triangular dual lattice of the honeycomb lattice. The ground state for the Hamiltonian for Majorana fermions on a triangular lattice occurs for $\frac{\pi}{2}$ -flux per plaquette. This can be effectively achieved by setting $s_{ij} = 1$ on solid links and $s_{ij} = -1$ on dashed links, which gives a π -flux on every other triangular plaquette. Such configuration is periodic respect to bi-coloring the columns black and white, which gives rise to the lattice symmetry Λ under their exchange.

form a triangular lattice, which is the dual lattice of the honeycomb lattice. We can thus envisage modeling the tunnelings of the Majorana fermions on a triangular lattice by a Hamiltonian

$$H = t \sum_{ij} s_{ij} \gamma_i \gamma_j, \quad (4.28)$$

where the t is the tunneling amplitude related to the nearest neighbour interactions and $s_{ij} = \pm 1$ describes a local gauge freedom. The ground state of such Hamiltonian occurs when one imposes a $\frac{\pi}{2}$ -flux per triangular plaquette [106], which requires the unit cell to contain two sites, i.e. two vortices on the honeycomb lattice (see Figure 4.8). Therefore, we conjecture that the symmetry Λ , (4.10), acting on the z -links of the honeycomb lattice, is inherently a lattice symmetry on the vortex lattice. Likewise, we postulate that the states in the bands $|\psi_{\pm}^{\pm}\rangle$ are eigenstates of (4.28) and live on the dual lattice. This is exactly the picture envisaged in [25] about the interactions nucleating a new topological phase on top of the original one. It is an interesting project to make this connection rigorous.

4.4 Summary

In this chapter the full-vortex sector of the honeycomb lattice model has been studied. We showed that the B -phase no longer supports non-Abelian Ising anyons, but is instead described by chiral Abelian anyons. We showed that this agrees with the prediction by anyon-anyon interaction driven phase transitions [14, 25], and illustrated explicitly how the interactions microscopically give rise to the new phase.

To understand the different phases beyond the Chern number, we considered their Fermi surfaces. These describe the characteristic long-range properties, which are manifest as a differing number of Fermi points in each phase. In agreement with [82], we showed that the discovered $\nu = -2$ phase is characterized by four Fermi points. As an alternative way to characterize the phases, we identified the symmetries that are responsible for the Fermi surface topologies. In particular, we discovered that the full-vortex sector gives rise to a new lattice symmetry, that is responsible for the further doubling of Fermi points. We observed that phase transitions may occur either through breaking of the Fermi surface symmetries or due to other mechanisms such as localization. It is an interesting topic of future research to obtain a more holistic picture of the different phase transition mechanisms manifest in the honeycomb lattice model.

Having established the connection between Hamiltonian symmetries, the Fermi surface topology and the different topological phases, we studied how the Fermi surfaces evolve under phase transition driving perturbations. By monitoring the transport of Fermi point we identified the locations in the momentum space where the phase transitions occur and used them to derive analytically the critical behavior of the extended phase space. This is a novel technique, which could be employed in a variety of fermion problems. We performed the analysis numerically, but it would be desirable to be able to infer the critical momenta, i.e the locations in the momentum space where the gap closes, directly from the Hamiltonian.

As an analytic study of the Fermi surface evolution, we considered the low-energy field theory of Dirac fermions. It was shown that perturbations translate to chiral

gauge fields, that always lead to a transport of the Fermi points. We found that the form of the gauge fields is directly related to the driving perturbations obeying or breaking the Fermi surface symmetries. Although this offers an attractive alternative picture, it does not reveal at the current level new physics beyond the Fermi surface symmetries. Finding analytically a full gauge theory description similar to graphene, [104], would provide new insight. Still, we note that although Fermi point transport had been studied before in the context of fermion systems subjected to disorder [107], strain [108] or non-Abelian gauge fields [109], our results show analytically the role of gauge fields for the first time.

Chapter 5

Conclusions

In this thesis we have demonstrated that in exactly solvable systems one can go beyond the Chern number when studying the anyonic excitations. The key advance was the generalization of the solution of the model to arbitrary vortex sectors, which enabled to study the physics of only few vortices at a time. These studies revealed that the vortices introduce zero modes to the spectrum, which can acquire finite energy due to short-range interactions. By considering the spectral evolution as a function of the vortex separation, the interactions enabled us to unambiguously identify the zero modes with the fusion degrees of freedom of the Ising anyons. Our results using the exact solution agreed with the predictions of p -wave superconductors where the analysis employs effective field theory [81, 83, 89–93]. Furthermore, we fully characterized the low-energy spectrum by obtaining the coupling dependent energy gaps and the length scales of the system.

The understanding of the low-energy spectrum enabled us to consider the non-Abelian statistics, that together with the fusion rules provide full characterization of the anyon model. The calculation was carried out by evaluating the holonomy associated with a transport process where a vortex winds around another. We showed that such a calculation is possible for any system where the ground state admits representation in terms of Slater determinants, i.e. the Hamiltonian is diagonal in the basis of free fermions. By considering a range of finite systems and parameters,

we observed the holonomy converging systematically to non-Abelian statistics as the system size and the vortex separation were increased. We also obtained strong support that the statistics corresponds indeed to Ising anyons, but better numerics using larger systems are still needed for conclusive confirmation. As opposed to previous calculations employing trial wave functions [34, 94, 100], our calculation was the first to employ exact eigenstates of a microscopic model.

The discovery of interactions demonstrates clearly that the Chern number does not give a full description of the low-energy physics. Only a direct study of the anyonic excitations can reveal the length scale where the pure anyon theory provides a good approximation. This sets limits on the future experiments,[51], that are going to be performed on finite size systems. As demonstrated by our holonomy calculation, one has to be careful when preparing the system in order for it to support the predicted topological behavior. When these systems become accessible in the laboratory, our holonomy calculation provides both an experimental protocol for vortex transport as well as exact predictions for braiding experiments. Likewise, the energy gaps and the lifting of zero mode degeneracy provide measures of stability and ways to detect the fusion channels of the vortices, respectively.

The importance of understanding and controlling the interactions is emphasized by our demonstration that they not only interfere with the topological behavior, but that they can even lead to phase transitions. To understand how these transitions occur, we studied numerically the spectral evolution as the vortex density is increased and observed directly the formation of new band structure with a modified Fermi surface topology. The Fermi surface symmetry responsible for the topology could be interpreted as an emergent lattice symmetry, that appears due to the interacting anyons. This interplay of a parent model and an interaction driven emergent model has only been proposed very recently parallel to our work [25]. Our results provide the first confirmation of this novel extension to the theory of topologically ordered systems. In Section 4.3 we took first steps in understanding how the interactions give microscopically rise to a new lattice model. It is fascinating topic of future

research to make this connection rigorous.

Future work

In general, the theory of interacting anyon liquids predicts different phase transitions depending on the favoured fusion channels [14, 25]. A natural extension of our work is to consider these in the context of the honeycomb lattice model. This is possible because of the oscillations in the interactions. They imply that for certain sparse vortex sectors the fermion channel can be favoured. It would be interesting to study what happens in vortex sectors where this occurs or where a complex arrangements of the vortices makes the fusion channels compete. Kitaev's catalogue, [62], based on Chern numbers allows for up to eight different anyon models and we believe that at least some of them can be actually realized within the honeycomb lattice model. It would also be interesting to see where does the honeycomb lattice model with its various topological phases fit in the classification of topological insulators and superconductors [11, 110].

Fermi surface symmetries that arise due to emergent lattice symmetries is a new concept in the characterization of the phases. For the chiral Abelian phase, the symmetry Λ could be interpreted as acting on the dual lattice. This is actually a special case, because for sparse vortex sectors the lattice of vortices does not in general coincide with the dual lattice of the honeycomb lattice. We predict that the same mechanism should hold though. If other new phases are discovered, we postulate that their Fermi surfaces are also characterized by emergent symmetries that are lattice symmetries of the vortex lattice.

One can also turn this postulate around and envisage finding vortex lattices with different symmetries. If one then starts from the vortex-free sector and creates a particular vortex-lattice on top of it, the new symmetries of this lattice will immediately imply a new phase due to increased number of Fermi points. Although it is well known that lattice symmetries lead to doubling of Fermi points [82], to our understanding the idea of using this mechanism to drive the system into other

topological phases has not been considered before. As each Fermi point contributes $\nu = \pm 1$ to the Chern number, any emergent Z_2 lattice symmetry, such as Λ , will double the Fermi points and drive the system to some chiral Abelian phase. One could also entertain a more ambitious scenario. If the interacting vortices can give rise to a lattice with a Z_3 symmetry by having a three-site unit cell, this would lead to tripling of Fermi points giving rise to a transition between two non-Abelian phases. It is hard to see immediately how this could occur though.

Even though the physical interpretation of the Fermi surface symmetries is not yet fully understood, we regard them as useful tools to study transitions between topologically ordered phases. As they are directly related to the Chern number through the Fermi surface topology, a perturbation breaking one of these symmetries will necessarily drive a phase transition. The critical perturbations can be obtained by performing a study of the Fermi surface evolution, like the one we performed in Section 4.2. However, they do not provide full characterization of the phase transitions as illustrated by the transition to the Abelian toric code phase. It broke no symmetries, but it still led to the removal of all Fermi points. Therefore, we predict the Fermi surface symmetries to be useful for understanding transitions between chiral phases, i.e. ones with non-zero Chern number. In general, it is a fascinating topic of future work to fully map the phase space of the honeycomb lattice model across all vortex sectors and understand the role of the different physical mechanisms that give rise to it.

Finally, one would also like to understand the new chiral Abelian anyons better. Although they have no fusion degrees of freedom and thus no zero modes, outlining the low-energy spectrum would be the obvious first step. It could be employed to understand microscopically how the anyonic character of the vortices changes at the phase transitions. As a pairing of the non-Abelian Ising anyons is known to give rise to the anyons of the chiral Abelian phase [26], one could investigate whether the vortices in the $\nu = -2$ phase could somehow be understood as bound states of two $\nu = -1$ vortices. Also, a braiding calculation similar to Section 3.3 could be readily

carried out to verify the characteristic statistics of the vortices.

In summary, the contribution of the honeycomb lattice model to the contemporary study of topologically ordered phases is far from being exhausted. In this thesis we have investigated in detail its non-Abelian phase and obtained novel results on the microscopic behavior. Our results pave the way to future experiments as well as open new research directions. Once the honeycomb lattice model will hit the laboratories, its significance as a testbed for topological order can only increase.

Bibliography

- [1] Alain Connes, *Noncommutative Geometry*, Academic Press (1994).
- [2] M. de Wild Propitius and F.A. Bais, *Discrete Gauge Theories*, Lectures presented at the CRM-CAP Summer School ‘Particles and Fields 94’, Banff, Alberta, Canada, August 16-24, 1994. PAR-LPTHE 95-46 and ITFA-95-46 (1995), arXiv: hep-th/9511201.
- [3] J.M. Leinaas and J. Myrheim, On the theory of identical particles, *Il Nuovo Cimento B* **37**, 132 (1977).
- [4] F. Wilczek, Magnetic flux, angular momentum and statistics, *Phys. Rev. Lett.* **48**, 1144 (1982).
- [5] F. Wilczek, Remarks on dyons, *Phys. Rev. Lett.* **48**, 1146 (1982).
- [6] A.Y. Kitaev, Fault-tolerant quantum computation by anyons, *Ann. Phys.* **303**, 3 (2003).
- [7] M.H. Freedman, A.Y. Kitaev, M.J. Larsen, and Z. Wang, Topological quantum computation, *Bull. Amer. Math. Soc.* **40**, 31 (2004).
- [8] Ville Lahtinen, *Topological Quantum Computation - An Analysis of an Anyon Model Based on Quantum Double Symmetries*, Master’s thesis, Department of Physical Sciences, University of Helsinki (2006).
- [9] M.H. Freedman, Topological quantum computation, a talk given at KITP seminar as part of the program Exotic Order and Criticality in Quantum Matter, 2004, <http://online.kitp.ucsb.edu/online/exotic04/>.

Bibliography

- [10] E. Rowell, R. Stong and Z. Wang, On classification of modular tensor categories, *Comm. Math. Phys.* **292**, 343 (2009).
- [11] A.Y. Kitaev, Periodic table for topological insulators and superconductors, *AIP Conf. Proc.* **1134**, 22 (2009).
- [12] S. Ryu, A. Schnyder, A. Furusaki and A.W.W. Ludwig, Topological insulators and superconductors: ten-fold way and dimensional hierarchy, *arXiv:0912.2157* (2009).
- [13] J.R. Wootton, V. Lahtinen, Z. Wang and J.K. Pachos, Non-Abelian statistics from an Abelian model, *Phys. Rev. B* **78**, 161102(R) (2008).
- [14] C. Gils, S. Trebst, A. Kitaev, A.W.W. Ludwig, M. Troyer, Z. Wang, Topology driven quantum phase transitions in time-reversal invariant anyonic quantum liquids, *Nat. Phys.* **5**, 834 (2009).
- [15] O. Buerschaper and M. Aguado, Mapping Kitaev's quantum double lattice models to Levin and Wen's string-net models, *Phys. Rev. B* **80**, 155136 (2009).
- [16] P. Fendley, Topological order from quantum loops and nets, *Ann. Phys.* **323**, 3113 (2008).
- [17] A. Kitaev and J. Preskill, Topological entanglement entropy, *Phys. Rev. Lett.* **96**, 110404 (2006).
- [18] M. Levin and X.-G. Wen, Detecting topological order in a ground state wave function, *Phys. Rev. Lett.* **96**, 110405 (2006).
- [19] S. Iblisdir, D. Perez-Garcia, M. Aguado and J.K. Pachos, Thermal states of anyonic systems, *Nucl. Phys. B* **829**, 401 (2010).
- [20] H. Yao and X.-L. Qi, Entanglement entropy and entanglement spectrum of the Kitaev model, *arXiv:1001.1165* (2010).
- [21] P. Bonderson, Splitting the Topological Degeneracy of non-Abelian Anyons, *Phys. Rev. Lett.* **103**, 110403 (2009).

-
- [22] A. Feiguin, S. Trebst, A.W.W. Ludwig, M. Troyer, A. Kitaev, Z. Wang, M.H. Freedman, Interacting anyons in topological quantum liquids: The golden chain, *Phys. Rev. Lett.* **98**, 160409 (2007).
- [23] S. Trebst, E. Ardonne, A. Feiguin, D.A. Huse, A.W.W. Ludwig, M. Troyer, Collective states of interacting Fibonacci anyons, *Phys. Rev. Lett.* **101**, 050401 (2008).
- [24] C. Gils, E. Ardonne, S. Trebst, A.W.W. Ludwig, M. Troyer, Z. Wang, Collective States of Interacting Anyons, Edge States, and the Nucleation of Topological Liquids, *Phys. Rev. Lett.* **103**, 070401 (2009).
- [25] A.W.W. Ludwig, D. Poilblanc, S. Trebst and M. Troyer, Two-dimensional quantum liquids from interacting non-Abelian anyons, arXiv:1003.3453 (2010).
- [26] F.A. Bais and J.K. Slingerland, Condensate induced transitions between topologically ordered phases, *Phys. Rev. B* **79**, 045316 (2009).
- [27] F.A. Bais, J.K. Slingerland and S.M. Haaker, A theory of topological edges and domain walls, *Phys. Rev. Lett.* **102**, 220403 (2009).
- [28] J. Preskill, Lecture notes for a course of quantum computation, <http://www.theory.caltech.edu/~preskill/ph219/>.
- [29] G.K. Brennen and J.K. Pachos, Why should anyone care about computing with anyons?, *Proc. R. Soc. A* **10**, 1098 (2007).
- [30] C. Nayak, S.H. Simon, A. Stern, M.H. Freedman and S. Das Sarma, Non-Abelian Anyons and Topological Quantum Computation, *Rev. Mod. Phys.* **80**, 3 (2008).
- [31] P. Bonderson and J.K. Slingerland, Fractional Quantum Hall Hierarchy and the Second Landau Level, *Phys. Rev. B* **78**, 125323 (2008).
- [32] A. Wojs, G. Moller, S.H. Simon and N.R. Cooper, Skyrmions in the Moore-Read state at $\nu=5/2$, arXiv:0910.4176 (2009).

Bibliography

- [33] G. Moller and S.H. Simon, Paired composite fermion wavefunctions, *Phys. Rev. B* **77**, 075319 (2008).
- [34] M. Baraban, G. Zikos, N. Bonesteel and S.H. Simon, Numerical Analysis of Quasiholes of the Moore-Read Wavefunction, *Phys. Rev. Lett.* **103**, 076801 (2009).
- [35] R.B. Laughlin, Anomalous quantum Hall effect - an incompressible quantum fluid with fractionally charged excitations, *Phys. Rev. Lett.* **50**, 1395 (1983).
- [36] R. de-Picciotto, M. Reznikov, M. Heiblum, V. Umansky, G. Bunin and D. Mahalu, Direct observation of a fractional charge, *Nature* **389**, 162 (1997).
- [37] F.E. Camino, W. Zhou and V.J. Goldman, Realization of a Laughlin quasiparticle interferometer: observation of fractional statistics, *Phys. Rev. B* **72**, 075342 (2005).
- [38] G. Moore and N. Read, Nonabelions in the fractional quantum Hall effect, *Nucl. Phys. B* **360**, 362 (1991).
- [39] P. Bonderson, K. Shtengell and J.K. Slingerland, Probing non-Abelian statistics with quasiparticle interferometry, *Phys. Rev. Lett.* **97**, 016401 (2006).
- [40] P. Bonderson, K. Shtengell and J.K. Slingerland, Interferometry of non-Abelian anyons, *Ann. Phys.* **323**, 2709 (2008).
- [41] R.L. Willett, L.N. Pfeiffer and K.W. West, Measurement of filling factor $5/2$ quasiparticle interference with observation of charge $e/4$ and $e/2$ period oscillations, *PNAS* **106**, 8853 (2009).
- [42] W. Bishara, P. Bonderson, C. Nayak, K. Shtengel and J.K. Slingerland, The non-Abelian interferometer, *Phys. Rev. B* **80**, 155303 (2009).
- [43] C.L. Kane and E.J. Mele, Quantum Spin Hall Effect in Graphene, *Phys. Rev. Lett.* **95**, 226801 (2005).

-
- [44] L. Fu and C.L. Kane, Superconducting Proximity Effect and Majorana Fermions at the Surface of a Topological Insulator, *Phys. Rev. Lett.* **100**, 096407 (2008).
- [45] L. Fu, C.L. Kane and E.J. Mele, Topological insulators in three dimensions, *Phys. Rev. Lett.* **98**, 106803 (2007).
- [46] M. König, S. Wiedmann, C. Bruene, A. Roth, H. Buhmann, L.W. Molenkamp, X.-L. Qi and S.-C. Zhang, Quantum Spin Hall Insulator State in HgTe Quantum Wells, *Science* **318**, 766 (2007).
- [47] D. Hsieh, D. Qian, L. Wray, Y. Xia, Y.S. Hor, R.J. Cava and M.Z. Hasan, A topological Dirac insulator in a quantum spin Hall phase, *Nature* **452**, 970 (2008).
- [48] F. Wilczek, Majorana returns, *Nat. Phys.* **5**, 614 (2009).
- [49] S. Bravyi, Universal quantum computation with the $\nu = 5/2$ fractional quantum Hall state, *Phys. Rev. A* **73**, 042313, (2006).
- [50] S. Tewari, S. Das Sarma, C. Nayak, C. Zhang and P. Zoller, Quantum computation using vortices and Majorana zero modes of a $p_x + ip_y$ superfluid of fermionic cold atoms, *Phys. Rev. Lett.* **98**, 010506, (2007).
- [51] A. Micheli, G. K. Brennen, and P. Zoller, A toolbox for lattice spin models with polar molecules, *Nat. Phys* **2**, 341 (2005).
- [52] G.K. Brennen, A. Micheli and P. Zoller, Designing spin-1 lattice models using polar molecules, *New J. Phys.* **9**, 138 (2007).
- [53] L.M. Duan, E. Demler, and M.D. Lukin, Controlling spin exchange interactions of ultracold atoms in optical lattices, *Phys. Rev. Lett.* **91**, 090402 (2003).
- [54] H.P. Büchler, E. Demler, M. Lukin, A. Micheli, N. Prokof'ev, G. Pupillo and P. Zoller, Strongly correlated 2D quantum phases with cold polar molecules:

Bibliography

- controlling the shape of the interaction potential, *Phys. Rev. Lett.* **98**, 060404 (2007)
- [55] B. Doucot, L.B. Ioffe, and J. Vidal, Discrete non-abelian gauge theories in Josephson-junction arrays and quantum computation, *Phys. Rev. B* **69**, 214501 (2004).
- [56] B. Paredes and I. Bloch, Minimum instances of topological matter in an optical plaquette, *Phys. Rev. A* **77**, 023603 (2008).
- [57] G. K. Brennen, M. Aguado and J.I. Cirac, Simulations of quantum double models, *New J. Phys.* **11**, 053009 (2009).
- [58] M. Aguado, G.K. Brennen, F. Verstraete and J.I. Cirac, Creation, manipulation, and detection of Abelian and non-Abelian anyons in optical lattices, *Phys. Rev. Lett.* **101**, 260501 (2008).
- [59] J.R. Wootton, V. Lahtinen and J.K. Pachos, Universal quantum computation with a non-Abelian topological memory, *LNCS 5906*, 56 (2009).
- [60] S. Gladchenko, D. Olaya, E. Dupont-Ferrier, B. Doucot, L.B. Ioffe and M.E. Gershenson, Superconducting nano-circuits for topologically protected qubits, *Nat. Phys.* **5**, 48 (2008).
- [61] J.R. Wootton, V. Lahtinen, B. Doucot and J.K. Pachos, Engineering non-Abelian topological memories from Abelian lattice models, *arXiv:0908.0708* (2009).
- [62] A.Y. Kitaev, Anyons in an exactly solved model and beyond, *Ann. Phys.* **321**, 2 (2006).
- [63] M. Levin and X.-G. Wen, String-net condensation: A physical mechanism for topological phases, *Phys. Rev. B* **71**, 045110 (2005).
- [64] G. Kells, A.T. Bolukbasi, V. Lahtinen, J.K. Slingerland, J.K. Pachos and J.

- Vala, Topological degeneracy and vortex manipulation in Kitaev's honeycomb model, *Phys. Rev. Lett.* **101**, 24 (2008).
- [65] J. Vidal, K.P. Schmidt and S. Dusuel, Perturbative approach to an exactly solved problem: the Kitaev honeycomb model, *Phys. Rev. B* **78**, 245121 (2008).
- [66] K. P. Schmidt, S. Dusuel, J. Vidal Emergent Fermions and Anyons in the Kitaev Model, *Phys. Rev. Lett.* **100**, 057208 (2008)
- [67] D.-H. Lee, G.-M. Zhang and T. Xiang, Edge solitons of topological insulators and fractionalized quasiparticles in two dimensions, *Phys. Rev. Lett.* **99**, 196805 (2007).
- [68] G. Kells, J.K. Slingerland and J. Vala, A description of Kitaev's honeycomb model with toric-code stabilizers, *Phys. Rev. B* **80**, 125415 (2009).
- [69] H. Yao and S.A. Kivelson, An exact chiral spin liquid with non-Abelian anyons, *Phys. Rev. Lett.* **99**, 247203 (2007).
- [70] H. Yao, S.-C. Zhang, S.A. Kivelson, Algebraic spin liquid in an exactly solvable spin model *Phys. Rev Lett.* **102**, 217202 (2009).
- [71] V. Lahtinen, G. Kells, T. Stitt, J. Vala and J.K. Pachos, The spectrum of the non-Abelian phase of the honeycomb lattice model, *Ann. Phys.* **323**, 9 (2008).
- [72] V. Lahtinen and J.K. Pachos, Non-Abelian statistics as a Berry phase in exactly solvable models, *New J. Phys.* **11** 093027 (2009).
- [73] V. Lahtinen and J.K. Pachos, Topological phase transitions driven by gauge fields in an exactly solvable model, *arXiv:1003.1086* (2010).
- [74] M. Oshikawa, Y.B. Kim, K. Shtengel, C. Nayak and S. Tewari, Topological degeneracy of non-Abelian states for dummies, *Ann. Phys.* **322**, 1477 (2007).
- [75] J.E. Avron, R. Seiler and B. Simon, Homotopy and quantization in condensed matter physics, *Phys. Rev. Lett.* **51**, 51 (1983).

Bibliography

- [76] D.J. Thouless, M. Kohmoto, M.P. Nightingale and M. den Nijs, Quantized Hall conductance in a two-dimensional periodic potential, *Phys. Rev. Lett.* **49**, 405 (1982).
- [77] Y. Hatsugai, Chern number and edge states in the integer quantum Hall effect, *Phys. Rev. Lett.* **71**, 3697 (1993).
- [78] J.S. Xia, W. Pan, C.L. Vicente, E.D. Adams, N.S. Sullivan, H.L. Stormer, D.C. Tsui, L.N. Pfeiffer, K.W. Baldwin, K.W. West, Electron Correlation in the Second Landau Level: A Competition Between Many Nearly Degenerate Quantum Phases, *Phys. Rev. Lett.* **93**, 176809 (2004).
- [79] G. Volovik, *The Universe in a Helium Droplet*, Clarendon Press, Oxford (2003).
- [80] C.Y. Hou, C. Chamon and C. Mudry, Electron fractionalization in two-dimensional graphenelike structures, *Phys. Rev. Lett.* **98**, 186809 (2007).
- [81] D.A. Ivanov, Non-Abelian statistics of half-quantum vortices in p -wave superconductors, *Phys. Rev. Lett.* **86**, 268 (2001).
- [82] F.D.M. Haldane, Model for a Quantum Hall Effect without Landau Levels: Condensed-Matter Realization of the Parity Anomaly, *Phys. Rev. Lett.* **61**, 2015 (1988).
- [83] N. Read and D. Green, Paired states of fermions in two dimensions with breaking of parity and time-reversal symmetries, and the fractional quantum Hall effect, *Phys. Rev. B* **61** 10267 (2000).
- [84] M. Nakahara, *Geometry, Topology and Physics*, Adam Hilger, Bristol (1990).
- [85] T. Fukui, Y. Hatsugai and H. Suzuki, Chern Numbers in Discretized Brillouin Zone: Efficient Method of Computing (Spin) Hall Conductances, *J. Phys. Soc. Jpn.* **74** 1674-1677 (2005).
- [86] J. K. Pachos, The wavefunction of an anyon, *Ann. Phys.* **322**, 1254 (2007).

- [87] J.C. Slater, The theory of complex spectra, Phys. Rev. **34**, 10 (1929).
- [88] E.H. Lieb, The flux-phase of the half-filled band, Phys. Rev. Lett. **73**, 2158 (1994).
- [89] H.-D. Chen and Z. Nussinov, Exact results on the Kitaev model on a honeycomb lattice: spin states, string and brane correlators and anyonic excitations, J. Phys. A **41**, 075001 (2008).
- [90] V. Gurarie and L. Radzihovsky, Zero modes of two-dimensional chiral p -wave superconductors, Phys. Rev. B **75**, 212509 (2007).
- [91] A. Stern, F. von Oppen and E. Mariani, Geometric phases and quantum entanglement as building blocks for non-Abelian quasiparticle statistics, Phys. Rev. B **70**, 205338 (2004).
- [92] M. Stone and S.-B. Chung, Fusion rules and vortices in $p_x + ip_y$ superconductors, Phys. Rev. B **73**, 014505 (2003).
- [93] M. Cheng, R.M. Lutchyn, V. Galitski and S. Das Sarma, Splitting of Majorana modes due to intervortex tunneling in a $p+ip$ superconductor, Phys. Rev. Lett. **103**, 107001 (2009).
- [94] D. Arovas, J.R. Schrieffer and F. Wilczek, Fractional statistics and quantum Hall effect, Phys. Rev. Lett **53**, 722 (1984).
- [95] M.V. Berry, Quantal phase factors accompanying adiabatic changes, Proc. R. Soc. Lond. A **392**, 45 (1984).
- [96] B. Simon, Holonomy, the quantum adiabatic theorem and Berry's phase, Phys. Rev. Lett. **51**, 24 (1983).
- [97] F. Wilczek and A. Zee, Appearance of gauge structure in simple dynamical systems, Phys. Rev. Lett. **52**, 2111 (1984)
- [98] N. Read, Non-Abelian adiabatic statistics and Hall viscosity in quantum Hall states and $p_x + ip_y$ paired superfluids, Phys. Rev. B **79**, 045308 (2009).

Bibliography

- [99] A. Messiah, *Quantum Mechanics*, Amsterdam, (1962).
- [100] Y. Tserkovnyak and S.H. Simon, Monte Carlo evaluation of non-Abelian statistics, *Phys. Rev. Lett.* **90**, 016802 (2003).
- [101] M.E. Peskin and D.V. Schroeder, *An Introduction to Quantum Field Theory*, Westview Press Inc (1995).
- [102] W.-Y. Hsiang and D.H. Lee, Chern-Simons invariant in the Berry phase of a 2×2 Hamiltonian *Phys. Rev A* **64**, 052101 (2001).
- [103] X.-G. Wen and A. Zee, Winding number, family index theorem, and electron hopping in a magnetic field, *Nucl. Phys. B* **316**, 641 (1989).
- [104] R. Jackiw and S.-Y. Pi, Chiral gauge theory for graphene, *Phys. Rev. Lett.* **98**, 266402 (2007).
- [105] N. Read and A.W.W. Ludwig, Absence of a metallic phase in random-bond Ising models in two dimensions: Applications to disordered superconductors and paired quantum Hall states, *Phys. Rev. B* **63**, 024404 (2000).
- [106] E. Grosfeld and A. Stern, Electronic transport in an array of quasiparticles in the $\nu=5/2$ non-Abelian quantum Hall state, *Phys. Rev. B* **73**, 201303 (2006).
- [107] M.S. Foster and A.W.W. Ludwig, Interaction effects on 2D fermions with random hopping, *Phys. Rev. B* **73**, 155104 (2006).
- [108] V.M. Pereira, A.H. Castro Neto and N.M.R. Peres, A tight-binding approach to uniaxial strain in graphene, *Phys. Rev B* **80**, 045401 (2009).
- [109] A. Bermudez, N. Goldman, A. Kubasiak, M. Lewenstein and M.A. Martin-Delgado, Topological phase transitions in the non-Abelian honeycomb lattice, *New J. Phys.* **12**, 033041 (2010).
- [110] A. Ruegg, J. Wen and G.A. Fiete, Topological insulators on the decorated honeycomb lattice, *arXiv:0911.4722* (2009).